University of Alberta

Exploration of the Effects of Pressure and Temperature on the Evaporation Rate of Selected Liquids

by

Aydin Jafarnejad

A thesis submitted to the Faculty of Graduate Studies and Research
in partial fulfillment of the requirements for the degree of

Master of Science

Department of Mechanical Engineering

Fall 2009
Edmonton, Alberta

In the memory of my dear Grandmother and Uncle

Examining Committee

Dr. Larry Kostiuk, Department of Mechanical Engineering.

Dr. Janet A. W. Elliott, Department of Chemical and Materials Engineering.

Dr. Morris Flynn, Department of Mechanical Engineering.

Abstract

The rate of evaporation of liquids has been a topic of research for over a century. A detailed understanding of this phenomena is required to make scientific advancements in various areas. The principal objective for conducting this work was to study the effect of pressure on the rate of evaporation of liquids in close to equilibrium conditions, and further increase the much needed lack of existing data sets for evaporation of liquids in any such controlled environment.

The experimental setup involved two glass cannisters, each containing four glass capillaries. The capillaries were filled with liquid at various levels, and tests were preformed at fixed temperatures while the containers maintained vacuum. This initial condition was not at equilibrium and liquid from the capillaries slowly evaporated. By measuring the change in liquid height in the capillaries the net rate of evaporation was estimated.

The experimental results suggested that even though, as thought before, pressure has a role in determining the rate of evaporation of liquids, for the case where the evaporation takes place from a receding meniscus inside a capillary tube, the rate of vapor diffusion out and away from an evaporating meniscus could be equally as important, and the pressure build up above an evaporating meniscus entrapped inside a capillary tube could impede the evaporation rate.

Acknowledgements

I humbly acknowledge with thanks and gratitude my thesis Supervisor, Professor Larry Kostiuk. He provided supervision, encouragement, and direction so that the research for this thesis could be completed. I wish to thank Professor Janet Elliott for her support during difficult times, great conversations, and the thermodynamics I have learned from her.

I would like to thank my friends at the Department of Mechanical Engineering who have both intellectually and socially supported me and with whom I have many great memories: Ahmad Ghazi, Siavash Rezazadeh, Mehdi Saffarian, and Neda Nazemifard.

Special thanks to technicians in the Department of Mechanical Engineering machine shop especially Bernie Faulkner,Roger Marchand, and Andrew Campbell.

I thank the remaining members of my committee for their time, valuable suggestions and challenging questions: Dr. Morris Flynn, and Dr. Jason Olfert. Dr. Payam Rahimi was present and supervised this work from September of 2005 until December of 2008. I wish to thank him for all his help and introducing me to this interesting field of studies.

Finally I wish to thank my dear parents, Auntie Nessie, Arya, Wayne, Maryam, and Omid whose unconditional support and encouragement helped me through all the tough times.

Financial support from the Faculty of Graduate Studies, Department of Mechanical Engineering and the Graduate students' Association is also gratefully acknowledged.

Edmonton, Alberta

July 20, 2009

Aydin Jafarnejad

Table of Contents

List of Tables

List of Figures

List of Symbols

A	area
A^{LV}	area of the liquid-vapor interface
H	in geometry, the height of a cylindrical container
M	molecular weight
P	hydrostatic pressure (Pa)
S	entropy
S^*	modified entropy of the system
S_m	entropy of the fluid in the capillary
T	absolute temperature (K)
U	internal energy
V	volume
f_m	Maxwellian velocity distribution
h	height of the meniscus from the reference point
$\hbar$	Plank's constant
k	Boltzmann constant
s	intensive entropy (per unit volume or area)
u	intensive internal energy (per unit volume or area)
z	elevation along the axis of a cylindrical container

Greek Symbols

ΔT	applied temperature difference in two surface system
Λ	thermal de Broglie wavelength
α	modified intensive entropy per unit volume as a function of energy and number of moles
β	modified intensive entropy per unit area as a function of energy and number of moles
γ	surface tension
ϕ	potential energy due to gravitational field
κ	isothermal compressibility
λ	Lagrangian multiplier
μ	chemical potential
ν	molar volume
θ	turning angle measured from the axis of a symmetric interface
θ_c	contact angle

Subscripts and Superscripts

L	liquid
S	solid
V	vapor
LV	liquid-vapor interface
SL	solid-liquid interface
SV	solid-vapor interface

Abbreviations

CST	Commonly-Shared-Trend
liq	liquid
menisc	meniscus
SRT	Statistical rate theory
vap	vapor

Chapter 1

Introduction

1.1 Motivation

The rate of evaporation, which is a case of interfacial molecular transport, has been a topic of research for over a century. Beginning from the early 19th century with Hertz (1882), Stefan (1889), Knudsen (1915) until today, it has been a continuous issue of evolving theories as well as interdisciplinary contributions. Elaborative study of the phenomena of evaporation and condensation is more intriguing than it first appears. Despite all these endeavors, still some fundamental questions and disputes remain unresolved and yet to be discovered. By reviewing earlier research work regarding these phenomena and comparing them to current advancements, one may conclude that this subject could benefit from more theoretical and experimental research, and is open to major mutual collaboration from various scientific and industrial disciplines.

Even though a basic understanding of this phenomenon is sufficient for some practical applications, more detailed models are widely needed in order to make advancements in the areas that require precise information about evaporation. For example, many industrial and technological applications such as heat pipes, cooling devices, chemical processing equipment, micro electro-mechanical sys-

tems, and surface sciences require advanced and accurate information about surface tension, adsorption, interface pressure and temperature gradients, contact angle, evaporation rate and many more topics which are related to evaporation and phase change. Many theoretical and experimental models for prediction of the rate of evaporation of liquids under various conditions have been developed over the years but for many the deviation in their models is a topic of controversial arguments in the scientific community. To this time, prediction of the rate of evaporation has been tested by exploiting three different theories: continuum mechanics, classical kinetic theory and the statistical rate theory (SRT).

In 1977 an elementary form of Statistical Rate Theory (SRT), a quantum statistical thermodynamic model, was proposed. Since then, this theory has been matured and applied to investigate various physical phenomena (e.g. adsorption of gases on solid surfaces, evaporation of liquids, etc.). The SRT has offered us insight to some phenomena for which the theoretical understanding has lagged behind empirical knowledge. For example, the "anomalous temperature profile" at the interface of an evaporating liquid film is a discontinuity of temperature which exists at the interface with the temperature of the vapor higher than that in the liquid. This phenomenon is predicted by SRT and supported by experiments whereas the classical kinetic theory fails to predict the temperature gradient direction and the continuum theory makes the assumption of temperature continuity. Following this theory, a vast amount of theoretical and experimental work has been performed that provided additional verification of this model's applicability in various areas dealing with near equilibrium conditions (Rizk (1982), Rudzinski (1991), Elliott (1997), Fang (1999), Rahimi (2003), and Duan (2005)).

In the current work, the rate of liquid evaporation (relatively close to equilib-

rium) to its own vapor as a function of vapor phase pressure was scrutinized. In accordance with SRT predictions, very small and essentially immeasurable variation in pressure (approximately on the order of $10^{-}3$ [Pa]) would be expected to increase/decrease the rate of evaporation, a hypothesis that other models fail to capture. The key motivating point is to shed new lights on understanding the rate of phase change of material between vapor and liquid in near equilibrium conditions, and this thesis is part of the exploration of those phenomena.

The most important application with high impact on Alberta's development and economy is the optimization of oil production and refinement which is one of Alberta's strategic priorities. Currently, Canada's major industries require vast resources of energy and with world energy sources heading toward depletion, highly efficient methods for providing energy is becoming crucial. Since the major resource for energy is oil, acquiring more efficient procedures to refine conventional and heavy oil in Alberta and economical techniques to extract oil from Alberta's oil-sands along with exporting the developed technologies is inevitable. Thus, realistic predictions and accurate data are needed for developing highly efficient and feasible production technologies.

1.2 Objectives

The goals and objectives of this thesis are to systematically investigate the rates of evaporation very near to the equilibrium state of pure substances (e.g., water, octane and methycyclohexane) in a single component controlled environment. In this context, the temperature was kept constant and there was no mass transfer in or out of the experimental setup during the course of the experiments. These conditions make it possible to use the thermodynamic laws to investigate the effect of pressure on the rate of evaporation and compare the results to

existing models (e.g., Statistical Rate Theory). The emphasis of the thesis is to experimentally establish such an environment and eliminate factors that are known to have an effect on the evaporation of liquids (e.g., temperature variation, ambient vapor pressure and etc.) so that one would obtain a better understanding of the effect of pressure on this phenomena.

1.3 Methodology

The experimental setup is based on the test performed originally by Rahimi et. al [4]. The basic geometry consists of a cylindrical glass tube with capillaries (1.1mm in diameter) mounted on a saucer filled with a pure liquid. After the lid of the tube was closed the liquid was degassed in order to create a single component system. The liquid inside the capillaries evaporates into the glass tube filled with the vapor of testing liquid that is held at a constant temperature. Two custom built glass containers with different gap between the glass tube and the saucer were made. The gap determines the shape of the liquid meniscus formed in-between and hence the liquid pressure at its apex. The effect of the pressure on the rate of evaporation for various liquids at different temperatures between the two containers could then be studied studied as the system tried to reach equilibrium. The positive attributes relative to the original experiment are the addition of another geometry, conducting the tests in various temperatures and using liquids other than water, with the key feature being the establishing evaporative interfaces with very small variations in pressure between them.

1.4 Thesis Structure

Chapters 2 gives an overview about the phenomenon of evaporation, its importance and applications in industry and pure scientific advancements made

in this field of studies, as well as some of the proposed models used in estimation of the evaporation flux and other literature relevant to comprehending the underlying physics of this phenomena. In Chapter 3, classical thermodynamic relations will be used to determine the equilibrium conditions for the system of study. It will be shown that by having certain geometrical dimensions of the interface, the radius of curvature could be estimated which ultimately would be used to numerically calculate the bulk liquid pressure in the system. In Chapter 4, the SRT and its applications in predicting nonequilibrium processes is introduced and with the use of statistical thermodynamics an expression for the net evaporation flux will be expressed. Chapter 5, discusses the experimental setup, apparatus and techniques used for collecting data. The experimental data and post processing of the results is provided in Chapter 6. Finally, Chapter 7, gives a summery of the presented work and some ideas for future work.

Chapter 2

Review of relevant literature

A full review of evaporation and condensation is a daunting task and can be found elsewhere [5]. The perspective taken in this chapter is to introduce some of the common approaches by giving an overview of the classical work of Hertz and its extension by Knudsen, which is followed by a review of literature for the case of an evaporating meniscus inside a capillary tube.

2.1 Hertz-Knudsen

Hertz conducted a series of experiments on evaporation of mercury in a very low vapor pressure (i.e. vacuum) conditions and introduced an empirical relation for the upper limit to the maximum rate of evaporation [6]

$$j_m = \frac{1}{4}\, n\, \bar{c} \tag{2.1}$$

where j_m is the maximum rate of molecular transition (i.e. evaporation), n represents the density number of gas molecules, and $\bar{c}$ is the mean velocity of gaseous molecules. In descriptive terms, the equation above indicates the number of gas molecules, n, impinging per unit area per unit time. Using the

Maxwell's law of velocity distribution of molecules for an ideal gas, the mean velocity in the space may be expressed as [7]

$$\overline{c} = \left(\frac{8kT_{sat}}{\pi m}\right)^{1/2} \tag{2.2}$$

where k is the Boltzmann constant, T_{sat} the saturated temperature and m is the mass of the molecule.

By substituting equation 2.2 and the ideal gas law (i.e. $n = P_{sat}/k\,T_{sat}$) in equation 2.1 the maximum rate of molecular transition, known as the Hertz equation could be obtained [8]

$$j_m = \frac{P_{sat}}{(2\pi m k T_{sat})^{1/2}} \tag{2.3}$$

Knudsen [9] performed experiments on the rate of evaporation for pure mercury and enhanced Hertz's equation by introducing an evaporation coefficient. In order to correlate his experimental data with theory, Knudsen defined σ_e (i.e. the evaporation coefficient), as the rate of molecules transferred to the vapor phase to the rate of the molecules emitted from the liquid surface.

The well known Hertz-Knudsen formula expresses the mass flux as the difference of the absolute rates of evaporation and condensation, and has been widely used for the case of an evaporating liquid into its own vapor [10]

$$j = \frac{1}{(2\pi m k)^{1/2}} \left(\sigma_e \frac{P_{sat}}{T_{sat}^{1/2}} - \sigma_c \frac{P_v}{T_v^{1/2}}\right) \tag{2.4}$$

where P_v and T_v are the pressure and temperature evaluated in the vapor phase. In the equation 2.4, σ_e and σ_c are the evaporation and condensation coefficients

respectively. However, the aforementioned coefficients were considered to be equal until Prüger, introduced the condensation coefficient, σ_c, analogous to the evaporation coefficient as the rate of molecules adsorbed by the liquid phase to the incident molecules [11].

From the molecular point of view, when a particle in the vapor phase collides with the liquid-vapor interphase, the incident molecule can be intercepted by the liquid, i.e, it condenses. However, if a molecule at the interface gains enough energy, it detaches from the interface, i.e, evaporates. Fig. 2.1 schematically depicts these phenomena. In thermodynamic equilibrium, the evaporation and condensation coefficients are considered to be equal [10].

The evaporation/condensation coefficients of many liquids such as water have been extensively studied; however the reported values cover a wide range. The existence of this discrepancy could partially be due to chemical impurities, and apparent differences in experimental apparatus and testing conditions [8, 11].

2.2 Schrage Correction

Schrage [12] further enhanced Hertz-Knudsen's equation by considering the following factors. First, he assumed that the center of mass of a molecule could be considered as a point with velocities v_x, v_y, and v_z in each Cartesian coordinate direction with x being the direction normal to the surface. Second, he included the prevailing fact that during evaporation there will be a mean bulk velocity, v_b, away from the liquid interface with no collision between the vapor molecules. Thus, the Maxwellian velocity distribution (f_m) could be expressed as [9]

$$f_m = A \cdot \exp\left\{ -\beta_\circ^2 \left[(v_x - v_b)^2 \, v_y^2 \, v_z^2 \right] \right\} \tag{2.5}$$

Here, A=$n\frac{\beta_\circ^3}{\pi^{3/2}}$ and $\beta_\circ = \left(\frac{m}{2kT_{sat}}\right)^{1/2}$ are constants which depend on thermodynamic states of the gaseous phase.

For small net flow away from the interface, Schrage's expression for the mass flux is given by [10, 11]

$$j = \frac{2}{2-\sigma_c} \cdot \left(\frac{1}{2\pi m k}\right)^{1/2} \left(\sigma_e \frac{P_{sat}}{T_s^{1/2}} - \sigma_c \frac{P_v}{T_v^{1/2}} \right) \tag{2.6}$$

This equation differs from equation 2.4 by the first factor on the right hand side. In the case where σ_e and σ_c are assumed to be equal to one, Schrage's equation predicts twice the flux of the Hertz-Knudsen [10]. This equivalence in temperature could only be true when there is a thermal equilibrium between two phases ($T^L = T^V$), which suggests that the rate of evaporation and condensation are equal. However, this is not always true given that the interface by definition is in a state of non-equilibrium during net evaporation or condensation. It should be noted that in principle σ_e depends on the liquid interface properties, whereas molecular dynamic simulations suggest that σ_c is a function the energy of the impinging molecule as well as the temperature at the interface. [11,13,14].

Barret et al. [10] further investigated the accuracy of the method developed by Schrage, and indicated that they failed to consider the factors which ultimately lead to violations of conservation of momentum and energy at the interface (e.g. the consideration of heat transfer through Knudsen layer for evaporation. The Knudsen layer is defined as the region near the interface where

molecular collisions are negligible thus the molecular exchange can be described by kinetic theory [13]). They then improved the relation based on a Maxwell-Boltzmann molecular distributions and rewrote the expression for the net rate of evaporation. It is known that during evaporation an interfacial resistance to mass transfer due to heat transfer and irreversibility process attenuates this phenomenon [1]. This phenomena (i.e. evaporation) is a topic of its own and further speculation is not in the scope of this work.

2.3 Temperature Inversion

Pao [15–17] presented an approximate analytic solution for the temperature jump for the half-space, as well as the two surface problem of evaporation and condensation. The two surface problem is the case with the vapor phase trapped between two liquid films at different temperatures, the modeled temperature profile showed an opposite trend than would have otherwise been expected. The boundary conditions for such a system were defined such that the emitted vapor from the one interface would ultimately condense on the other interphase and the vapor was treated as a monatomic gas obeying the Maxwellian distribution. In the view of kinetic theory, this phenomenon (i.e. temperature inversion) could occur when the latent heat of vaporization is greater than 4.5 times the thermal energy (i.e. $h_{fg} > \frac{9}{2}RT$). Considering that Toruton approximated the latent heat of gases to be equal to $10RT$, the inverted temperature profile will occur in the case of a condensing gaseous molecule on a wall [18].

The magnitude of temperature jump for this criterion would be such that the temperature profile in a vapor phase confined between two liquids kept at different temperatures, would have a slope opposite to the applied temperature

difference. This implies that the temperature across a gap from a hot to a cold wall does in fact increase locally in the vicinity of the colder interface [19]. He concluded that this phenomena should occur throughout the Knudsen layer in the vicinity of the interface. The thickness of this layer is on the order of the molecules mean free path [13].

Even though the inverted temperature gradient appears physically unrealistic [20], the evidence of validity of this phenomenon was tested by several authors [18, 19, 21]. Hermnas et al. [22], pointed out that the anomalous temperature profile does not violate the second law of thermodynamics and should not be marked physically unrealistic.

More recently Meland et al. [23], Frezzotti [24], and Wleklinski [25] performed nonequilibrium molecular dynamics simulations for a single component system where two liquid phases were kept at different temperatures with the vapor phase in between. They verified that an inverted temperature gradient does in fact exist for low Mach numbers (i.e. in the slow evaporation/condensation regime) and small liquid temperature difference between the liquid slabs. Johannessen et al. [26] also confirmed these results using the nonequilibrium van der Waals square gradient model. However, it was concluded that large evaporation and condensation fluxes would result in a large temperature difference across the surfaces and hence larger temperature gradients. This phenomenon is a subject all in itself, so discussion here was necessarily brief.

2.4 Temperature discontinuity at the interface of an evaporating meniscus

Fang et al. [27, 28] studied the variation between the liquid and vapor phase temperature for evaporation of liquids (with various temperatures) under steady state conditions. In their experiments, the liquid of interest was pumped into the bottom of a funnel (forming a concave interface) at the same rate it was evaporating. The funnel was placed inside a chamber and was subjected to a continuous vacuum during the course of experiments. Micro-thermocouples (approximately 20 μm) were used to measure the temperature profile of the evaporating meniscus in both the liquid and vapor phases. They showed that the temperature in the vapor is higher than that of the liquid phase (i.e. $T^V > T^L$).

Duan et al. [29–32] conducted a similar class of experiments studying the evaporation of various liquids (under steady state conditions) and the corresponding temperature discontinuity from a circular funnel. They hypothesized that thermocapillary convection could occur in water evaporation in the presence of a temperature gradient at the interface.

In general, the convective movements caused by surface tension gradients give rise to a type of flow movement, that is referred to as the Bénard-Marangoni motion. The instability in this convection is driven by two mechanisms. The first arises from the difference in densities across the liquid thickness (Rayleigh-Bénard), and the second is induced by the surface tension gradient generated by temperature variations at the interface due to uneven evaporation (Bénard-Marangoni) [33–36].

In the case of a circular convex interface, Duan et al. [29–32] observed an axisymmetric, parabolic temperature profile with the minimum at the centerline and the maximum at the periphery (i.e. the rim of the funnel). This finding

indicates that the evaporation rate is higher at the centerline of the meniscus.

It is worth mentioning that for most liquids, surface tension is inversely proportional to the temperature of the liquid [37]. This would then suggest the existence of a flow pattern from the warmer region to the cooler (i.e. from the periphery towards the centerline, where most of the evaporation was shown to take place).

Due to uneven evaporation across the interface (formed inside a capillary tube), the region adjacent to the wall of the capillary is colder than the apex (in the case of a concave interface). As a result the iso-concentration lines in the vapor phase above an evaporating meniscus are closer together above the center. Intuitively, the partial pressure gradient would be greater above the triple line inducing vapor circulation as a result of concentration gradient. However, the induced density gradient for vapor phase is too weak to contribute to gravitational convection and a viscous drag circulation due to Maragnoni motion could also be ruled out (due to small viscosity of the vapor phase) [36]. The authors demonstrated that a decrease in evaporation flux would result in a similar trend in the temperature discontinuity. In addition, interface curvature affects temperature discontinuity, and was found to be minimal for interfaces with smaller curvature.

This outcome was partially explain by the numerical model of Bond et al. [13], however, their model fell short of scientific reliance due to the over simplification of the geometries used, and modeling of water vapor as a monatomic ideal gas.

Popov et al. [38] performed a similar series of experiments , where they showed that an increase in evaporation rate is linked to a decrease in the vapor pressure and the resulting increase in the interfacial temperature jump.

Badam et al. [1] also investigated the interfacial temperature discontinuity

during steady state evaporation. They reconfirmed the results published by previous authors suggesting that a decrease in the vapor pressure is coupled with an increase in both the evaporation flux and temperature jump across the interface.

It is worth mentioning that using data from the literature on temperature discontinuity of a concave interface may not be quantitatively applicable to non-forced evaporation cases because the interface is not exposed to a continuous vacuum as that seen by experiments preformed to further enhance the severity of this phenomenon. Despite this uncertainty in our ability to interpret the experimental data on temperature discontinuity for an unforced evaporation from a concave interface, one fact is made very clear by the data available in the literature: a decrease in the evaporation flux will result in a decrease in the temperature discontinuity at the interface (i.e. the difference between the liquid and vapor temperature). Fig. 2.2 amply depicts this trend.

2.5 Evaporating meniscus in a capillary tube

In this section, a brief overview for the case of an evaporating meniscus inside a capillary tube is provided. Indeed, there is a vast amount of literature available speculating various aspects of evaporation from such a meniscus, but we shall limit our focus to self induced (i.e. spontaneous) evaporation cases. The evaporation inside a confined boundary such as a capillary has been the subject of study for many researchers who have speculated on the mass transport and heat transfer associated with an evaporating extended meniscus [39–42].

When a liquid meniscus wets the wall of a capillary, its characteristic evaporative and heat transfer behavior is generally classified into three sub re-

gions [41, 43]. The first region is the equilibrium thin film region (the adsorbed layer). In this region van der Walls forces are dominant, as a result, due to strong adhesion forces the evaporation is suppressed and the heat transfer is minimal [40].

Second, next to the adsorbed layer, is a very thin region where most of the evaporation is believed to take place. This conclusion is made due to the balance between the capillary forces (controlled by surface tension) and adhesion forces. This region is referred to as the micro-region, where it is believed that between 50% to 80% of the total mass transfer takes place [43, 44]. The third and final region is extended from the former (i.e. the micro-region) to the bottom (or apex) of the meniscus and is known as the macro-region. In this region, capillary forces are dominant, and the growth of film thickness increases the thermal resistance, which ultimately attenuates evaporation. In comparison with the micro-region, the overall heat and mass transfer from this portion are insignificant [43]. A schematic of the meniscus sub regions is depicted in Fig. 2.3.

Rice et al. [45] modeled the diffusion of the evaporated vapor into the air domain and found the diffusion to be stronger in the vicinity of the wall than the center of the meniscus. Their simulation, as we will see later, was in agreement with the experimental findings of various groups of authors [33, 46–49].

Wang et al. [50] investigated an evaporating meniscus in a channel using an augmented Young-Laplace and kinetic theory based model. They found the contribution of the micro-region to the overall heat transfer and consequently the temperature drop across the interface to be inversely proportional to the radius of the channel. The same group of authors also modeled evaporation from the meniscus at a distance from the capillary mouth into air by coupling the effects

of evaporation and diffusion [51]. Their results confirmed the experimental findings by the previous authors regarding the existence of a higher diffusion flux at the capillary wall.

Before delving further into this subject, it should be pointed out that having a clear picture of the temperature profile along an evaporating meniscus as well as the associated flow patterns adjacent to such an interface are crucial in elucidating the physics behind an evaporating meniscus in a capillary. Thus these subjects shall be briefly discussed in the following sections.

2.5.1 Temperature profile across an evaporating meniscus inside a capillary

Sufficient information about the temperature profile across an evaporating meniscus is a key to having a better understanding on which to model heat and mass transfer in this geometry. For instance, the regions with lower temperature are indicative of higher evaporation rates [47].

For a number of reasons, thermocouples, although commonly used, [33], have some disadvantages. First, they impose dimensional constraint (i.e. the smallest thermocouples could be orders of magnitude bigger than the dimension of the region of interest). Second, they prohibit mapping the temperature profile for the entire region of interest, and finally they are invasive in nature (since they alter the interface shape) [46–48].

In this section alternative techniques suggested by various authors are introduced to rectify these difficulties, as well as a brief overview of some experimental observations, and interpretations of spontaneous evaporation from capillary tubes.

Buffone et al. [46] used Thermo-chromic Liquid Crystals (TLCs) to map

the temperature gradient due to self-induced evaporation of a volatile liquid (pentane) in a capillary tube. TLCs are organic compounds that reflect light in a certain wavelength range determined by their temperatures, and thus could be used as temperature sensors. They found that for an evaporating meniscus the liquid is cooler near the tube wall (i.e. rim of the capillary) than it is at its apex. This finding suggests that the evaporation rate ought to be higher near the wall (i.e. micro-region). Their finding complimented the results reported previously by authors who hypothesized about the exitance of a temperature dip associated with higher evaporation rate at the micro-region [48, 52].

It is accepted that evaporation phenomena has a cooling effect due to the required energy input (i.e. latent heat of vaporization). In other words, the evaporation of liquids requires a heat supply equivalent to the latent heat of vaporization. In this case, the cooler region near the periphery of the meniscus is indicative of higher evaporation rate experienced at this section (i.e. the required energy is being taken from the liquid adjacent to the micro-region).

Buffone and Sefiane [47] conducted a series of experiments to further corroborate the notion of temperature gradient across an interface using Infra-Red (IR) measurements. They showed that indeed the temperature near the three phase contact point (i.e. at the periphery) is lower than at the center (indicating a non-uniform evaporation along the interface). It was demonstrated that this cooling effect near the wall is more pronounced for liquids with higher volatility and smaller capillaries [49, 53].

This observation is quite intriguing as it profoundly distinguishes the evaporation pattern between a convex and concave meniscus. As we discussed in the previous section of this Chapter, for a convex meniscus Duan et al. [30] reported a parabolic temperature profile with the minimum interfacial temperature oc-

curring at the centerline, whereas the experimental data for a concave meniscus divulges an opposite trend.

2.5.2 Flow patterns of an evaporating meniscus inside a cylindrical tube

As discussed in section 2.5.1, the cooling effect due to non-uniform evaporation of liquids induces a temperature gradient along the interface. Intuitively, this pattern is more vigorous for more volatile liquids (i.e. liquids with lower boiling point) [52]. Recall that for most liquids surface tension increases with a decrease in temperature. Thus, in the case of an evaporating meniscus formed inside a capillary tube, the surface tension would be higher near the corners of the capillary in comparison with the center line [46].

When the surface tension gradient is sufficiently strong, it induces a Poiseuille flow beneath the interface (i.e. from the center towards the edge of the tube) replenishing the liquid evaporating from the micro-region. This convective motion is also known as thermocapillary Marangoni convection [34, 53]. In other words, convection transfers heat and mass by driving hotter liquid to cooler regions (reducing the temperature gradient across the interface) and thus produce two axi-symmetrical (with respect to the capillary axis) counter rotating vortices beneath the interface [40–43, 49, 54]. An opposite pattern for a convex meniscus was observed where Marangoni convective rolls were reported to flow from the periphery towards the center line [30]. Fig. 2.4 schematically depicts the temperature variation and the consequent surface tension gradient of an evaporating concave meniscus inside a capillary.

This symmetrical pattern of counter rotating vortices induced due to viscous coupling could be distorted by thermocapillary-buoyancy driven convec-

tion when evaporation rate is higher (e.g. through external heating or under a reduced pressure environment).

It is worth mentioning that thermocapillary convection usually occurs in the regions adjacent to the interface, while buoyancy driven flow is due to the motion in the bulk phase. It was shown that the former is the dominating phenomenon in capillaries with diameters smaller than 1 mm while the latter is stronger at larger tube sizes [35].

Hemanth et al. [35,55] investigated the steady buoyant thermocapillary convection induced by uneven evaporation from a meniscus in horizontally oriented micro capillaries at atmospheric pressure. Using micro scale particle image velocimetry (μPIV) method visualization, they confirmed the existence of two axisymmetrical counter rotating vortices at the horizontal plane with the maximum velocity at the interface (as expected due to thermocapillary driven flow) located halfway between the centerline and the three phase contact line. In the case of small tube sizes (and methanol as the working fluid), the induced vortex pair was found to be symmetric; however, the symmetrical pattern was distorted for larger size tubes, possibly due to buoyancy-driven flow and gravitational effects.

2.5.3 Receding meniscus inside a capillary

Sefiane [52] et al. conducted a series of experiments for evaporation of volatile liquids inside small capillary tubes, evaporating to the surrounding environment (1 atm and $25°C$). They showed that the evaporation rate does in fact decrease as the meniscus recedes from the tube's mouth, a trend shared commonly between all the liquids and tube diameters they tested. The same group of authors also investigated evaporation from capillaries into dry air. They showed that

for a receding meniscus (of a volatile nature) inside a capillary, the evaporation was significantly reduced and the convective rolls almost disappear [43].

This observation supported the findings by Buffone et al. [53] which mapped the convective rolls and temperature gradient associating with an evaporating meniscus in a tube using μPIV method and an IR camera. The IR thermography measurements clearly demonstrated that the liquid thermocapillary convection was suppressed as the meniscus recedes farther from the capillary mouth.

This observed behavior could be due to changes in the vapor concentration above the meniscus. As the concentration of the vapor builds up the evaporation rate slows down, as possibly the result of faster evaporation of the vapor phase compared to diffusion out of the tube's open end. It was previously shown that evaporation from (volatile) liquids in their own vapor is much more subtle than that evaporating into air [56].

2.5.4 Effect of tube inner diameter on evaporation

It is expected that an increase in the tube diameter would contribute to higher evaporation rates (due to larger surface area) and a decrease in evaporation flux. Note that the average flux is calculated from the measured evaporation rate and surface area of the liquid vapor meniscus. Buffone et al. [57, 58] confirmed the results of Potash et al. [59] where it was shown that there exists an adverse linear relation between the evaporation mass flux (the ratio of total evaporation to the capillary surface area) and capillary diameter. According to their work, the total evaporation in the micro-region increased linearly with an increase in the diameter of the capillary. They stated that the width of the aforementioned region (where most evaporation takes place) increases linearly with the capillary diameter, and not by a square root factor.

Rice et al. [45] developed an analytical solution examining the evaporation of volatile liquids in capillary tubes that evaporated in ambient conditions. Their finding supported the experimental results by Buffone et al. [57,58]. They noted that the evaporation rate increases almost linearly with tube diameter, and the evaporation flux drops nearly as the inverse of the tube diameter.

More recently, Dhavaleswarapu et al. [35] used power curve fitting methods to relate mass flux and mass flow rate to the inner diameter of the tube. They found the proportionality to be a function of $D^{-0.5}$ and $D^{1.5}$ respectively. This finding suggests that the evaporation is distributed between two rate limiting bounds, the micro and macro regions of a meniscus formed inside a capillary tube. Finally, it is worth mentioning that the averaged evaporation fluxes in capillaries with rectangular cross section was found to be higher than that of capillary tubes [60].

Indeed further modeling is required for a better understanding of the dependence of evaporation rate on the tube size, and remains to be a topic for future research.

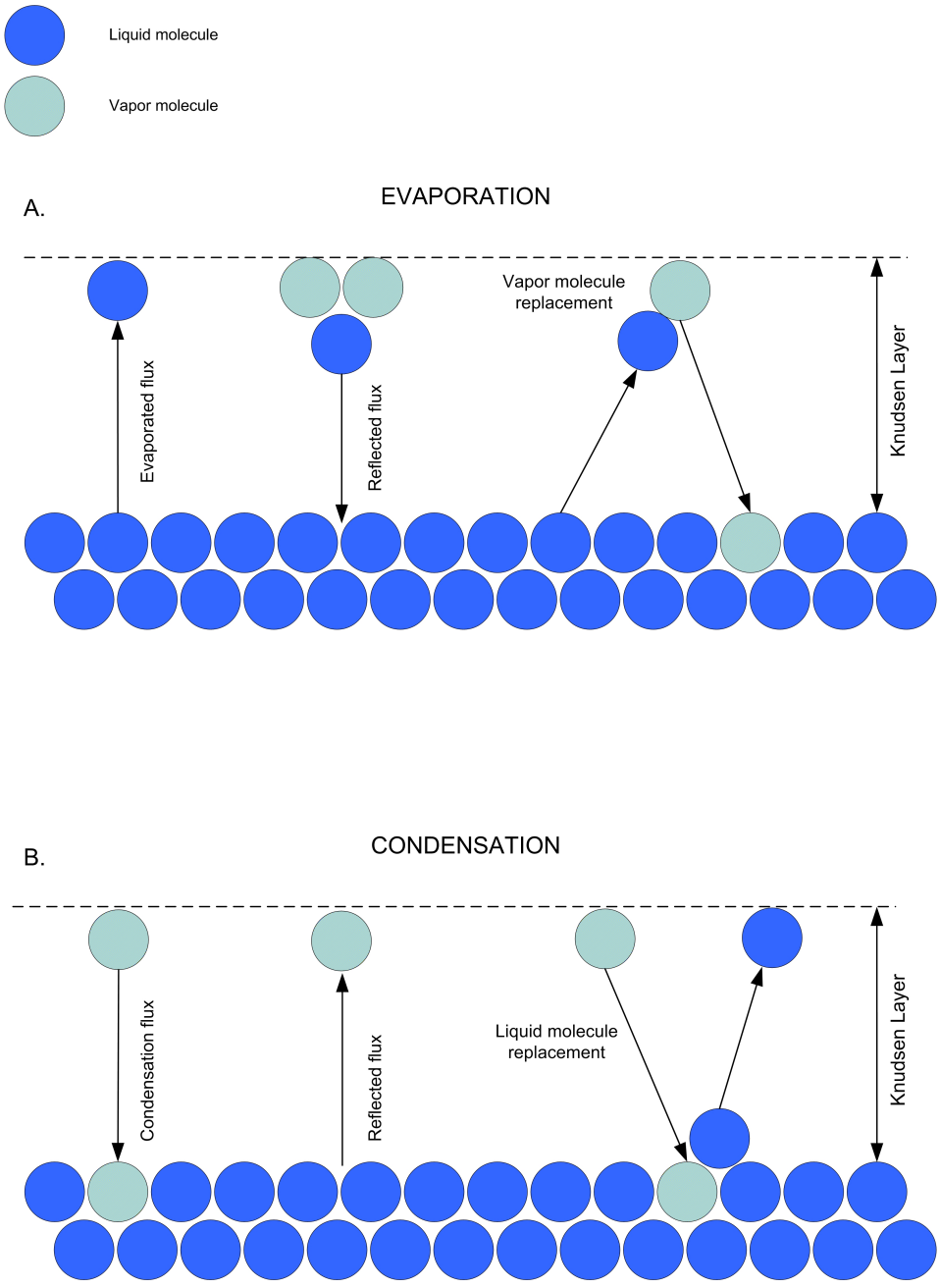

Figure 2.1: Schematic molecular arrangement of evaporation and condensation.

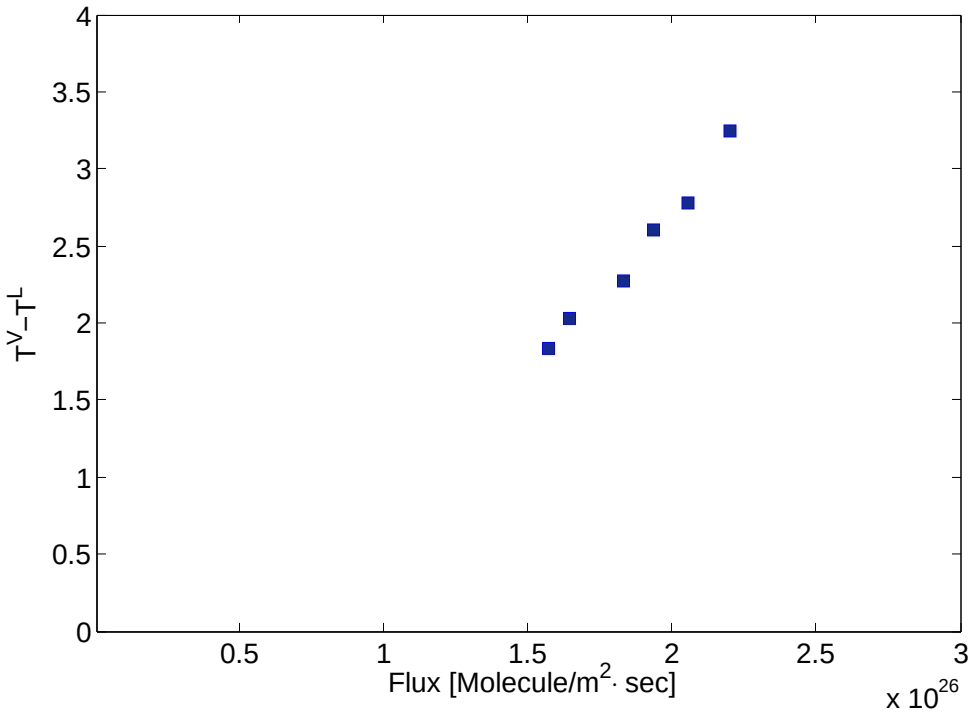

Figure 2.2: Temperature jump as a function of evaporation flux for a convex meniscus formed in a rectangular funnel. The temperature decreases almost linearly with a decrease in evaporation flux [1].

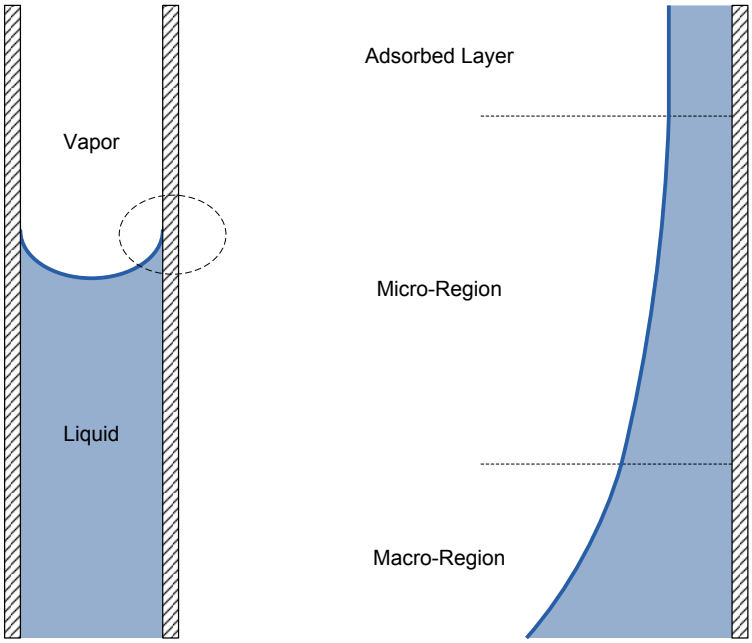

Figure 2.3: Layers of an evaporating meniscus.

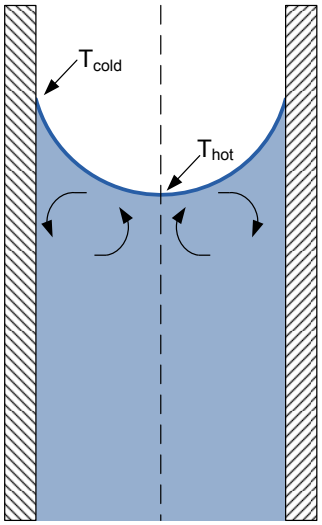

Figure 2.4: Schematic symmetrical counter rotating vortices in horizontal section due to thermocapillary convection.

Chapter 3

Review of derivation of governing equations

Material presented in this chapter is a review of work already in the open literature.

3.1 Introduction

Sasges et al. [2,61] analytically calculated the equilibrium conditions for a single component, isothermal, two phase fluid system in a gravitational field. They showed that for such a system the necessary conditions for equilibrium are the satisfaction of Laplace and Young equations, as well as the equality of chemical potentials of each phase along the interface, which is a key factor that previous authors had failed to show as a necessary condition for equilibrium. Intuitively, all these conditions must be satisfied simultaneously for such a system to be in equilibrium. Further, they showed that the chemical potential of the liquid and vapor phase could be used to constitute a relationship for the pressure profile within such a system. This significant notion enables one to determine the pressure profile in a closed system where it cannot be measured directly via experimental apparatus. In this chapter we shall adopt a similar procedure

in order to derive the equilibrium conditions as well as the pressure profile in our system of study. Finally, we discuss the numerical implementation used to determine the shape of the liquid-vapor meniscus in equilibrium, and how in combination with measurable physical geometrical variables the mean radius of curvature can be calculated. This information is used to analyze the shape of the bulk meniscus in order to calculate the liquid pressure at its apex. As we will discuss later, this is the only method available to determine the liquid phase pressure accurately enough as it cannot be measured directly using experimental apparatus.

3.2 Conditions for equilibrium

Consider a single component two phase system in a gravitational field that has constant volume, temperature, and is impermeable to mass transfer. This system is schematically shown in Fig. 3.1. Although the basic geometry is a simplification of what the actual system consists of, it provides a starting point in understanding equilibrium conditions and, as we will see later, the pressure profile of the actual system of study. To solve such a class of problems, one can use the classical thermodynamics postulatory approach [62].

The entropy, S, of any system using the fundamental Euler relation can be expressed as [37, 62]

$$S^j = \frac{U^j}{T} + \frac{P^j.V^j}{T} - \sum_{i=1}^{n} \frac{\mu_i N_i}{T}, \qquad j = L, V, \; and \; i = 1, 2, ..., n \tag{3.1}$$

where U and T are the total internal energy and temperature respectively. The pressure is denoted as P and V represents the total volume of the system. In

the equation above μ is the chemical potential, and the total number of moles of the ith component is shown by N. The superscripts L and V denote the liquid and vapor phases respectively. For liquid-vapor, solid-vapor and solid-liquid interphases, the total entropy can be written as [37, 63]

$$S^j = \frac{U}{T} - \frac{\gamma.A}{T} - \sum_{i=1}^{n} \frac{\mu_i N_i}{T}, \qquad j = LV, SV, \ and \ SL \tag{3.2}$$

where A is the surface area and γ is the surface tension. The superscript LV, SV or SL on a property associates it with the liquid-vapor, solid-vapor and solid-liquid interphases respectively.

For any system in a gravitational field the total energy of each phase consists of the internal energy, U, and the potential energy, Ψ, given as a function of position. In other words, the energy term is augmented to take into account the potential energy arising form the gravitational field [64]

$$\Psi = gz \sum_{i=1}^{n} W_i N_i \tag{3.3}$$

where W_i is the molecular weight of component i, g is the gravitational acceleration and z is the vertical elevation in the field with respect to a reference position. By adopting this definition, the entropy of a system in a gravitational field can be expressed as a function of position throughout its extent.

Introducing the Lagrangian multipliers λ_i and λ_0 into equations 3.1 and 3.2, let's define α and β such that

$$\alpha^j \equiv S' - \sum_{i=1}^{n} \lambda_i \ N_i' - \lambda_0 (U' + \Psi') \qquad j = L, V \tag{3.4}$$

and

$$\beta^{j} \equiv S^{''} - \sum_{i=1}^{n} \lambda_i \; N_i^{''} - \lambda_0 (U^{''} + \Psi^{''}) \qquad j = LV, SV, \; and \; SL \tag{3.5}$$

where α and β are the modified intensive entropy as a function of total energy and number of moles. In the equations above the superscript ($'$) and ($''$) indicate that the variable is divided by unit volume and unit interfacial area respectively. The total modified entropy of the system (see Fig. 3.1) may be written as

$$\begin{aligned} S^{*} \;=\; & \left\{ \left[\int_0^{Z_{b\circ}} \alpha^{L}.dV + \int_{Z_{b\circ}}^{Z_{bm}} \alpha^{L}.dV \right]_{liq} + \left[\int_{Z_{b\circ}}^{Z_{bm}} \alpha^{V}.dV + \int_{Z_{bm}}^{H} \alpha^{V}.dV \right]_{vap} \right. \\ & \left. + \left[\int_0^{Z_{bm}} \beta^{SL}.dA + \int_{Z_{bm}}^{H} \beta^{SV}.dA + \int \beta^{LV}.dA \right] \right\}_{bulk} + \cdots \\ & \left\{ \left[\int_0^{Z_{c\circ}} \alpha^{L}.dV + \int_{Z_{c\circ}}^{Z_{cm}} \alpha^{L}.dV \right]_{liq} + \left[\int_{Z_{c\circ}}^{Z_{cm}} \alpha^{V}.dV + \int_{Z_{cm}}^{h_c} \alpha^{V}.dV \right]_{vap} \right. \\ & \left. + \left[\int_0^{Z_{c\circ}} \beta^{SL}.dA + \int_{Z_{cm}}^{h_c} \beta^{SV}.dA + \int \beta^{LV}.dA \right] \right\}_{capillary} \end{aligned} \tag{3.6}$$

In order to select equilibrium states among the other possible thermodynamic configurations, we have to employ the equilibrium theorem by applying the extremum principle of entropy or, equivalently, find the corresponding stable configuration when the thermodynamic potential of the system is a minima.

This requires that the variations of S^{*} (the modified entropy of the system) subject to the constraints i.e. variations in S^{*} must vanish for all virtual displacements about the equilibrium state. In other words, using the classical thermodynamics postulatory approach enables one to determine the conditions that must be satisfied by the intensive properties when equilibrium exists. In-

deed, the Helmholtz extremum principle would be another alternative for the proposed constant volume and temperature system [37, 65]. However, the final results would be identical.

Solving equation 3.6 as a whole is rather cumbersome. Thus, in order to reduce the extent and complexity of the solution, we shall confine our calculations to finding the conditions for equilibrium of the meniscus, depicted in Fig. 3.1 and solve for the terms in the second curly brackets (i.e. S_m, entropy of the fluid in the capillary). Despite this though, we can extend the necessary conditions to the bulk phase keeping in mind that, they too have to be satisfied simultaneously for the system to be in equilibrium.

Using the Leibnitz integral rule [66], applying the constraints, considering that, h_c, the capillary length is a constant (thus $\frac{dh_c}{dz} = 0$) and simplifying gives

$$\begin{aligned}
\frac{dS_m}{dz} &= \int_0^{Z_{c\circ}} \frac{d\alpha^L}{dz}\,\pi R_c^2\,dz + \int_{Z_{c\circ}}^{Z_{cm}} \pi\left[\frac{d\alpha^L}{dz}\,(R_c^2 - x^2) + \alpha^L\left(\frac{-dx^2}{dz}\right)\right]dz \\
&+ \int_{Z_{c\circ}}^{Z_{cm}} \pi\left[\frac{d\alpha^V}{dz}\,x^2 + \alpha^V\left(\frac{dx^2}{dz}\right)\right]dz + \int_{Z_{c\circ}}^{Z_{cm}} \frac{d\alpha^V}{dz}\,\pi R_c^2\,dz \\
&+ \int_0^{\phi_{cm}} 2\pi\left(\frac{d\beta^{LV}}{dz}x(\phi_c)R_{1c}(\phi_c) + \beta^{LV}\frac{dR_{1c}x}{dz}\right)d\phi_c + \beta^{LV}2\pi x(\phi_c)R_{1c}(\phi_c)\frac{d\phi_c}{dz}\bigg|_{\phi_{cm}} \\
&+ \int_{Z_{cm}}^{h_c} \frac{d\beta^{SV}}{dz}\,2\pi R_c\,dz - \beta^{SV}(2\pi R_c)\frac{dZ_{cm}}{dz}\bigg|_{Z_{cm}} + \int_0^{Z_{cm}} \frac{d\beta^{SL}}{dz}\,2\pi R_c\,dz \\
&+ \beta^{SL}(2\pi R_c)\frac{dZ_{cm}}{dz}\bigg|_{Z_{cm}}
\end{aligned} \tag{3.7}$$

After grouping some of the terms in the equation above and equating to zero one finds

$$\mu_i^j + W_i g z = \left(\frac{-\lambda_i}{\lambda_0}\right) = const., \qquad j = L, V, LV, SV, SL \tag{3.8}$$

and the following result that the temperatures of each phase (L,V, LV, SV, and SL) are equal to each other. The remaining terms could be grouped into two sets of equations which then can be solved individually. Thus equation 3.7 reduces to

$$\int_{Z_{co}}^{Z_{cm}} \pi \left[\left(\frac{dx^2}{dz} \right) (\alpha^L - \alpha^V) \right] dz + \int_0^{\phi_{cm}} \beta^{LV} 2\pi \left[R_{1c}(\phi_c) \left(\frac{dx}{dz} \right) + x \frac{dR_{1c}}{dz} \right] d\phi_c = 0 \tag{3.9}$$

and

$$(2\pi R_c) \left(\beta^{SL} \frac{dZ_{cm}}{dz}\bigg|_{Z_{cm}} - \beta^{SV} \frac{dZ_{cm}}{dz}\bigg|_{Z_{cm}} + \beta^{LV} x(\phi_c) \frac{d\phi_c}{dz}\bigg|_{\phi_{cm}} \right) = 0 \tag{3.10}$$

Bashforth et al. [67] and Sugden [68], proposed the following geometrical relations for the dividing surface at the liquid-vapor interface (see Fig. 3.2.A.).

$$x = R_{2c} \sin\phi_c \tag{3.11}$$

Following the steps set by Sasges et al. [69], considering horizontal variations of the interface about the equilibrium state gives rise to a couple of additional differential geometry relations (see Fig. 3.2.C)

$$dx = \sin\phi_c \cdot dR_{1c} \tag{3.12}$$

$$dz = \sec\phi_c \cdot R_{1c} d\phi_c \tag{3.13}$$

where R_{1c} and R_{2c} are the principal radii of curvature of the liquid-vapor interface at the three phase line and ϕ_c is the angle of inclination to the horizontal.

Substituting equations 3.11 - 3.13 into equation 3.9 and expressing the terms as a function of, z, one can write

$$\int_{Z_{co}}^{Z_{cm}} \left[\left(\alpha^V - \alpha^L\right) - \beta^{LV} \left(\frac{R_{1c}\, R_{2c}}{R_{1c} + R_{2c}} \right) \right] dz = 0 \tag{3.14}$$

Since the choice of the integration region (i.e. dz) is arbitrary, the integrand must be equal to zero, thus

$$P_c^V - P_c^L = \gamma^{LV} \left(\frac{1}{R_{1c}} + \frac{1}{R_{2c}} \right) \tag{3.15}$$

The equation above is the well known Laplace equation for a curved interface. Equilibrium at the three-phase line requires the Young equation to be satisfied. Thus, considering the variations about the equilibrium configuration there is a corresponding virtual displacement at the three phase line as well as the interface. For the position of the dividing surface of the interphase the following geometrical relation can be obtained as depicted in Fig. 3.2.B [2, 70].

$$R_{1c}\, d\phi_{cm} = \sin\phi_{cm}\, dZ_{cm} \tag{3.16}$$

Substituting in 3.10 and using the identity $x(\phi_c)|_{\phi_{cm}} = R_c$, and considering that $\phi_{cm} = \pi/2 - \theta_c$, one finds the Young equation as the final condition for equilibrium of a curved surface in a gravitational field

$$\gamma^{SV} - \gamma^{SL} = \gamma^{LV} \cos\theta_c \tag{3.17}$$

where θ_c is the contact angle at the three phase line.

Equations 3.8, 3.15, 3.17 together with temperature equality between all phases constitute the necessary condition for equilibrium. As mentioned earlier, the same procedure can be adopted to find the equilibrium conditions for the bulk phase in this system. Intuitively, the final results will be similar to what was found for the meniscus. However, it should be emphasized that the conditions for equilibrium form a coupled system of equations. Thus, in order for any such system (see Fig. 3.1) to be in equilibrium, all the aforementioned necessary conditions have to be satisfied simultaneously.

3.3 Pressure

In the preceding discussion the equations for equilibrium were found. However, they represent the equilibrium conditions in a very general from. Thus, it is required to express them in a more traceable format for a constant volume and temperature, closed to mass transport system.

For a slightly incompressible liquid phase, κ, the isothermal compressibility, defined

$$\kappa \equiv -\frac{1}{\nu^L}\left(\frac{\partial \nu^L}{\partial P}\right)_{T=cte} \tag{3.18}$$

is a constant and satisfies the following condition

$$\left|\kappa(P^L - P_\infty)\right| \ll 1. \tag{3.19}$$

In the equation above P_∞ is the saturation pressure evaluated at the corresponding temperature. For a single-component system, the well known Gibbs-Duhem relation in terms of the chemical potential of the bulk phase may also be expressed as [62]

$$d\mu^j = -s^j dT + \nu^j dP^j \qquad\qquad j = L, V \tag{3.20}$$

where s and ν are the molar entropy and volume respectively.

The chemical potential for an incompressible fluid can be determined by putting equation 3.18 into equation 3.20 and performing an integration for an isothermal case. The integration constant may then be evaluated at the saturation pressure for the liquid phase, $P_\infty(T)$, and further simplified using equation 3.19 to give [71]

$$\mu^L(T, P^L) = \mu^L_\circ(T, P_\infty) + \nu^L_\infty \left(P^L - P_\infty\right) \tag{3.21}$$

where ν^L_∞ is the molar volume of the liquid evaluated at the saturated state. On the other hand, the vapor phase may be approximated as an ideal gas and its chemical potential may be written in terms of the saturation condition [71]

$$\mu^V(T, P^V) = \mu^V_\circ(T, P_\infty) + \overline{R}\, T \ln\left(\frac{P^V}{P_\infty}\right) \tag{3.22}$$

where $\overline{R}$ is the universal gas constant.

To proceed to rigorously calculate the pressure profile would require one to include the functional dependence of pressure on location. Evidently, the chemical potential of each bulk phase is an independent function of height which can be evaluated at any vertical position within the respected phase. Thus, substituting equation 3.21 in 3.8, the pressure difference between two arbitrary points z_a and z_b (where $z_a < z_b$) in the liquid phase may be expressed as [61]

$$P^L_{z_a} - P^L_{z_b} = \frac{Wg}{\nu^L_\infty}(z_b - z_a) \tag{3.23}$$

Adopting a similar approach the pressure difference in the vapor phase is then given by [61]

$$\frac{P^V_{z_a}}{P^V_{z_b}} = \exp\left[\left(\frac{Wg}{\overline{R}T}\right)(z_b - z_a)\right] \tag{3.24}$$

In a closed system as described earlier, the principal limitation stems from the prediction of the true pressure at the interface. This limitation is responsible for the difficulty in predicting the true phase pressure required for calculating other principal relations in such systems. It should be noted that the pressure can not be measured directly with the experimental apparatus [4, 72]. However, this conceptual complexity is circumvented by the proceeding mathematical formulation.

Employing the liquid-vapor boundary equilibrium condition, $\mu^L = \mu^V$, and using the Laplace equation to substitute for the pressure difference across the interface, the liquid pressure at the interface, P^L_I, is found to be

$$P_I^L = \frac{\overline{R}T}{\nu_\infty^L} \cdot \ln \left[\frac{P^L + \gamma \left(\frac{1}{R_1} + \frac{1}{R_2} \right)}{P_\infty} \right] + P_\infty \tag{3.25}$$

where the subscript I denotes the interface. Since the chemical potentials are independent and different functions of pressure, the vapor pressure at the interface, P_I^V, can be found by interchanging the terms in equation 3.25 and the use of Laplace equation (i.e. 3.15)

$$P_I^V = P_\infty \exp \left[\frac{\nu_\infty^L}{\overline{R}T} \left(P_I^L - P_\infty \right) \right] \tag{3.26}$$

3.4 Interface shape

As part of the process to determine the actual pressure of the liquid phase, the liquid-vapor interface shape formed in the system needs to be found. For this purpose we divide the meniscus shape into two regions.

First we calculate the shape of the interface for the liquid inside the capillary. In this case the interface is assumed to be symmetric. This can almost readily be obtained by using the approach first introduced by Bashforth and Admas [67, 68]. This mathematical approach was developed to investigate the capillary rise problem to obtain a real curvature ratio at the apex of meniscus. Bashforth et al. and Sugden stated that the two radii of curvature, R_1 and R_2, must be equal at the apex and equal to the mean radius of the curvature R^{LV}. This approach makes it possible to explicitly determine the meniscus shape in terms of measurable experimental parameters (i.e. the physical boundary con-

ditions) [73, 74].

Second, we also require to find a relation for the bulk interface shape between the saucer and the cylinder wall. Fig. 3.4 schematically depicts the bulk interface. As can be seen, due to the geometry of the container this portion is axisymmetric.

It should be pointed out that determining the shape of the liquid-vapor interface is of significant importance. Intuitively, by having the mean radius of curvature the pressure at the interface could be determined numerically which as we will see later could be used to obtain other key information about the system.

3.4.1 Meniscus shape in capillary

Consider a liquid-vapor interface in a micro capillary subject to a gravitational field. The meniscus is in equilibrium and is kept at a constant temperature. We wish to formulate an expression for the liquid phase pressure as a function of height relative to the interface.

Choosing the apex of the meniscus on the axis of the capillary, $Z_{c_\circ}$ as the reference point (i.e. the point where the phase boundary crosses the axis of rotation) and using equation 3.23, the liquid pressure at any point below the reference can be expressed as

$$P_c^L = P_{c_\circ}^L - \frac{Wg}{\nu_\infty^L}(Z - Z_{c_\circ}) \tag{3.27}$$

where the subscript $c_\circ$ indicates values at the apex of the meniscus (see Fig. 3.1). The vapor pressure for any arbitrary point above the meniscus level in the vapor phase is given by equation 3.24 and is found to be

$$P_c^V = P_{c_\circ}^V \exp\left[\frac{-Wg}{\overline{R}T}(Z - Z_{c_\circ})\right] \tag{3.28}$$

Finally, the Laplace equation relates the pressure difference across a curved interface to the curvature of the interface and surface tension

$$P_c^V - P_c^L = \gamma^{LV}\left(\frac{1}{R_{1c}} + \frac{1}{R_{2c}}\right) \tag{3.29}$$

As mentioned earlier R_{1c} and R_{2c} are the two principal radii of curvature. For any curved shell the two radii of curvature at an arbitrary point is obtained by drawing a normal to the surface at that particular point. If one passes a plane through the shell such that it includes the normal, the curved intersecting line between the plane and the surface defines the first radius of curvature. On the other hand, passing a second plane orthogonal to the first plane also containing the normal defines the second radius of the curvature. By rotating the first plane in a full circular path, there will be a radius at which the first radius has a global minimum, which is referred to as the principal radius of curvature. Corresponding to that, the second principal radius of curvature is in the second plane perpendicular to the first.

For the special case of an axisymmetric interface, there are numerical methods available to calculate its shape. Various authors have developed modules (i.e. axisymmetric drop shape analysis, also known as ADSA) to simulate the shape of any such droplet by using fundamental relations and the appropriate boundary conditions [74–76]. We shall adopt a similar procedure to obtain the equilibrium shape of the liquid-vapor boundary and its radius of curvature in this problem. In the case of a general irregular meniscus, the mathematical

approach is complex which is not in the scope of this thesis.

The pressure difference along the meniscus interface can be formulated by subtracting equations 3.27 and 3.28

$$P_c^V - P_c^L = P_{c_\circ}^V \exp\left[\frac{-Wg}{\overline{R}T}(Z - Z_{c_\circ})\right] - P_{c_\circ}^L + \frac{Wg}{\nu_\infty^L}(Z - Z_{c_\circ}) \tag{3.30}$$

This pressure difference must be equal to the Laplace equation, thus equating 3.30 to 3.29 gives

$$P_{c_\circ}^V \exp\left[\frac{-Wg}{\overline{R}T}(Z - Z_{c_\circ})\right] - P_{c_\circ}^L + \frac{Wg}{\nu_\infty^L}(Z - Z_{c_\circ}) = \gamma^{LV}\left(\frac{1}{R_{1c}} + \frac{1}{R_{2c}}\right) \tag{3.31}$$

However, it is more agreeable to interchange the vapor pressure for the liquid pressure on the left hand side of the equation above, which can be achieved by substituting $P_{c\circ}^L$ for $P_{c\circ}^V$ using the Laplace equation at the apex of meniscus. It should be noted that due to the axial symmetry of the interface, the curvature at the apex is constant in all directions. Finally, putting $2\,R_c^{LV}$ for the sum of $(1/R_{1c_\circ} + 1/R_{2c_\circ})$ results in

$$\left(P_{c_\circ}^L + \frac{2\,\gamma^{LV}}{R_c^{LV}}\right) \exp\left[\frac{-Wg}{\overline{R}T}\,(Z - Z_{c_\circ})\right] - P_{c_\circ}^L + \frac{Wg}{\nu_\infty^L}(Z - Z_{c_\circ}) = \gamma^{LV}\left(\frac{1}{R_{1c}} + \frac{1}{R_{2c}}\right) \tag{3.32}$$

The notion that the interface is axisymmetric about the z-axis relates the first principal radius of curvature, R_{1c}, to the arc length, $\mathbf{s}$, and the turning angle, ϕ_c, by the following geometrical relation (see Fig 3.3.B)

$$\frac{1}{R_{1c}} = \frac{d\phi_c}{d\mathbf{s}} \tag{3.33}$$

where the arc length is related to the radial and axial coordinates by

$$dx_I = d\mathbf{s}\cos\phi_c \tag{3.34}$$

and

$$dz_I = d\mathbf{s}\sin\phi_c \tag{3.35}$$

Putting equations 3.34 and 3.35 in 3.33 gives the following set of first order differential equations in terms of R_{1c}, $x(\phi_c)$, and $z(\phi_c)$

$$\frac{1}{R_{1c}} = \frac{\cos\phi_c\, d\phi_c}{dx_I} \tag{3.36}$$

and

$$\frac{1}{R_{1c}} = \frac{\sin\phi_c\, d\phi_c}{dz_I} \tag{3.37}$$

The second principal radius of curvature is related to the radial coordinate, x_I, as well as the turning angle, ϕ_c, by (see Fig. 3.3.A)

$$\frac{1}{R_{2c}} = \frac{\sin\phi_c}{x} \tag{3.38}$$

Then, one can substitute for R_{2c} in equation 3.32 using equation 3.38 and then non dimensionalize the subsequent relation using, R_c^{LV}, as length scale to obtain

$$\frac{P_{c_\circ}^L\, R_c^{LV}}{\gamma^{LV}}\left(\exp\chi_c - 1\right) + 2\exp\chi_c + B_{\circ c}(\bar{z} - \bar{z}_{c_\circ}) - \frac{\sin\phi_c}{\bar{x}} = \frac{1}{\bar{r}_{1c}} \tag{3.39}$$

where $\bar{r_1}$, $\bar{x}$ and $\bar{z}$ are the dimensionless principal radius of curvature, radial and axial coordinates respectively. The following identities were used in the equation above

$$\chi_c(\phi_c) = \frac{-R_c^{LV} W g}{\overline{R}T} \tag{3.40}$$

and

$$B_{oc} = \frac{(R_c^{LV})^2 \rho^L g}{\gamma^{LV}} \tag{3.41}$$

In the equation above, B_{oc}, is the Bond number, which is a measure to evaluate the effect of the gravitational field on the liquid-vapor interface. This number is the nondimensional ratio of gravitational force to surface tension. In our study, Bond numbers were calculated for various temperatures and found to be about 0.04. For values of less than 0.08, it was shown that the curvature is 1.5% less than that of a sphere [70, 72, 75]. However, this deviation from a spherical interface shape was included in the calculations.

Using equations 3.36 and 3.37 and substituting for $1/\bar{r}_{1c}$ in equation 3.39 forms the following set of first order differential equations [69]

$$d\bar{x}(\phi_c) = \frac{\cos\phi_c \, d\phi_c}{\vartheta(\phi_c) - \dfrac{\sin\phi_c}{\bar{x}}} \tag{3.42}$$

and

$$d\bar{z}(\phi_c) = \frac{\sin\phi_c \, d\phi_c}{\vartheta(\phi_c) - \dfrac{\sin\phi_c}{\bar{x}}} \tag{3.43}$$

where $\vartheta_c(\phi_c)$ is defined as

$$\vartheta_c(\phi_c) = \frac{P^L_{c_\circ} R^{LV}_c}{\gamma^{LV}} (\exp \chi_c - 1) + 2 \exp \chi_c + B_{\circ c}(\bar{z} - \bar{z}_{c_\circ}) \tag{3.44}$$

The shape of the axisymmetric liquid-vapor interface curve can then be calculated by numerical integration of the above set of equations (i.e. equations 3.42 - 3.44). In addition, the area of the interface, A^{LV}, may also be calculated by numerical integration of the following expression

$$A^{LV} = 2\pi (R^{LV}_c)^2 \int_0^{\phi_m} \frac{\bar{x}(\phi_c)}{\vartheta_c} d\phi_c \tag{3.45}$$

By examining equations 3.42 - 3.44 one finds that they also include the unknown $P^L_{c_\circ}$. However, the pressure at the apex of the meniscus is not considered an unknown since it can be obtained by combining the assumption of chemical potential equality along the interface and having the mean radius of the curvature (i.e. $\mu^L_I = \mu^V_I$). Thus, the vapor pressure is given by

$$P^V_I = P_\infty \exp \left[\frac{\nu^L_\infty}{\overline{R}T} (P^L_I - P_\infty) \right] \tag{3.46}$$

where the subscript I denotes the interface. Then putting P^V_I in Laplace equation the pressure at the apex of the meniscus is expressed as

$$P^L_{c_\circ} = P_\infty \exp \left[\frac{\nu^L_f}{\overline{R}T} (P^L_{c_\circ} - P_\infty) \right] - \frac{2\gamma^{LV}}{R^{LV}_c} \tag{3.47}$$

Solving the above equations would allow us to determine the value of the mean radius of the curvature and thereby estimate the pressure at the apex of the meniscus. However, these equations (i.e. 3.42 - 3.44) as written cannot be solved exactly, forcing us to discretize them and solve the above boundary value problem numerically. They form a coupled system of nonlinear, first order, differential equations that can be solved numerically using a standard numerical ordinary differential equation solver. In addition, we require boundary conditions (i.e. $\bar{x}(\phi)$ and $\bar{z}(\phi)$, the non-dimensionalized radius of the capillary and height of the meniscus respectively) in axial and radial coordinates. The numerical method used for this purpose is explained later in this chapter.

3.4.2 Meniscus shape formed between the saucer and the cylinder wall

The bulk meniscus shape entrapped between the saucer and the cylinder wall is schematically depicted in Fig. 3.4.

Choosing the bulk interface apex at $x = L$ and using equation 3.23, as shown previously, the liquid pressure at any arbitrary point below the bulk interface may be expressed as

$$P_b^L = P_{b_\circ}^L - \frac{Wg}{\nu_\infty^L}(Z_b - Z_{b\circ}) \tag{3.48}$$

where the subscript $b_\circ$ indicates values at the apex of the bulk meniscus. Using equation 3.24 the relation for vapor pressure above the meniscus can be formulated by

$$P_b^V = P_{b_\circ}^V \exp\left[\frac{-Wg}{\overline{R}T}(Z_b - Z_{b_\circ})\right] \tag{3.49}$$

Similar to what was shown previously, the pressure difference across the bulk interface can be formulated by subtracting equations 3.48 and 3.49. Substituting for $P_b^V - P_b^L$ using the Laplace equation gives

$$P_{b_\circ}^V \exp\left[\frac{-Wg}{\overline{R}T}(Z - Z_{b_\circ})\right] - P_{b_\circ}^L + \frac{Wg}{\nu_\infty^L}(Z - Z_{b_\circ}) = \gamma^{LV}\left(\frac{1}{R_{1b}} + \frac{1}{R_{2b}}\right) \quad (3.50)$$

It should be noted that at the apex the meniscus is symmetric with respect to the center line of the cylinder. However, the second radius of the curvature goes to infinity. Thus, the Laplace equation at this location would become [3]

$$P_{b_\circ}^V - P_{b_\circ}^L = \frac{\gamma^{LV}}{R_{1b_\circ}} \quad (3.51)$$

Using the equation above to substitute for $P_{b_\circ}^V$ in equation 3.50 results in

$$\left(P_{b_\circ}^L + \frac{\gamma^{LV}}{R_{1b_\circ}}\right)\exp\left[\frac{-Wg}{\overline{R}T}(Z - Z_{b_\circ})\right] - P_{b_\circ}^L + \frac{Wg}{\nu_\infty^L}(Z - Z_{b_\circ}) = \gamma^{LV}\left(\frac{1}{R_{1b}} + \frac{1}{R_{2b}}\right) \quad (3.52)$$

Following the same geometrical principals and using equations 3.33-3.35 gives the following set of first order differential equations that relates R_{1b}, x, z, and ϕ_b

$$\frac{1}{R_{1b}} = \frac{\cos\phi_b \, d\phi_b}{dx} \quad (3.53)$$

and

$$\frac{1}{R_{1b}} = \frac{\sin\phi_b \, d\phi_b}{dz} \tag{3.54}$$

The second principal radius of curvature for the meniscus is given by (see Fig. 3.4)

$$\frac{1}{R_{2b}} = \frac{\sin\phi_b}{x_b + L} \tag{3.55}$$

Then we can replace $1/R_{2b}$ in equation 3.52 to convert it into

$$\frac{P^L_{b_\circ} R_{1b_\circ}}{\gamma^{LV}} \exp(\chi_b - 1) + \exp\chi_b + B_{\circ b}(\bar{z} - \bar{z}_{b_\circ}) - \frac{\sin\phi_b}{\left(\bar{x}_b + \dfrac{L}{R_{1b_\circ}}\right)} = \frac{1}{\bar{r}_{1b}} \tag{3.56}$$

where

$$\chi_b(\phi) = \frac{-W g \, R_{1b_0}}{\overline{R}T} \tag{3.57}$$

and

$$B_{\circ b} = \frac{(R_{1b_\circ})^2 \rho^L g}{\gamma^{LV}} (\bar{z} - \bar{z}_{b_\circ}) \tag{3.58}$$

Finally, in an analogous manner to the geometrical analysis described earlier, the following set of differential equations can be found [3]

$$d\bar{x}(\phi_b) = \frac{\cos\phi_b \, d\phi_b}{\vartheta_b(\phi_b) - \dfrac{\sin\phi_b}{\bar{x} + \frac{L}{R_{1b_\circ}}}} \tag{3.59}$$

and

$$d\bar{z}(\phi_b) = \frac{\sin\phi_b \, d\phi_b}{\vartheta_b(\phi_b) - \frac{\sin\phi_b}{\bar{x} + \frac{L}{R_{1b_\circ}}}} \tag{3.60}$$

while $\vartheta_b(\phi_b)$ is defined as follows

$$\vartheta_b(\phi_b) = \frac{P^L_{b_\circ} R_{1b_\circ}}{\gamma^{LV}} \exp(\chi_b - 1) + \exp\chi_b + B_{\circ b}(\bar{z} - \bar{z}_{b_\circ}) \tag{3.61}$$

Similarly, the pressure at the bottom of the bulk meniscus is not known. However, it could be expressed as a function of the mean radius of curvature and other intensive properties. Equation 3.46 holds true for the vapor pressure at any interface in our system of study, similarly the liquid pressure at the apex of the bulk meniscus is given by

$$P^L_{b\circ} = P_\infty \exp\left[\frac{\nu^L_f}{\overline{R}T}(P^L_{b\circ} - P_\infty)\right] - \frac{\gamma^{LV}}{R_{1b\circ}} \tag{3.62}$$

3.5 Numerical implementation

The governing equations derived above can be employed to determine the shape of the phase boundary in equilibrium. This understanding in combination with observations from experiments, makes it possible to obtain the meniscus shape inside the capillary and that of the portion entrapped between the saucer and the cylinder wall. However, we shall limit our discussion to the estimation

of the shape of the meniscus as the other follows the same procedure with minor geometrical differences. With this in mind, the values for the surface tension, γ^{LV}, molecular weight, W, molar volume of the liquid, ν_{∞}^{L}, as well as the experimentally measured values of the cylinder radius, R_c, and height of the liquid meniscus, $Z_{co} - Z_{cm}$, are required for computation. As mentioned earlier, the shape of the equilibrium phase boundary can be determined by integrating equations 3.42 and 3.43 numerically form $\phi = 0$ to $\phi = \pi/2$. The boundary conditions for the meniscus shape can be defined by placing the coordinate reference at the apex of the meniscus

$$\phi(0) = 0\,,\ \bar{x}(0) = 10^{-18}\ \ and\ \ \bar{z}(0) = 0 \tag{3.63}$$

Since the liquid pressure at the apex is not known a priori, a range of values for the mean radius of curvature have to be hypothesized, R_{guess}. Starting with a guessed value, the liquid pressure, P_{co}^{L}, is calculated from equation 3.47 using the Newton-Raphson method (fsolve in Matlab v.7.4) and its value is returned to the main script that was developed to implement the procedure. The shape of the interface is then calculated by preforming a numerical integration of the set of ODEs using a fourth and fifth order Runge-Kutta algorithm (using the standard differential equation solver ODE45) with absolute error tolerance of 10^{-15} and adaptive step size to attain higher accuracy.

The maximum calculated value of the interface radius must be equal to the experimentally measured radius of the capillary

$$\bar{x}_m = \frac{R_c}{R_{guess}} \tag{3.64}$$

and the maximum calculated value for the interface height must be equal to measured interface height

$$\bar{z}_m = \frac{Z_\circ - Z_{cm}}{R_{guess}} \tag{3.65}$$

The corresponding axial and radial turning angle difference with respect to the physical boundary conditions is found by interpolation or extrapolation form the data array by

$$\Delta\phi_m = \phi(\bar{x}_m) - \phi(\bar{z}_m) \tag{3.66}$$

In the case that this difference was close to zero, the program would converge and the value of the mean radius of curvature, R^{LV}, was saved for future calculations. Otherwise, the program would choose a new guess value and repeat the procedure until the condition was satisfied. For the sake of brevity details of the mathematical procedure are not given here but can be found in texts in numerical methods [77].

To estimate the bulk meniscus shape a procedure analogous to that described above was utilized. Therefore, the shape of the liquid-vapor interface curve could be obtained by simultaneous integration of equations 3.59 and 3.60 for given boundary conditions and other required variables. It should be pointed out that the geometry of the container directly affects the vapor pressure at the apex of the bulk meniscus, so that the proposed boundary conditions are limited to the specific geometry that they were developed for. This might seem like a small achievement, however, calculation of the mean radius of the curvature is of significant importance as it is used to determine the pressure at the apex of

the meniscus, a crucial parameter in our studies that cannot be measured directly. The flowchart in Fig. 3.5 depicts this iterative procedure. The simulated meniscus shape inside the capillary, and between the saucer and cylinder wall is depicted in Fig. 3.6 and Fig. 3.7 respectively.

3.6 Summary

In this chapter we demonstrated that classical thermodynamics could be used to derive the equilibrium conditions as well as the pressure profile within the system being studied. From our discussion it should be apparent that by having certain geometrical dimensions of the interface and using numerical methods the mean radius of curvature could at the apex be estimated. This value may then be used to determine the liquid and ultimately the vapor phase pressure at the apex of the meniscus (formed in an isothermal, constant volume system that is impermeable to mass transfer), a property that cannot be measured using the experimental apparatus. In addition, having the vapor phase pressure at the apex of the bulk phase is crucial in determining the corresponding pressure at the meniscus formed inside the capillary. This finding allows detailed quantitative prediction of vapor pressure at the apex of capillary meniscus with respect to bulk phase as the reference point. Our studies in the following chapters are aimed at understanding each of these processes and the limiting role of vapor bulk pressure on the rate of evaporation from the capillaries.

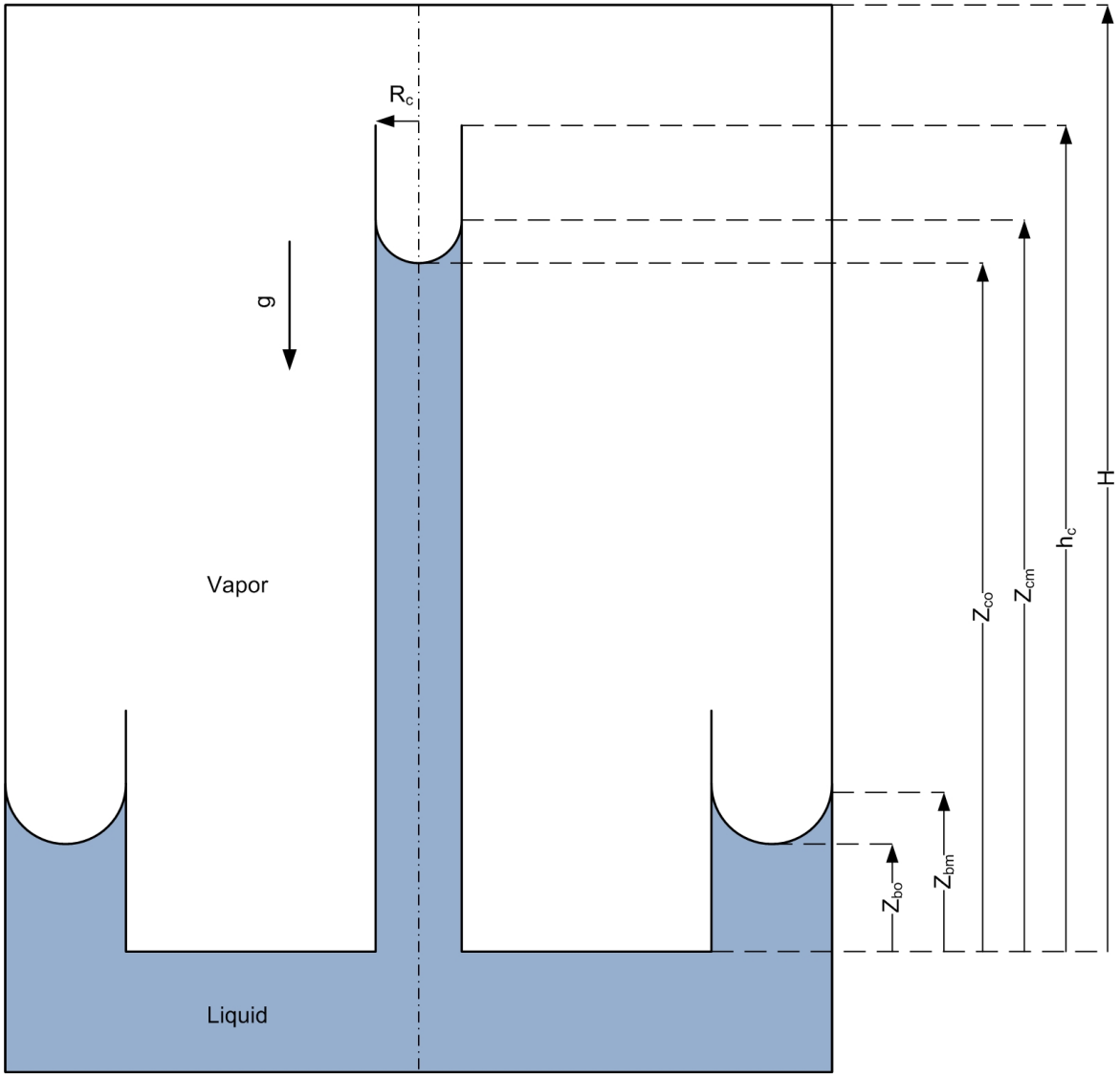

Figure 3.1: A schematic representation of system.

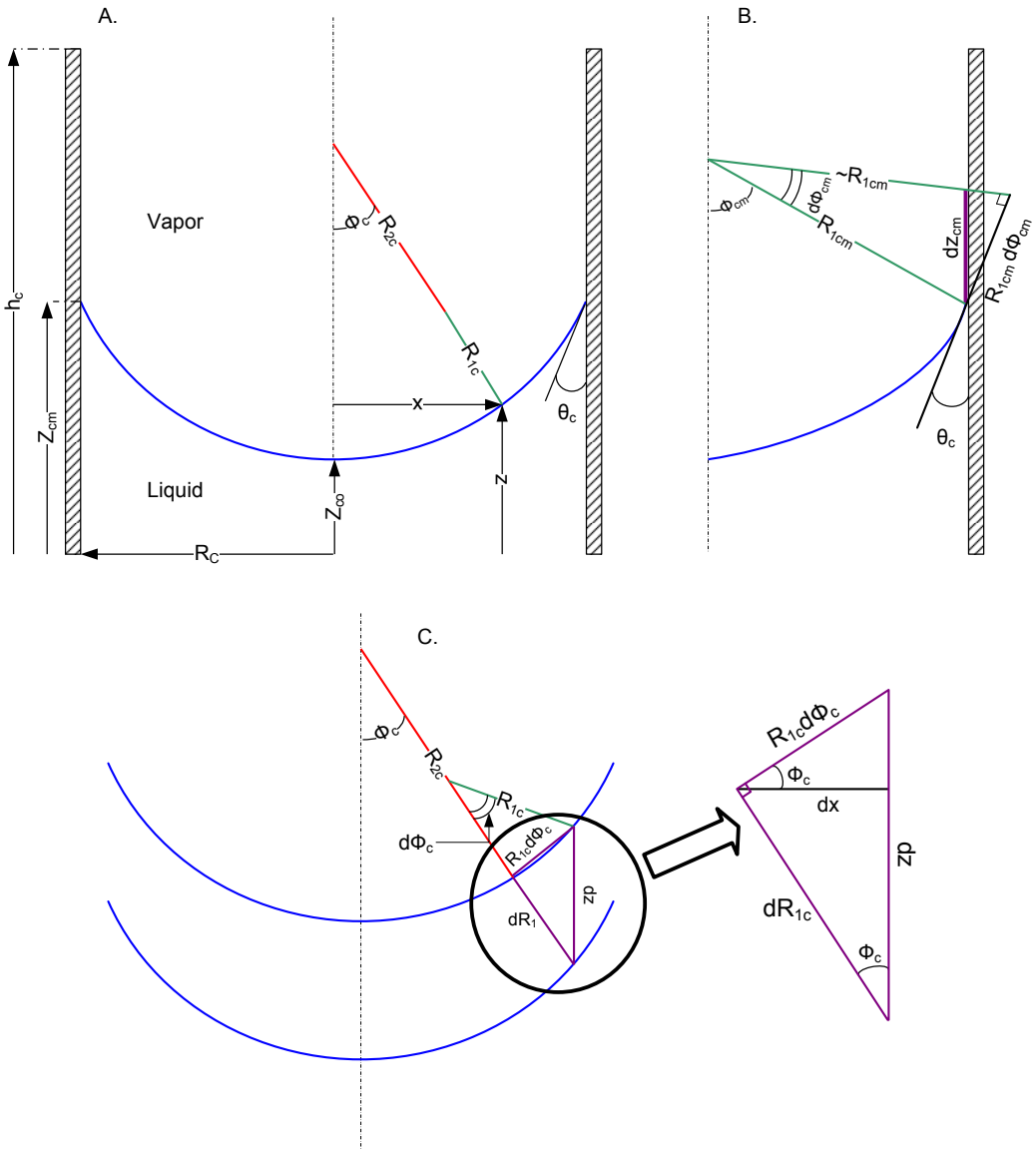

Figure 3.2: A. Schematic geometry of the system. R_{1c} and R_{2c} are the two collinear radii of curvature, the turning angle is denoted by ϕ_c. B. Virtual displacement of the three phase contact point. C. Virtual displacement of the interface [2].

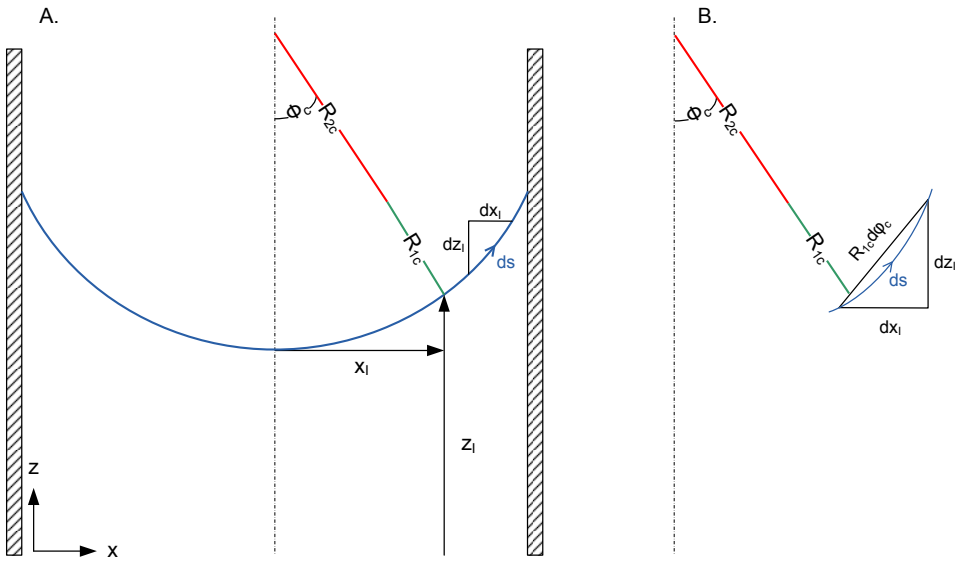

Figure 3.3: A. Schematic geometry of the capillary tube. B. Differential geometry of the interface.

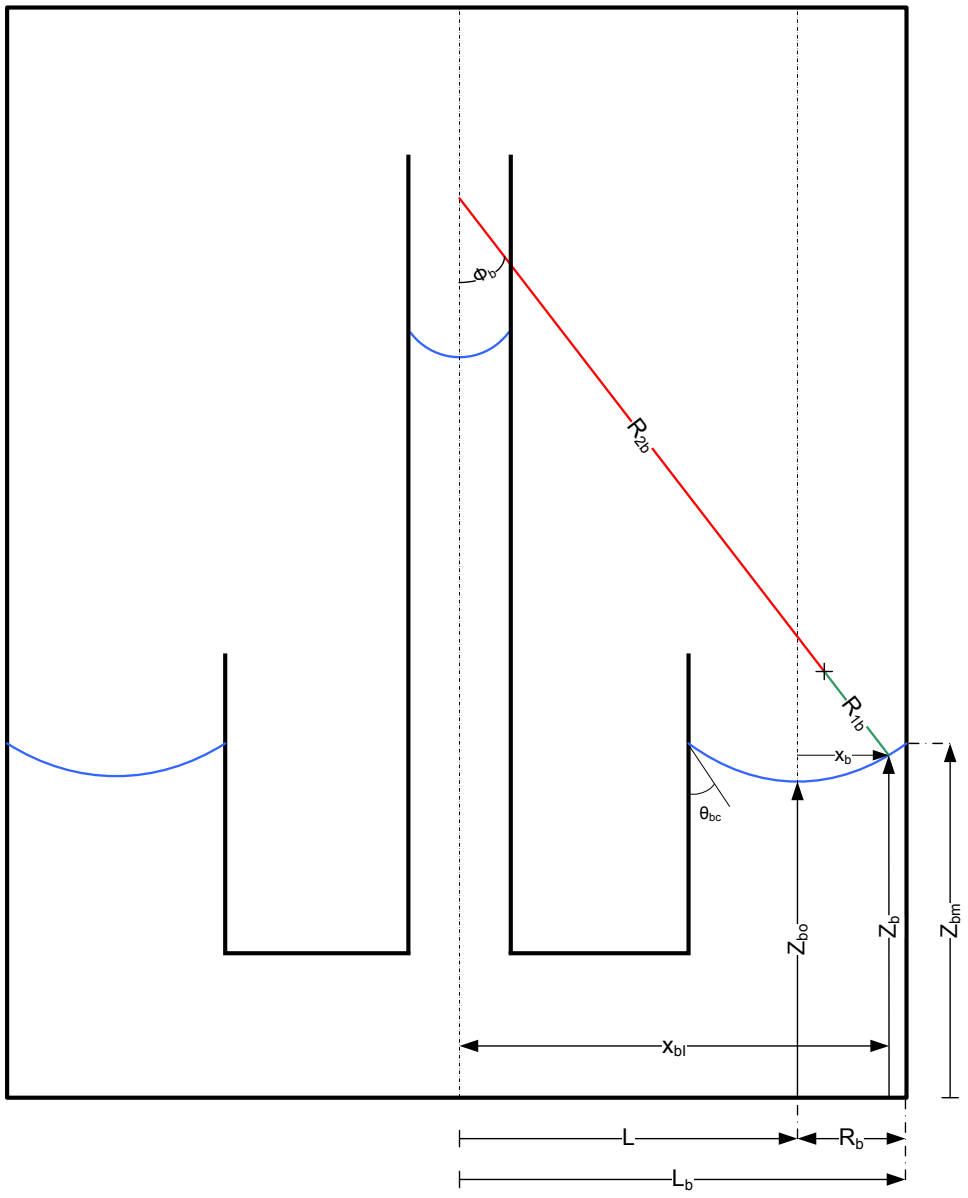

Figure 3.4: Schematic geometry of the meniscus formed between the saucer and the cylinder wall [3].

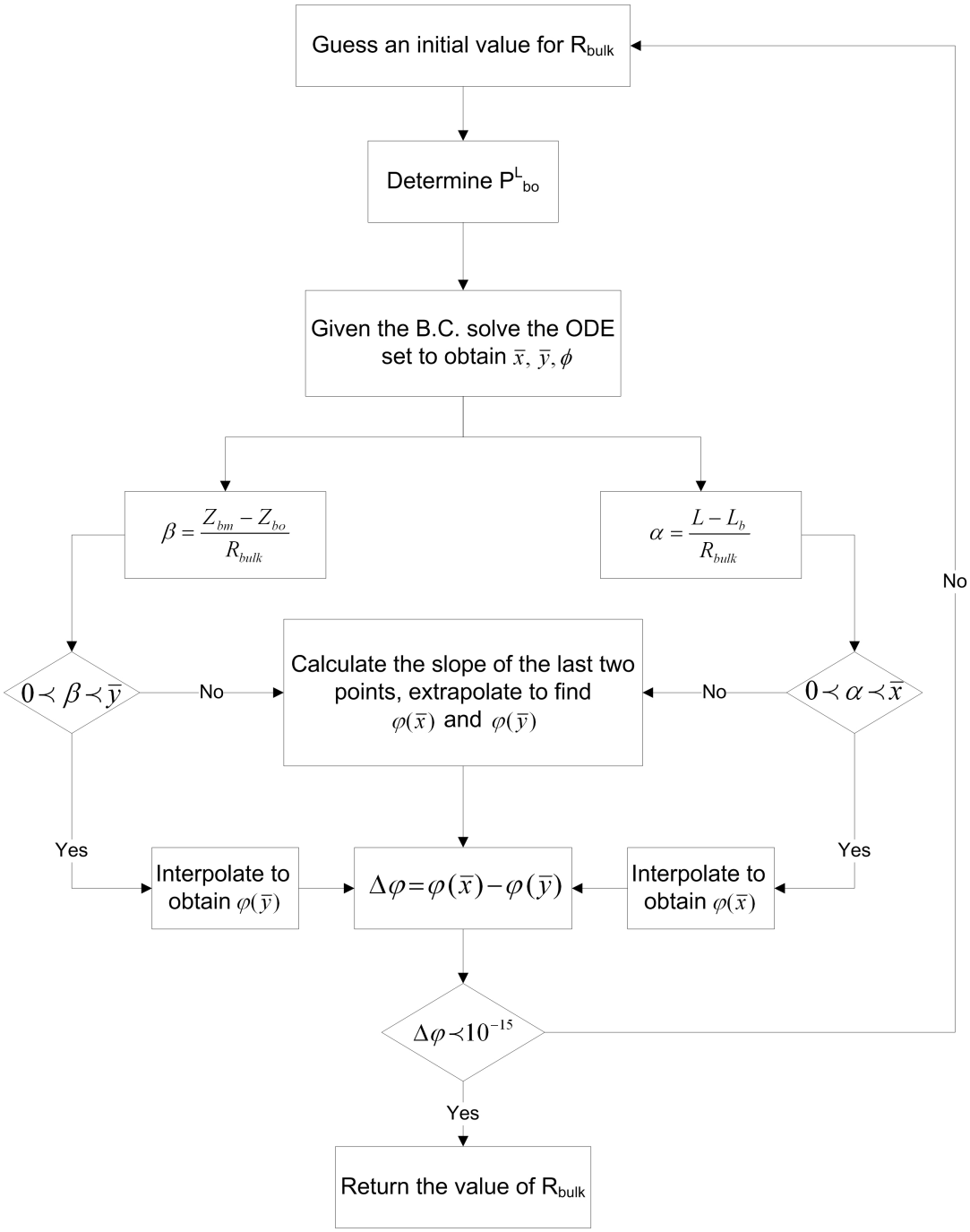

Figure 3.5: General procedure of determining bulk liquid radius of the curvature, R^{LV}_{bulk}.

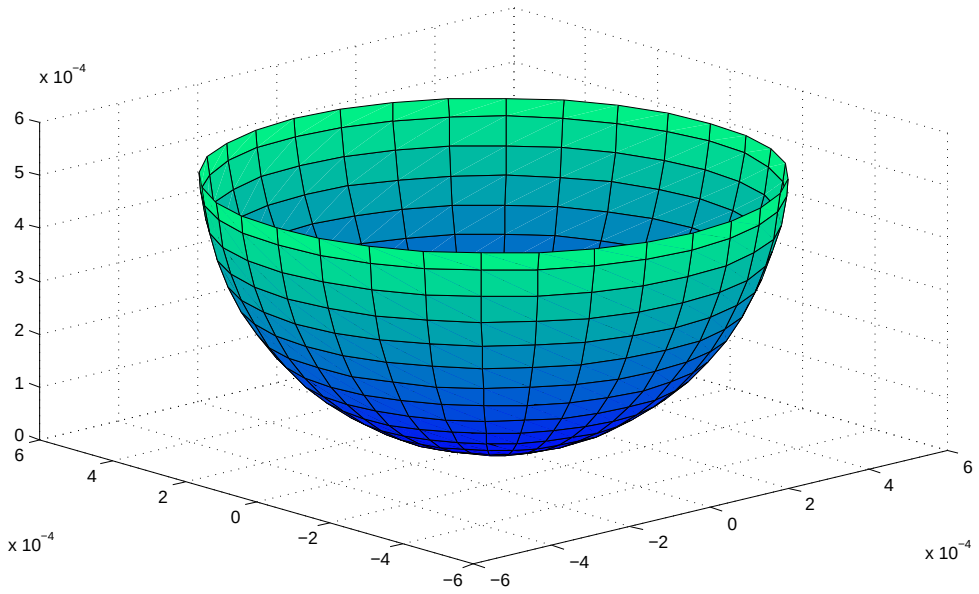

Figure 3.6: 3D image of the simulated meniscus $T = 40°C$, $R_c = 0.55mm$, $Z_{cm} - Z_{c\circ} = 0.45mm$, $R_c^{LV} = 0.56mm$, $B = 0.044$.

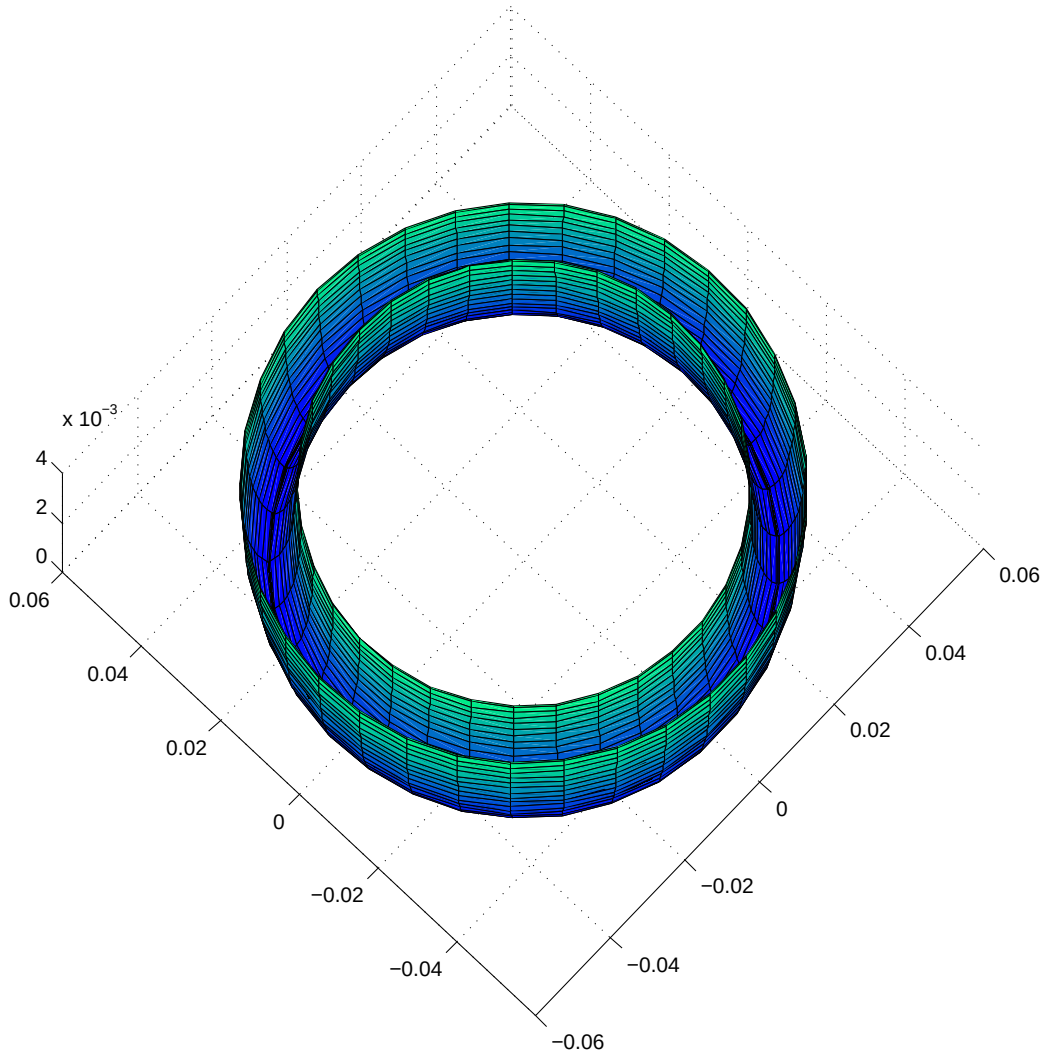

Figure 3.7: 3D image of the simulated bulk meniscus. $T = 40°C$, $Z_{bm} - Z_{bo} = 3.1mm$, $Lb = 47.72mm$, $R_b = 5.25mm$.

Chapter 4

Review of an expression for evaporation flux using SRT

Material presented in this chapter is a review of work already in the open literature.

4.1 Introduction

In order to answer questions about the effect of pressure on the rate at which liquids evaporate, it is necessary to understand the factors that play a significant role in this matter. In a sense, the governing equations that we wish to discuss in this chapter are the cornerstone upon which knowledge is built. However, in order to better answer any equations it is necessary to specify the detailed geometry, physical, and thermodynamical specifications of the system of our study. As we have seen in Chapter 3, the geometry, and physical conditions of the system are well defined. As a result, we have been able to obtain valuable information from solving the governing equations (described in Chapter 3).

Statistical rate theory (SRT) was introduced by Ward et al. in the 1980's. Many advances have been made by adoption and implementation of this theory in various nonequilibrium situations. In general, for an isolated system, SRT

could be used to predict an irreversible process to an equilibrium configuration which corresponds to the maximum number of available quantum mechanical states. There is a vast amount of literature available that has examined and validated this theory for various nonequilibrium processes. This methodology has been adopted as an approach to examine various physical rate phenomena, e.g. unsteady evaporation and condensation, gas adsorption on surfaces, membrane transport [78–80]. The results obtained from applying SRT to the aforementioned are in general agreement with the experimental measurements. In the case of an evaporating liquid, Fang et al. [27,28,81] developed an expression for the liquid evaporation flux in terms of measurable thermodynamic variables, as well as material and molecular properties. The intriguing factor about this method is the independence of the developed expression of fitting parameters for liquids with known molecular properties such as water. The SRT ability to predict the vapor phase pressure and its role on evaporation is amply resonated in the work done by Rahimi et al. [4,72]. In this chapter, we shall try to give a basic understanding of SRT and derive the governing equations for an evaporating liquid flux following the steps first set by Fang et al. [27], which will be used in analyzing the experimental data presented in chapter 6.

4.2 An expression for evaporation flux using SRT

Consider an isolated, isothermal, single component system. This system is comprised of liquid and vapor phases and is spatially homogenous. Let us assume that λ_f is the initial molecular distribution in the volume of this nonequilibrium system. At the initial time $t_\circ$, this configuration represents the

number of molecules of each respected phase, N^L and N^V, such that

$$\lambda_f \equiv (N^L, N^V) \tag{4.1}$$

If at an instant t, a liquid molecule evaporates from the liquid subvolume, its corresponding particle configuration , λ_g, can be expressed as

$$\lambda_g \equiv (N^L - 1, N^V + 1) \tag{4.2}$$

By following the standard procedure of first order perturbation analysis the probability of transition from molecular configuration λ_f to λ_g is given by [78,82]

$$\mathrm{P}(\lambda_f, \lambda_g, t) = \mathbf{K}'(\lambda_f, \lambda_g, t)\, \frac{\Omega(\lambda_g)}{\Omega(\lambda_f)} \tag{4.3}$$

where

$$\mathbf{K}'(\lambda_f, \lambda_g, t) = \frac{\omega(\bar{E})}{\hbar} |V_{nm}|^2\, t \tag{4.4}$$

In the equation above, $\omega(\bar{E})$ is the macroscopic state density of molecular configuration λ_f; the trace of the matrix elements corresponding to transition from state λ_f to λ_g is denoted by $|V_{nm}|$ and $\hbar$ is Plank's constant. It should be noted that for a given molecular distribution, $\omega(\bar{E})$ is approximated as a constant for the available range of quantum state in the system. The number of available quantum mechanical states of the isolated system, corresponding to the designated molecular distribution λ_f or λ_g, is denoted as $\Omega(\lambda)$.

For an arbitrary small volume, the transition probability per unit area can be obtained by applying the perturbation for a period of time δt to give [81]

$$\tau(\lambda_f, \lambda_g) = \mathbf{K}^{LV}(\lambda_f, \lambda_g) \frac{\Omega(\lambda_g)}{\Omega(\lambda_f)} \cdot \frac{\delta A}{\delta t} \tag{4.5}$$

where

$$\mathbf{K}^{LV}(\lambda_f, \lambda_g) = \frac{\omega(\bar{E})}{\hbar} |V_{nm}|^2 \cdot \frac{\delta t}{\delta A} \tag{4.6}$$

$\tau(\lambda_f, \lambda_g)$ in the equation above is the probability of transition at any instant in the time interval δt.

Assuming that for an isolated system in a particular molecular distribution all quantum states are equally probable, the Boltzmann definition for entropy of such system in a given molecular configuration (e.g. λ), in the view of statistical mechanics is given by [83]

$$S(\lambda) = k \ln \Omega(\lambda) \tag{4.7}$$

where k is the Boltzmann constant. Substituting for $\Omega(\lambda)$ in equation 4.5 using the equation above results in

$$\tau(\lambda_f, \lambda_g) = \mathbf{K}^{LV} \exp\left[\frac{S(\lambda_g) - S(\lambda_f)}{k}\right] \cdot \frac{\delta A}{\delta t} \tag{4.8}$$

Entropy is a particularly important thermodynamic function. We now wish to constitute a relation for changes in entropy of this system when the molecular distribution changes from λ_f to λ_g. For any such systems, the change in entropy

is equal to the difference of entropies between the virtual stages λ_g and λ_f of the liquid and vapor phase

$$S(\lambda_g) - S(\lambda_f) = \sum_i \left[S^i(\lambda_g) - S^i(\lambda_f)\right] \qquad i = L, V \tag{4.9}$$

Note that the outside of the system is considered to be insulated, such that the system forms an isolated system, and no reservoir needs to be considered. Further, making the assumption that the chemical potential of each phase as well as their temperature remain constant during this transition, the change in the entropy of this isolated system can be written as

$$\begin{aligned} S(\lambda_g) - S(\lambda_f) &= \left[\left(\frac{U^L(\lambda_g) + P^L V^L(\lambda_g)}{T^L}\right) + \left(\frac{U^V(\lambda_g) + P^V V^V(\lambda_g)}{T^V}\right)\right] \\ &- \left[\left(\frac{U^L(\lambda_f) + P^L V^L(\lambda_f)}{T^L}\right) + \left(\frac{U^V(\lambda_f) + P^V V^V(\lambda_f)}{T^V}\right)\right] \\ &+ \mu^L \left[\frac{N^L(\lambda_f) - N^L(\lambda_g)}{T^L}\right] + \mu^V \left[\frac{N^V(\lambda_f) - N^V(\lambda_g)}{T^V}\right] \end{aligned} \tag{4.10}$$

The equation above is too general to be applied directly, thus one needs to formulate an expression in terms of measurable intensive properties.
For this system to form an isolated system, the conservation of energy must be valid and is found to be

$$\left[H^L(\lambda_g) - H^L(\lambda_f)\right] + \left[H^V(\lambda_g) - H^V(\lambda_f)\right] = 0 \tag{4.11}$$

where H is the total enthalpy. Keeping in mind that during the change from molecular distribution λ_f to λ_g the number of molecules in each phase can be expressed as [78, 81, 82]

$$N^L(\lambda_f) - N^L(\lambda_g) = 1 \tag{4.12}$$

and

$$N^V(\lambda_g) - N^V(\lambda_f) = 1 \tag{4.13}$$

After applying equations 4.11-4.13 into equation 4.10, the entropy change in the isolated system when a single molecule is emitted from the surface becomes

$$S(\lambda_g) - S(\lambda_f) = h^V \left(\frac{1}{T^V} - \frac{1}{T^L} \right) - \left(\frac{\mu^V}{T^V} - \frac{\mu^L}{T^L} \right) \tag{4.14}$$

where h^V is the intensive entropy of the vapor phase (i.e. H^V/N^V). Substituting equation 4.14 into 4.8 gives the final form of evaporation probability of a single molecule at any instant of time

$$\tau(\lambda_f, \lambda_g) = \mathbf{K}^{LV} \exp \left[\frac{h^V}{k} \left(\frac{1}{T^V} - \frac{1}{T^L} \right) - \frac{1}{k} \left(\frac{\mu^V}{T^V} - \frac{\mu^L}{T^L} \right) \right] \cdot \frac{\delta A}{\delta t} \tag{4.15}$$

At the same instant, the probability of a liquid molecule leaving the surface (i.e. a condensing vapor molecule) needs to be considered. Thus, for the virtual case where a gas molecule adsorbs to the liquid interface (i.e. condensation), the molecular configuration, λ_e, of this nonequilibrium ensemble would be

$$\lambda_e \equiv (N^L + 1, N^V - 1) \tag{4.16}$$

In a similar manner, the probability of a transition from configuration λ_f to λ_e at any instant, t, in the time interval δt could be formulated as

$$\tau(\lambda_f, \lambda_e) = \mathbf{K}^{VL} \exp\left[\frac{S(\lambda_e) - S(\lambda_f)}{k}\right] \cdot \frac{\delta A}{\delta t} \tag{4.17}$$

Analogous to the procedure shown in the preceding section, the change in the entropy from molecular distribution λ_f to λ_e is found to be

$$S(\lambda_e) - S(\lambda_f) = -h^V \left(\frac{1}{T^V} - \frac{1}{T^L}\right) + \left(\frac{\mu^V}{T^V} - \frac{\mu^L}{T^L}\right) \tag{4.18}$$

Subsequently, by putting 4.18 in equation 4.17, the probability for condensation of a vapor molecule at any instant as a function of the intensive properties is expressed by

$$\tau(\lambda_f, \lambda_e) = \mathbf{K}^{VL} \exp\left[-\frac{h^V}{k}\left(\frac{1}{T^V} - \frac{1}{T^L}\right) + \frac{1}{k}\left(\frac{\mu^V}{T^V} - \frac{\mu^L}{T^L}\right)\right] \cdot \frac{\delta A}{\delta t} \tag{4.19}$$

As mentioned earlier, it is reasonable to assume that $\tau(\lambda_f, \lambda_g)$ (i.e. the instantaneous probability of a single molecule transport from liquid to vapor phase) remains constant during a small time period. Under such circumstances, one can relate the transferred number of moles in the given time difference to the probability of $\tau(\lambda_f, \lambda_g)$ [81, 84]

$$\Delta N^{LV} = \mathbf{K}_\circ^{LV} \exp\left(\frac{-\Delta S^{LV}}{k}\right) \cdot \Delta t \tag{4.20}$$

comparing $\mathbf{K}_\circ^{LV}$ with $\mathbf{K}^{LV}$ in equation 4.6 suggests that , $\mathbf{K}_\circ^{LV} = \mathbf{K}^{LV} \cdot C_\circ$, where $C_\circ$ is a proportionality constant.

Let us further assume that the intensive properties do not change appreciably during molecular transfer, ΔN, in any of the two possible directions (i.e. λ_f to λ_g or λ_f to λ_e) for transition time period Δt. Thus, the instantaneous unidirectional rate of molecular transition for the available particle distributions becomes [78]

$$J(\lambda_f, \lambda_g) = \mathbf{K}_\circ^{LV}.\tau(\lambda_f, \lambda_g) \tag{4.21}$$

following a similar pattern, the expression for the unidirectional rate of condensation becomes

$$J(\lambda_f, \lambda_e) = \mathbf{K}_\circ^{VL}.\tau(\lambda_f, \lambda_e) \tag{4.22}$$

It should be pointed out that equations 4.21 and 4.22 are only valid when the change in the number of molecules during the transition time period is much smaller than the total number of molecules of the respected phase. This is true for liquids with low volatility.

The expression for the net evaporation when the system is in molecular configuration λ_f, may be obtained by subtracting the forward and reverse expression of net rate of molecular transfer (i.e. equations 4.21 and 4.22 respectively).

However, before we proceed, it is important to further elucidate , $\mathbf{K}_\circ$, the average probability of transition. Let us assume that the isolated system is in its initial configuration λ_f with two possible neighboring particle distributions λ_g and λ_e. This system will then evolve to an equilibrium configuration λ_{eq} with the neighboring distributions λ_m and λ_n. The transition between microscopic states of neighboring quantum states may be represented as [85]

$$\cdots \lambda_e \leftharpoondown \lambda_f \rightharpoonup \lambda_g, \cdots, \lambda_m \leftharpoondown \lambda_{eq} \rightharpoonup \lambda_n, \cdots \tag{4.23}$$

In statistical rate theory it is further assumed that the average probability for any instantaneous quantum molecular transition between the neighboring states remains equal for any two neighboring configurations (in a given temperature range) in an isolated system.

$$\mathbf{K}_{\circ}^{LV}(\lambda_f, \lambda_g) = \mathbf{K}_{\circ}^{VL}(\lambda_f, \lambda_e) = \cdots = \mathbf{K}_{\circ}^{LV}(\lambda_{eq}, \lambda_n) = \mathbf{K}_{\circ}^{VL}(\lambda_{eq}, \lambda_m) \tag{4.24}$$

where $\mathbf{K}_{\circ}^{LV}$ (is a constant and) is defined as the average probability of forward molecular transition (i.e. when a molecule evaporates), and is assumed to be as probable as the quantum molecular transition in the reverse direction $\mathbf{K}_{\circ}^{VL}$ (i.e. when an impinging gaseous molecule condenses).

The conditions for equilibrium of the isolated system can almost readily be obtained. Suppose that the system has reached an instantaneous equilibrium state, thus it is required that the variations of F (the Helmholtz function) must go to zero for all virtual micro states about the equilibrium state. Under the equilibrium conditions one finds that the temperature and chemical potential of the liquid and vapor phase must be equal (i.e. $\mu_e^L = \mu_e^V$ and $T_e^L = T_e^V$). Making the assumption that the liquid phase volume is large enough, the equilibrium temperature would be equal to the instantaneous liquid temperature (i.e. $T_e = T^L$).

Then, the two possible entropy changes due to molecular transition about the equilibrium distribution, λ_e, are found to be [81, 85]

$$S(\lambda_m) - S(\lambda_{eq}) = \left(\frac{\mu_e^L}{T^L} - \frac{\mu_e^V}{T^L}\right) + h_e^V \left(\frac{1}{T^L} - \frac{1}{T^L}\right) \tag{4.25}$$

and

$$S(\lambda_n) - S(\lambda_{eq}) = -\big[S(\lambda_m) - S(\lambda_{eq})\big] \tag{4.26}$$

Consequently, in the view of equilibrium conditions, equations 4.25 and 4.26 go to zero. Thus, at any instantaneous equilibrium state the expression for unidirectional evaporation flux (using equation 4.21) becomes

$$J_{eq}^{LV} = \mathbf{K}_{\circ}^{LV} \tag{4.27}$$

and similarly for condensation (using equation 4.22) we have [86]

$$J_{eq}^{VL} = \mathbf{K}_{\circ}^{VL} \tag{4.28}$$

Due to the prevailing fact that under equilibrium conditions the unidirectional evaporation and condensation must be equal, one can deduce the following from the equations above (i.e. 4.27 and 4.28)

$$\mathbf{K}_{\circ}^{LV} = \mathbf{K}_{\circ}^{VL} = \mathbf{K}_{eq} \tag{4.29}$$

This assumption is essential to construct an expression for $\mathbf{K}_{eq}$ as a function of measurable thermodynamic properties.

The expression for the molecular exchange rate between the liquid and vapor phases is given in the equations above. To complete the expression for the

unidirectional molecular exchange, an expression for the equilibrium exchange rate, $\mathbf{K}_{eq}$, is essential. An expression for this value may be determined from a physical model. The assumption for this approximation requires the vapor phase to behave as an ideal gas, and the condensation of every impinging vapor molecule. As a result, the equilibrium exchange rate would be equal to the frequency of the vapor molecules striking the liquid-vapor interface [79, 87]

$$K_{eq} = P_e^V \frac{\Lambda}{\hbar} \tag{4.30}$$

where P_e^V is the vapor pressure at equilibrium and Λ is the thermal de Broglie wavelength which is defined as [83]

$$\Lambda = \frac{\hbar}{\sqrt{2\pi m k T_e}} \tag{4.31}$$

In the equation above, the mass of the molecules exchanged between the two phases is denoted by m.

The conditions for equilibrium of an isothermal, constant volume, single component two phase system were determined when the Helmholtz function is a minima. These necessary conditions require the equality of chemical potentials as well as the equilibrium temperature of each phase.

Having the liquid phase approximated as a slightly incompressible fluid, the vapor phase as an ideal gas and choosing the saturation condition as the reference state, the chemical potentials of each phase may be expressed using using equations 3.21 and 3.22

$$\mu^L = \mu_\circ(T^L, P_\infty) + \nu_\infty^L \left[P_e^L - P_\infty(T^V) \right] \tag{4.32}$$

and

$$\mu^V = \mu_\circ(T^L, P_\infty) + k\,T^V \ln\left[\frac{P_e^V}{P_\infty(T^V)}\right] \tag{4.33}$$

where $\mu_\circ(T^L, P_\infty)$ is the reference chemical potential at the liquid temperature. Under equilibrium conditions, one can equate equations 4.32 and 4.33 to construct an expression for P_e^V resulting in [4, 80]

$$P_e^V = \eta\, P_\infty(T^L) \tag{4.34}$$

where η is defined as

$$\eta = \exp\left\{\frac{\nu_\infty^L}{kT^L}\left[P_e^L - P_\infty(T^L)\right]\right\} \tag{4.35}$$

By having P_e^V as a function of P_e^L, we may now express the equilibrium exchange rate in a tractable format. Putting equation 4.34 and 4.35 in 4.30 gives

$$\mathbf{K}_{eq} = \eta P_\infty(T^L)\frac{\Lambda}{\hbar} \tag{4.36}$$

The net evaporation can be obtained by the difference between J^{LV} and J^{VL}, from equations 4.21 and 4.22 is expressed by [88]

$$J = 2\,\mathbf{K}_{eq}\sinh\left(\frac{\Delta S^{LV}}{k}\right) \tag{4.37}$$

The equation above as expressed cannot be directly used, forcing one to use molecular statistical definition of chemical potential and enthalpy to incorporate the aforementioned as a function of available physical as well as molecular

properties. In the next section, we shall use the statistical thermodynamic approach to approximate the vapor phase as an ideal polyatomic gas, a method suggested by previous authors to circumvent this problem.

4.3 Governing equations, an expression for net evaporation flux

The SRT governing equation for unidirectional flux in an isolated, isothermal, single component two phase system, has been derived. However, this equation is too general to be applied directly. Thus, we shall express the governing equations and the flux in terms of measurable thermodynamic properties. For this purpose, we shall follow the steps set by Fang et al. [27, 28, 81, 84].

In a similar manner, we shall adopt the statistical thermodynamics approach towards constituting the necessary relationships for the vapor phase. Considering distilled deionized water as the working fluid, the water vapor may be approximated as an ideal polyatomic gas.

For an ideal polyatomic gas the well known Bose-Einstein and Fermi-Dirac statistics (i.e. Boltzmann statistics) and the Born-Oppenheimer approximation can be adopted to find the corresponding thermodynamic expressions. For a system of independent and indistinguishable gaseous molecules the canonical ensemble partition function in classical limit is given by [83, 89, 90]

$$Q^g = \frac{1}{N!} q^N(V,T) \tag{4.38}$$

where neglecting the nuclear internal partition function we have

$$q(V,T) = q_{tr}(V,T)\, q_r(T)\, q_\omega(T)\, q_e(T) \tag{4.39}$$

In the equation above, $q_{tr}(V,T)$, $q_r(T)$, $q_\omega(T)$, and $q_e(T)$ are the translational, rotational, vibrational, and electronic partition functions respectively. Assuming that these Hamiltonians are rigorously separable, the molecular partition

functions for a polyatomic molecule are defined as follows;

The translational partition function is given by [83, 90]

$$q_{tr} = \left[\frac{2\pi kT\sum m}{\hbar^2}\right]^{3/2} V \tag{4.40}$$

where the sum is over all atomic masses of the molecule, $\hbar$ is the Plank's constant and V is the volume.

The rotational partition function may be expressed as

$$q_r = \frac{\pi^{1/2}}{\sigma}\left(\frac{8\pi kT}{\hbar^2}\right)^{3/2}\prod_i^3 I_i^{1/2} \tag{4.41}$$

where σ is the symmetry number and is defined as the number of ways a molecule can be rotated to be in the same configuration, when like atoms are treated as indistinguishable (e.g. $\sigma = 2$ for H_2O). I is the principle moment of inertia and can be determined for a known molecular structure.

The vibrational partition function is formulated by

$$q_\omega = \prod_{i=1}^{i_\circ}\frac{\exp\left(\frac{-\Theta_{vib}(i)}{2T}\right)}{1-\exp\left(\frac{-\Theta_{vib}(i)}{T}\right)} \tag{4.42}$$

where $i_\circ = 3n-5$ or $i_\circ = 3n-6$ for a linear or nonlinear polyatomic molecule respectively (e.g. $i_\circ = 3$ for H_2O). $3n$ is the number of normal coordinates (associated with vibration). The characteristic vibrational temperature is given by [83]

$$\Theta_{vib}(i) = \frac{\hbar\omega_i}{k} \tag{4.43}$$

In practice, the ω_i for polyatomic molecules must be deduced empirically from vibrational spectroscopy (Infrared and Raman) methods (see Fig. 4.1) [91, 92].

Finally, the electronic partition function for nearly all polyatomic molecules is ascribed by the ground electronic state. This is due to the high separation in electronic energy levels compared with kT, thus

$$q_e = \omega_{e1} \exp\left(\frac{D_e}{kT}\right) \tag{4.44}$$

where ω_{e1} is the state degeneracy and is equal to unity for chemically saturated molecules, and D_e is the depth of the potential minimum relative to the reference point.

Substituting equations 4.40 through 4.44 into equation 4.38, gives the final form of the canonical ensemble partition function for a system comprised of independent and indistinguishable gaseous molecules. Thus, we can move to the next step and derive the governing relations for such a system with the help of statistical thermodynamics.

4.4 Thermodynamic functions

In the view of statistical thermodynamics, the Helmholtz function may be expressed in terms of the partition function of the gaseous polyatomic molecules, Q^g (equation 4.38) [37]

$$F = -kT \ln Q^g \tag{4.45}$$

Substituting equations 4.38-4.44, using the well known Stirling approximation for the logarithm of the factorial of large numbers and the identity ($PV = NkT$) for an ideal gas, the Helmholtz function for the gas phase in the light of statistical thermodynamics is expressed by

$$F^g = -NkT \ln\left(\frac{\Phi}{P}\right) \tag{4.46}$$

where

$$\Phi = \left(\frac{2\pi \sum m}{\hbar^2}\right)^{3/2} (kT)^{5/2} e\, q_r q_v q_e \tag{4.47}$$

The internal energy in terms of partition function is defined as

$$U^g = NkT^2 \left(\frac{\partial \ln q(T, V/N)}{\partial T}\right)_{N,V} \tag{4.48}$$

thus, by putting equations 4.38-4.44 into the equation above and taking a partial derivative with respect to temperature while treating volume and the number of moles as constants gives

$$U^g = NkT \left\{ 3 + \frac{1}{T} \sum_{i=1}^{i_\circ} \left[\frac{\Theta_{vib}(i)}{2} + \frac{\Theta_{vib}(i) \exp\left(\frac{-\Theta_{vib}(i)}{T}\right)}{1 - \exp\left(\frac{-\Theta_{vib}(i)}{T}\right)} \right] - \frac{D_e}{kT} \right\} \tag{4.49}$$

In order to determine the expression for the entropy of the gaseous phase, one can use Legendre's transform of the Helmholtz function

$$F^g = U^g - TS^g \tag{4.50}$$

Putting equations 4.46 and 4.49 in the above and solving for S^g, the entropy of the vapor phase may be written as

$$\begin{aligned} S^g &= Nk\left\{\ln\left[\left(\frac{2\pi\sum m}{\hbar^2}\right)^{3/2}\frac{(kT)^{5/2}}{P^V}\right] + \ln q_r + \ln\omega_{e1}\right. \\ &+ \left.\sum_{i=1}^{i_\circ}\left[\frac{\left(\frac{\Theta_{vib}(i)}{T^V}\right)\exp\left(\frac{-\Theta_{vib}(i)}{T^V}\right)}{1-\exp\left(\frac{\Theta_{vib}(i)}{T^V}\right)} - \ln\left(1-\exp\left(\frac{\Theta_{vib}(i)}{T^V}\right)\right)\right] + 4\right\} \end{aligned} \tag{4.51}$$

In classical thermodynamics, the enthalpy is defined as

$$H^g = U^g + PV \tag{4.52}$$

Using the ideal gas law to substitute for PV in equation 4.49 and simplifying, the enthalpy of the vapor phase may be expressed as

$$H^g = NkT^V\left\{4 + \frac{1}{T^V}\sum_{i=1}^{i_\circ}\left[\frac{\Theta_{vib}(i)}{2} + \frac{\Theta_{vib}(i)\exp\left(\frac{-\Theta_{vib}(i)}{T^V}\right)}{1-\exp\left(\frac{-\Theta_{vib}(i)}{T^V}\right)}\right] - \frac{D_e}{kT^V}\right\} \tag{4.53}$$

Finally, we require the expressions for the chemical potential of each phase. This can readily be done using the definition of Gibbs free energy [62]

$$G = F + PV = \mu N \tag{4.54}$$

Thus, the chemical potential of the vapor phase becomes

$$\mu^g = \mu_s(T^V) + kT^V \ln P^V \tag{4.55}$$

where $\mu_s(T)$ is referred to as the standard chemical potential and is defined as

$$\mu_s(T) = -kT \ln\left(\frac{\Phi}{e}\right) \tag{4.56}$$

By comparing equation 3.22 for the chemical potential of the vapor phase with the equation above it can be deduced that

$$\mu_\circ^V \equiv \mu_s(T^V) + \ln P_\infty(T^V) \tag{4.57}$$

As mentioned before, in equilibrium conditions the chemical potentials are equal, this forces the constant of integrals evaluated at the saturation condition to be equal as well, thus

$$\mu_\circ^L \equiv \mu_s(T^L) + \ln P_\infty(T^L) \tag{4.58}$$

In order to express the chemical potential of the liquid phase in a more tractable format one can substitute equation 4.56 into equation 4.32 and then express the liquid pressure in terms of the vapor pressure and the mean radius of curvature through the Laplace equation, 3.15, to find

$$\mu^L = \mu_s(T^L) + \ln P_\infty(T^L) + \nu_\infty^L \left[P^V - P_\infty(T^L) - \frac{2\gamma}{R^{LV}}\right] \tag{4.59}$$

at this point we have all the necessary equations in terms of tractable thermodynamical and molecular properties. Thus, we can proceed to form the final set of equations with vapor phase pressure as the only unknown.

4.5 Final form of evaporation flux using SRT

As seen before, the evaporation rate is given by equation 4.37; however, we may now express the change in entropy in terms of molecular, thermodynamical as well as local equilibrium properties of each respected phase.

Substituting 4.53, 4.55, 4.56, and 4.59 into 4.14, the change in entropy when a liquid molecule emits from the surface can be approximated as [4, 72, 81]

$$\begin{aligned}\frac{\Delta S^{LV}}{k} &= \left[\frac{\nu^L}{T^L}\left(P^V - P_\infty - \frac{2\gamma}{R_c^{LV}}\right)\right] - \left[\ln\left(\frac{T^L}{T^V}\right)^4 \frac{P(T^V)}{P(T^L)}\frac{q_\omega(T^L)}{q_\omega(T^V)}\right] \\ &\quad + \left(\frac{1}{T^V} - \frac{1}{T^L}\right)\left[4T^V + \sum_{i=1}^{i_\circ}\left(\frac{\Theta_{vib}(i)}{2} + \frac{\Theta_{vib}(i)\exp\left(\frac{-\Theta_{vib}(i)}{T^V}\right)}{1-\exp\left(\frac{-\Theta_{vib}(i)}{T^V}\right)}\right)\right]\end{aligned} \tag{4.60}$$

Putting the equation above in 4.37 we obtain the final form of approximated evaporation flux required for our studies.

$$\begin{aligned}J &= 2\mathbf{K}_{eq}\sinh\left[\frac{\nu^L}{T^L}\left(P^V - P_\infty - \frac{2\gamma}{R_c^{LV}}\right)\right] - \left[\ln\left(\frac{T^L}{T^V}\right)^4 \frac{P(T^V)}{P(T^L)}\frac{q_\omega(T^L)}{q_\omega(T^V)}\right] \\ &\quad + \left(\frac{1}{T^V} - \frac{1}{T^L}\right)\left[4T^V + \sum_{i=1}^{i_\circ}\left(\frac{\Theta_{vib}(i)}{2} + \frac{\Theta_{vib}(i)\exp\left(\frac{-\Theta_{vib}(i)}{T^V}\right)}{1-\exp\left(\frac{-\Theta_{vib}(i)}{T^V}\right)}\right)\right]\end{aligned} \tag{4.61}$$

4.6 Numerical calculation of evaporation flux

In chapter 3 we discussed the method used to estimate the shape of the meniscus. Having the required geometrical information to estimate the surface area of the meniscus (equation 3.45) one can also calculate the total evaporation rate by integrating J (after putting 4.60 in 4.37) over the surface area of the meniscus by the following relation [3, 88]

$$J = 2\pi (R_c^{LV})^2 \int_0^{\phi_m} \left[2\mathbf{K}_{eq} \sinh\left(\frac{\Delta S^{LV}}{k}\right) \right] \frac{\bar{x}(\phi_c)}{\vartheta(\phi_c)}\, d\phi \tag{4.62}$$

It should be noted that the only unknown in the equation above is the vapor phase pressure at the interface (i.e. P_I^V). Performing the above steps require some tedious algebra as well as numerical integration and root-finding methods, but with the help of a package such as Matlab this is not too difficult to perform. The flowchart given in Fig. 4.2 depicts the method implemented to predict the vapor phase pressure based on SRT.

4.7 Concluding remarks

In this chapter we have briefly introduced SRT and its applications in predicting nonequilibrium processes. In addition, the expression for the evaporation flux was re-derived (i.e. 4.37). As mentioned earlier, the general expression obtained could not be applied directly, thus, statistical thermodynamic approximations were implemented to substitute for the vapor phase. Finally, the expression

for net evaporation flux was given (i.e. 4.61). This relation can be inverted to implement a numerical method for predicting the vapor phase pressure for a given value of evaporation flux using numerical methods. It should be noted that in the case of liquids such as water, this expression is independent of fitting parameters. Predictions produced using this method are in good agreement with experimental results, and can be useful in the development of evaporation inside capillaries, particularly when the working fluid is water. There are a number of variables that go into this module, most of which can almost readily be determined experimentally or be obtained from tabulated values. However, there are certain variables that would require direct experimental measurements (i.e. interfacial temperature) or the use of molecular dynamic computation and simulation methods (i.e. internal vibration frequencies), that are not known for a wide range of liquids (other than water). This lack of information is rather disheartening, and could hamper the predictions using this method for a number of reasons. First, as pointed out in chapter 2, there is a lack of experimental data for interfacial temperature measurements in case of a receding meniscus at distal parts of the capillary. Second, the internal vibration frequencies of liquids with complex molecular structures are not available. However, despite this lack of knowledge, there is enough known about the basic aspects of an evaporating meniscus in a steady state circumstance that would attenuate the elusiveness of the aforementioned lack of data.

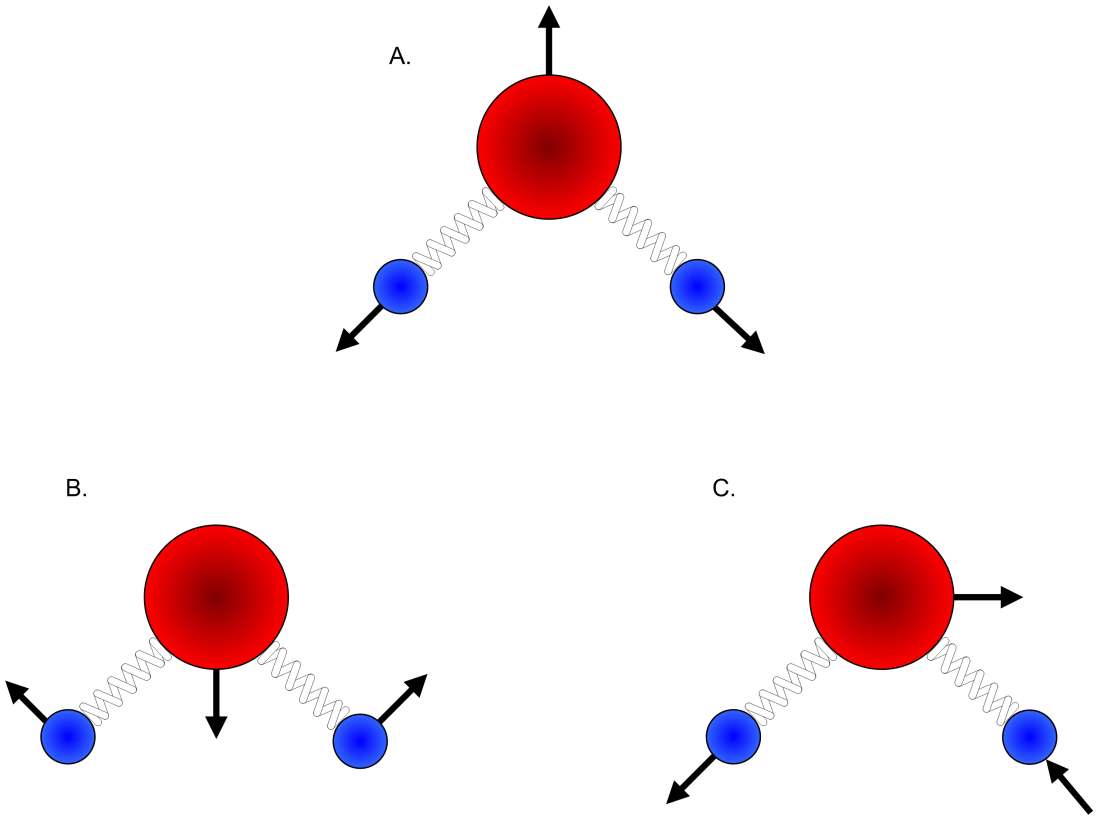

Figure 4.1: Vibrational energy modes for water molecule. A. Symmetric stretch, $\omega_1 = 3657\, cm^{-1}$. B. Asymmetric stretch, $\omega_2 = 3756\, cm^{-1}$. C. Bend $\omega_3 = 1595\, cm^{-1}$.

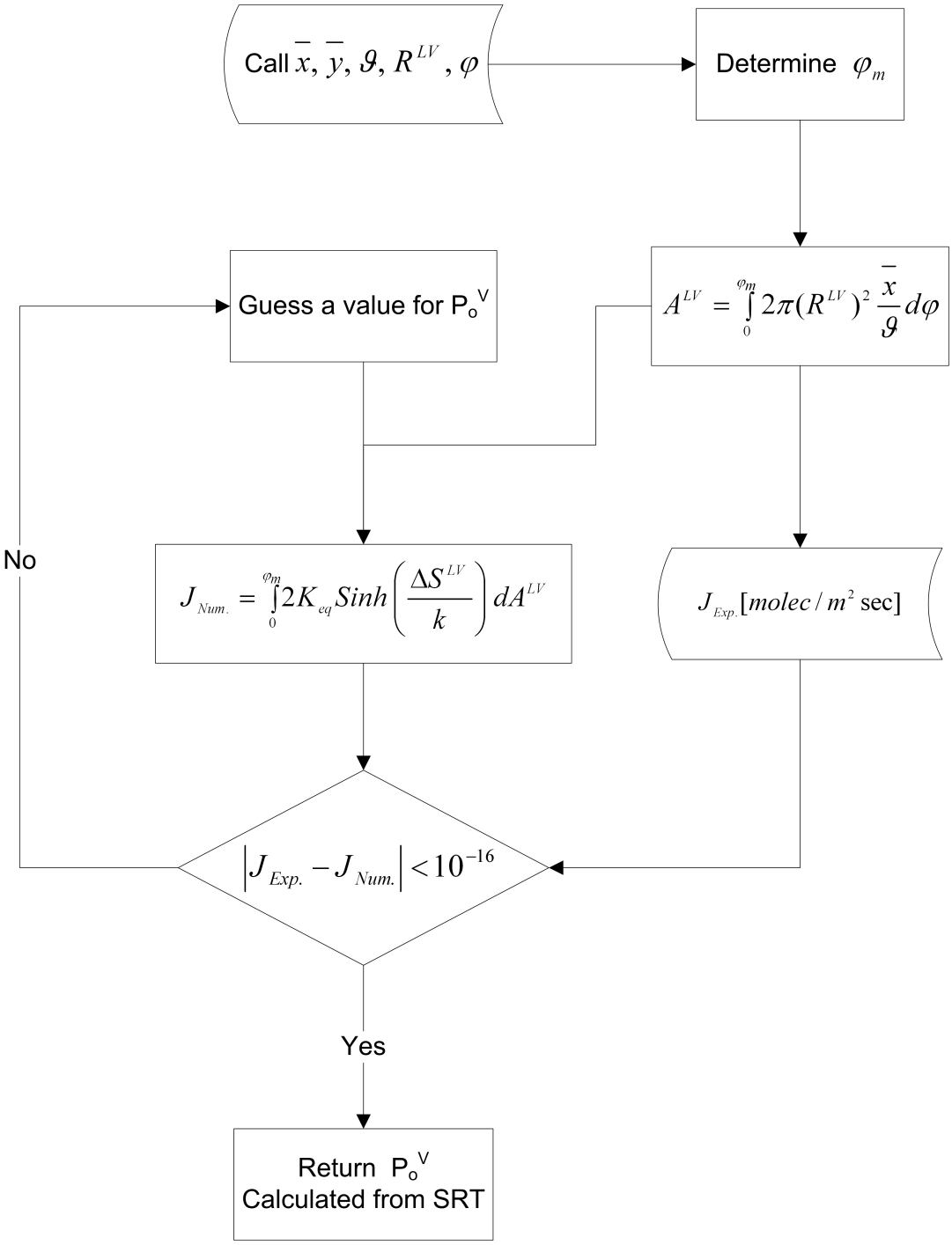

Figure 4.2: General procedure for determining the vapor phase pressure based on SRT.

Chapter 5

Experimental setup and procedure

5.1 Introduction

This chapter will describe the experimental setup in detail, along with the diagnostic equipment and procedures used to collect the pertinent data. The goal of this experiment is to establish a very well defined situation involving the evaporation of liquids that are relatively close to equilibrium and then monitor the evaporation rates as the system approaches equilibrium. In order to create a close to equilibrium situation, the gravitational field is used to establish liquid - vapor interfaces at slightly different pressures (on the order of a just few Pascals difference) and then observe the evaporation rate while the system maintains constant temperature and volume. The physical experimental setup that achieves this goal involves glass cannisters, each containing four glass capillaries, all of which must be clean and free of contaminants. To initiate the experiment the chosen, highly pure, liquid is added to a base reservoir of the evacuated cannister-capillary system and to various heights in all the capillaries. This initial condition is not at equilibrium and liquid from the capillaries slowly evaporates and there is a net transport of mass to the liquid reservoir at the

cannister base. By measuring the change in liquid height in the capillaries the net rate of evaporation can be estimated accurately as the system approaches equilibrium. In the following chapter, the collected data will be presented and compared to theory.

5.2 Experimental Setup

5.2.1 The canisters

Two canisters were used to study the effect of pressure on the rate of evaporation (see Fig. 5.1-5.2). These containers varied in geometrical dimensions that are given in table 5.1 (note that these are the values that were used in all calculations). Each canister consists of 4 capillaries that are closed at the bottom and open from the top, and one capillary which is open at both ends. The tubes were cut from a long glass tube to insure the heterogeneity and inner diameter of the tubes are the same. The capillaries were adhered to a saucer. The saucer was mounted on a stem (a glass rod) and placed at the center of a large diameter cylindrical glass tube. The reason behind having two canisters with various saucer-wall gap is to dictate the radius of the curvature of the bulk liquid meniscus formed in between and hence the bulk liquid pressure.

5.2.2 Canisters' lid

The lid (see Fig. 5.3) for each container consists of four glass tubes with outer diameter of 9.5 $[mm]$. This design enabled us to attach the thermocouples, pressure transducer, filling liquid, and vacuum lines to the lid via Ultra Torr unions (Swagelok®). A groove was etched on the rim of both the canister and

lid for placement of an O-ring to create a Hermetic seal.

5.2.3 The canisters' base

The base of each canister consists of two Aluminum disks connected via 4 metal rods. The canister would sit on the upper disk and a third disk would be used as a flange to press the lid down. Rubber gaskets were laid between the metal and glass parts to prevent them from chipping. To ensure each canister could withhold an air tight seal, the nuts on the flange would then be tightened thoroughly. It should be pointed out that once disconnected from the vacuum pump, the canisters had to withhold the vacuum during the course of each experiment. A schematic view of the canister is given in Fig. 5.4.

5.2.4 Temperature chamber

An environment chamber (Cincinati Sub-Zero Products, Inc., Model No. ZPH-32-1.5-H/AC) was used to keep the pre-set temperature constant (± 0.5 °C at steady state condition after stabilization) during the period of each experiment.

5.3 Preparation and Materials

5.3.1 Water distiller and filtering units

The water used for the experiment and rinsing purposes was distilled using a Fistreem II 2S Glass Still (Barnstead®). The distilled water was then collected in a 9 liter container (Nalgene®) that was attached to the filtering and deionizing unit, E-pure (Barnstead®, Model No. D4641) with four Module Type I Cartridge Kit. The water was used once, the resistivity meter measured its

specific resistance to be 18 $M\Omega\, cm$.

5.3.2 Cleaning procedure

Before each experiment all the glassware went through a rigorous cleaning procedure with a minimum of 24 hours between each step. This would allow the cleaning agents to remove unwanted contamination. The method used was similar to that prescribed by G.B. Jackson [93], and the cleaning solutions were used in the following consecutive order, Acetone (Fisher®), soap solution (Alconox®) and Chromic-Sulfuric acid (Fisher®). After each step the respected cleaning solution was drained and the parts were thoroughly rinsed with distilled deionized water until no residue of the cleaning agent was observed. To check if the glassware were clean, they were filled with distilled-deionized water and then emptied. Once the water formed an evenly distributed smooth sheet, with no signs of visible droplets, it was judged to be clean.

All other miscellaneous non-glass parts (e.g. O-rings, valves, filling tube, unions, etc.) were soaked in soap solution and meticulously rinsed before being used.

5.3.3 Other liquids

Octane (Aldrich®, 99+%, CAS Number 111-65-9) and Methylcyclohexane (Aldrich®, 99+%, CAS Number 108-87-2) were utilized as working liquids in these experiments. It should be pointed out that the aforementioned liquids were used as received and were not otherwise purified.

5.3.4 Degasification

The degasifying container was a 2.5 liter bottle (Corning, Germany). A pyrex tube with an outer diameter of 6.35 [mm] was attached to the side of the bottle to allow a path through which liquid could flow out. A 6.35 [mm] Bellows-Sealed valve (Swagelok®) was then connected to tube. After filling the bottle with the designated liquid, the neck of the bottle was closed with a 38.1 [mm] rubber stopper. A 12.7 [mm] stainless steel tube was inserted through the rubber stopper and sealed using epoxy (Varian Vacuum Tech.). A pressure gauge (WIKA Inc.) and a 12.7 [mm] valve (Bellows-Sealed) were connected to the stainless steel tube through a T-junction connector (Ultra Torr®). The 12.7 [mm] valve was then connected to a cold-trap connected to a vacuum pump (Welch®, Model No. 1402N) through a length of Teflon® tubing. The cold trap was filled with dry-ice and kept that way during the course of degasification procedure to prevent any damages caused by the liquid vapor to the pump. To enhance the degasification process the bottle was placed on a hotplate and stirrer (Jenway®) and a Teflon coated dumbbell shaped stirring bar was used to whirl the liquid. The apparatus is schematically shown in Fig. 5.5.

5.4 Diagnostic tools

5.4.1 Instrument calibration

The thermocouples (Copper-Constantan, type K, 0.4 mm) were formed into a U-shape and the ends were welded together. For each canister a set of 4 thermocouples were calibrated to monitor the temperature variations, in addition 2 other sets were used to record the temperature control in the environment chamber. The calibration was performed using a temperature bath

(NESLAB Inst.), and two mercury filled thermometers (Barnestead®, $\pm 0.01^0$ C). The thermocouples were connected to an ice point cell (Omega, Inc.) and at each temperature step (from $0°C - 70°C$) the voltage was recorded through a data acquisition/switch unit (Agilent 34970A, Agilent Technologies®) for a minimum of 40 seconds. When temperature differences occur an output voltage proportional to that temperature is generated. The corresponding voltages were recorded and then converted to temperature values employing a calibration curve.

Two pressure transducers (PX209, Omega, Inc.) were used in this study to monitor the vapor pressure inside the canisters. An aluminum vacuum chamber was designed for this calibration purpose (see Fig. 5.6). The pressure transducer, a U-shaped absolute manometer, the vacuum pump, and a Bellows-Sealed swagelock® valve were connected to the chamber. Starting from the minimum available vacuum (≈ 0 [KPa]) to atmospheric pressure, the mercury height was read with a cathetometer for a minimum of 32 points. The accuracy of the mercury column height reading was ± 0.001[mm]. At each step the output voltage of the pressure transducer was recorded and was later used for calibration purposes. Fig. 5.7 schematically depicts the calibration setup. It should be pointed out that the purpose of the pressure transducers were to detect any possible leakage in the canisters, and thus the recorded data was not used in any of our calculations.

5.4.2 Cameras and Switch-Box

In order to take pictures of the targets of interest (e.g. meniscus heights and the bulk liquid) in the containers, two cameras (Canon Rebel XTi and Canon Rebel

XT) were mounted on a custom built camera mount. The mount allowed for the height and location of each camera to be adjusted independently. Using a level, it was ensured that each camera was positioned perpendicular to the object's plane. The cameras had the view of the objects inside the environment chamber through the view window with a curtain thrown over them to prevent ambient light exposure. The light source was placed inside the temperature chamber behind the objects with a light diffuser in between. A switch box was designed and built to have the cameras take pictures every 90 minutes, turning the light source off after each image was taken. A Plexiglass® panel was placed in front of the containers to prevent direct forced air flow coming in contact with the the containers. This factor impeded the unwanted accumulation of condensed vapor on the front side of the canister which would ultimately obscure the view of the capillaries.

5.5 Experimental procedure

Before each experiment was performed, all parts were cleaned as described previously. Using a syringe, the capillaries were filled with the liquid to the designated heights. A filling tube was then inserted inside the lid. The purpose of this tube was to direct the liquid flow to the container wall which would then facilitate the filling procedure. After closing the lid, the instruments (i.e. thermocouples, pressure transducer, as well as filling and vacuum line shut-off valves) were mounted. At this stage, the container was put under vacuum by gradually opening the control valve while monitoring the pressure changes via a Labview program. This gradual, but progressive, adjustment of pressure lowers the chances of nucleation of the liquid inside the capillaries. It should be

noted that a sudden drop in pressure may cause nucleation in the distal parts of a capillary tube which, as a result, would push the water out. The container of the degassed liquid was then connected to the filling valve mounted on the canister lid through a Teflon® tube. The connecting line was vacuumed prior to opening the shut-off valve which would allow the the liquid to flow to the canister. Lastly, the canister was filled to the saucer rim before the filling valve on the lid was closed. The same procedure was repeated to prepare the second canister as well. Once the canisters were filled, they would be put inside the temperature environment with a previously set temperature. Finally, the cameras were adjusted and a curtain was thrown over them to isolate changes in the ambient light intensity. At this stage the only source of illumination was the light sources inside the environment chamber which were controlled by the timer box and turned on a few seconds before each image was taken and then turned off again after the picture was taken. It should be noted that once the experiment started it was not interrupted by any means and was continued as such until the course of each test was over. A schematic of the experimental set up as a whole is depicted in Fig. 5.8.

5.6 Digital Image Processing

In order to obtain the location of the liquid meniscus inside capillaries the images taken of each canister was required to be digitally processed. In this section we shall give a brief but concise description of the methods used to extract this information. The images are stored as two-dimensional arrays (i.e, matrices), in which each element of the matrix corresponds to a single pixel in the display image. For instance, an image composed of X rows and Y columns of differ-

ent colored dots would be stored in an X by Y matrix. The color images are in the RGB format, which requires a three dimensional array (X by Y by 3), where the first, second and third plane represent the red, green, and blue pixel intensities respectively. The color of each pixel is determined by combination of those color intensities stored in each color plane at the pixel's location. In order to perform image arithmetic (i.e. the implementation of arithmetic operations, such as addition and subtraction on an image), it was convenient to convert the color images to gray scale. This operation would merge the three dimensional array of data into a one dimensional matrix. The resulting array is an X by Y by 1 where X and Y represent the location of the pixel with the color intensity of the pixel ranging from 0 to 2222 where 0 is black and 2222 is white [94–96].

The pictures taken from the canisters were then digitally analyzed to determine the location of the meniscus in the capillaries (that are closed at one end), bulk liquid and the capillary which is open at both ends. Due to the uniqueness of each task, there were several computer manuscripts created to capture the location of desired meniscus or bulk liquid. The identified location was then saved and passed on for further calculations. The geometry of the capillaries, local illumination and surrounding regions can profoundly affect some processes (e.g. capillary edge detection), so that such techniques are limited to the specific geometry where they were developed for. Indeed, the methods used were not unique to this problem but found to give the best result for the given conditions. Because of the sensitivity of the analysis to the uniform back illumination for the objects, it was necessary to include a light diffuser to avoid any uneven distribution of light in the background which could significantly alter the image processing procedure.

5.6.1 Capillary edge detection

An issue, which was required to be taken into consideration, was that the capillary tubes were not straight. Intuitively, the middle point of each capillary needed to be located and included when searching for the location of the meniscus. The other issue that could complicate the analysis of each image was the vibration associated with the environment chamber. As mentioned above these two conditions made it necessary for a robust code which could locate the middle point of a capillary at each single image before proceeding to the next step.

To overcome this problem, the initial location of the meniscus and the capillary edge was manually read and given to the code. However, these values were only treated as boundary conditions, and did not affect the final result. Given the boundary conditions the code would consider a square region of (100 x 100) pixels above the initial location of the meniscus. A typical raw color image of a chosen section of a capillary is shown in Fig. 5.9.A, which is then converted to a black and white image Fig. 5.9.B.

A vertical Canny filter would then act on this region to facilitate the capillary edge detection procedure, as shown in Fig. 5.9.C. At this stage the resulting binary image may not be clear or noise free, thus, the regions containing less than 50 pixels were chosen to be eliminated from the frame, as shown in Fig. 5.9.D. The detected vertical lines represent the outlines of the capillary edge were found to be weak and discontinuous, thus additional post processing of data was still required. As a result, the lines in the image were dilated and elongated and the resultant was then multiplied by the original image. This

multiplication resulted in the elimination of the regions other than the detected edges to go to zero and the color intensity of the lines (which were binary before this stage) to become equal to the original image, see Fig. 5.9.E. In addition, this would eliminate other possible noise that could alter the edge detection procedure. The color intensity along every row of the final image was then stored and used to calculate the total average. The first and last maximum of the averaged data (in X direction) suggested the location of the left and right edges of the capillary respectively. The middle point of the capillary for every image could then be readily calculated and returned to the main body of the code for future calculations. This might seem like a small task, however, it created considerable control over complications as the correct detection of the meniscus level depends on the location of the middle of the capillary tube.

5.6.2 Location of the meniscus and bulk liquid

At this point it was required to find the location of the meniscus and the bulk liquid. Before getting down to details, it must be realized that the geometry and material (i.e. glass) of the containers, as well as vapor condensation on some parts resulted in optical characteristics that could impose intricacies during digital image processing. As a result, and in order to detect the meniscus location throughout the length of the capillaries, several computer programs were written to compensate for these factors. However, a reasonable understanding could be achieved by considering the explanation given below.

Initially, a number of images that were taken within the few hours of the experiments were added together and their total average was calculated. At each step the absolute difference of original image from the average was cal-

culated. This method would enhance the detection of meniscus location as it ultimately subdued the dominant color intensity of the non moving elements (e.g. capillaries) in an image. In order to find the location of the meniscus the average color intensity along the middle index of the capillary $\pm$ 2 pixels was vertically calculated. The minimum color intensity (i.e. the darkest pixel) along the averaged vector corresponds to an index in that vector which represents the vertical position of the meniscus in the form of pixel location, see Fig. 5.10. Intuitively, the proposed method would only be accountable for the cases that were undergoing evaporation, and thus the meniscus level was changing over time. However, in the case of open capillary, and the bulk liquid the location of the target was detected regardless of it previous position.

Unfortunately, it was not possible to adequately control for the regions in which the meniscus level was obscured behind the rim of the inner saucer or the bulk liquid (i.e. regional identification of the meniscus level is not achievable in any precise way, due to lack of clarity in those regions, and or concealment of the meniscus behind the bulk liquid). In these regions the location of the target was incomprehensible and is not available. Although this is a simplification of what actually occurs in the process of finding the location of the meniscus and the bulk liquid, it provides a good understanding of what actually takes place in the computer code for those who may not be familiar with digital image processing methods. A part of the algorithm used for meniscus position detection is given in Fig. 5.11.

5.6.3 Determining pixel calibration factor

A profile projector (Mitutoyo® PH-3500) was employed to measure the length of two length-scales 160.108±0.001 and 160.198± 0.001 [mm]. The length-scales were then used to determine the pixel-to-length ratio factor in the images. Since the camera and the object did not move during each test, the calculated conversion factor remained constant for the entire image set. Each length scale was mounted on an L shaped bracket outside the container such that it would be in the same plane as the capillaries. A level was used to ensure that the scale was perpendicular to the field of view (i.e. parallel with the capillaries).

5.7 Summary

In this chapter the details of the experimental apparatus and diagnostic equipment have been presented, as well as the procedures associated with cleaning the equipment, instrument calibration, initiating the experiment and collecting and quantifying the images to measure the rate of evaporation. In the next chapter, the results from the use of this setup will be presented.

Container1	L_b [mm]	51.70±0.01
	R_b [mm]	4.8895±0.0001
	capillary's inner diameter [mm]	1.10±0.01
Container2	L_b [mm]	49.69±0.01
	R_b [mm]	2.54±0.0001
	capillary's inner diameter [mm]	1.10±0.01

Table 5.1: Geometrical dimensions of containers 1 and 2. L_b and R_b are depicted in Fig. 3.4.

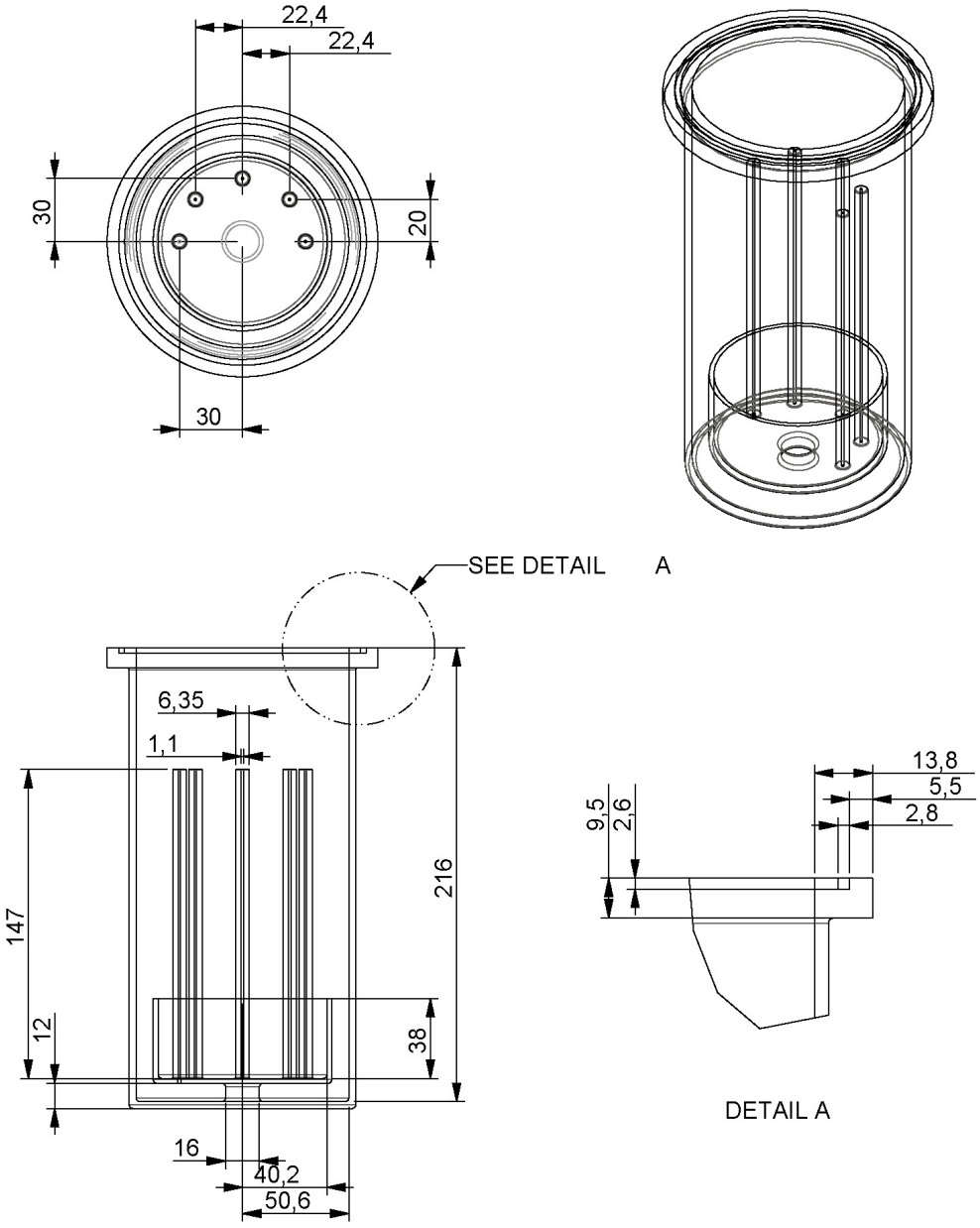

Figure 5.1: Technical drawing of container one. All dimensions are in millimeters. The tube thickness is approximately 3.3 [mm].

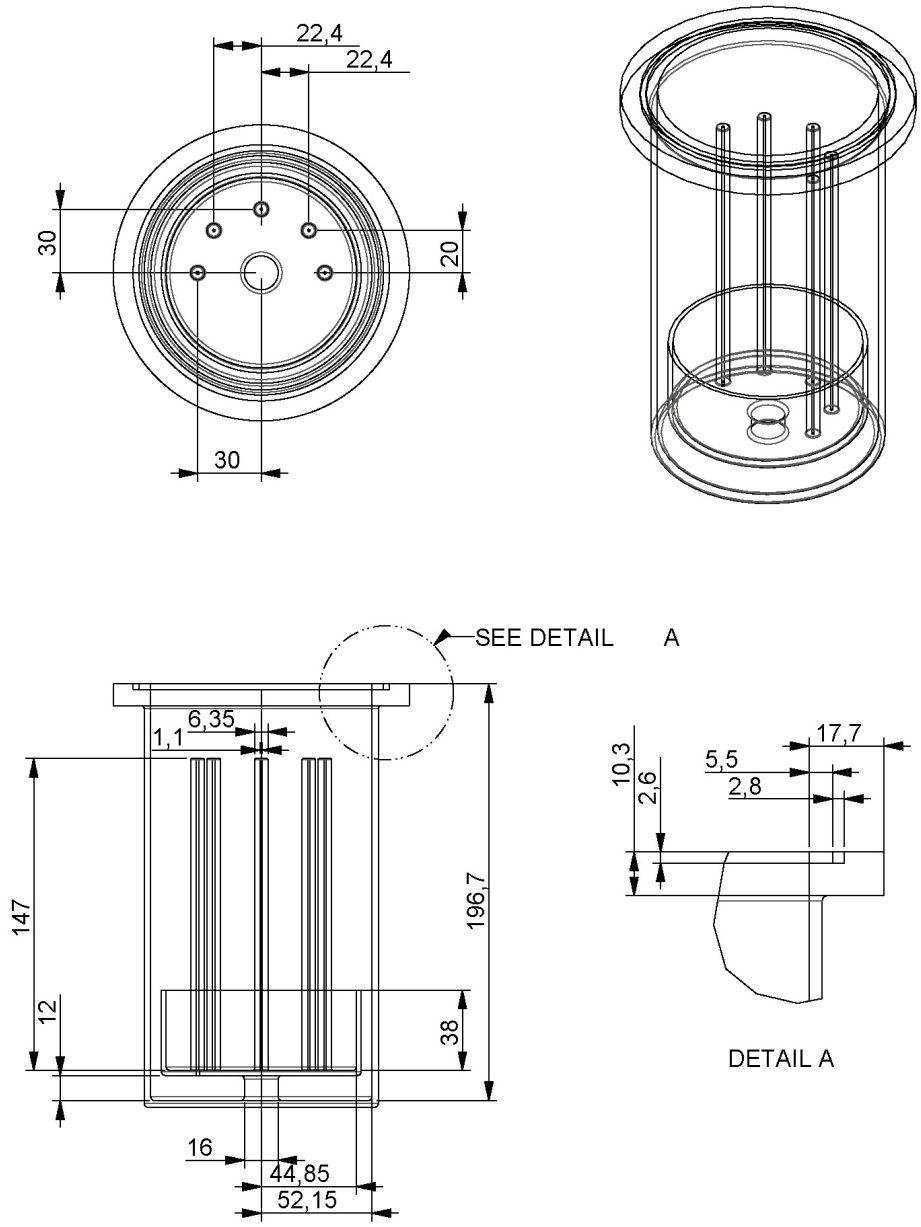

Figure 5.2: Technical drawing of container two. All dimensions are in millimeters. The tube thickness is approximately 3.1 [mm].

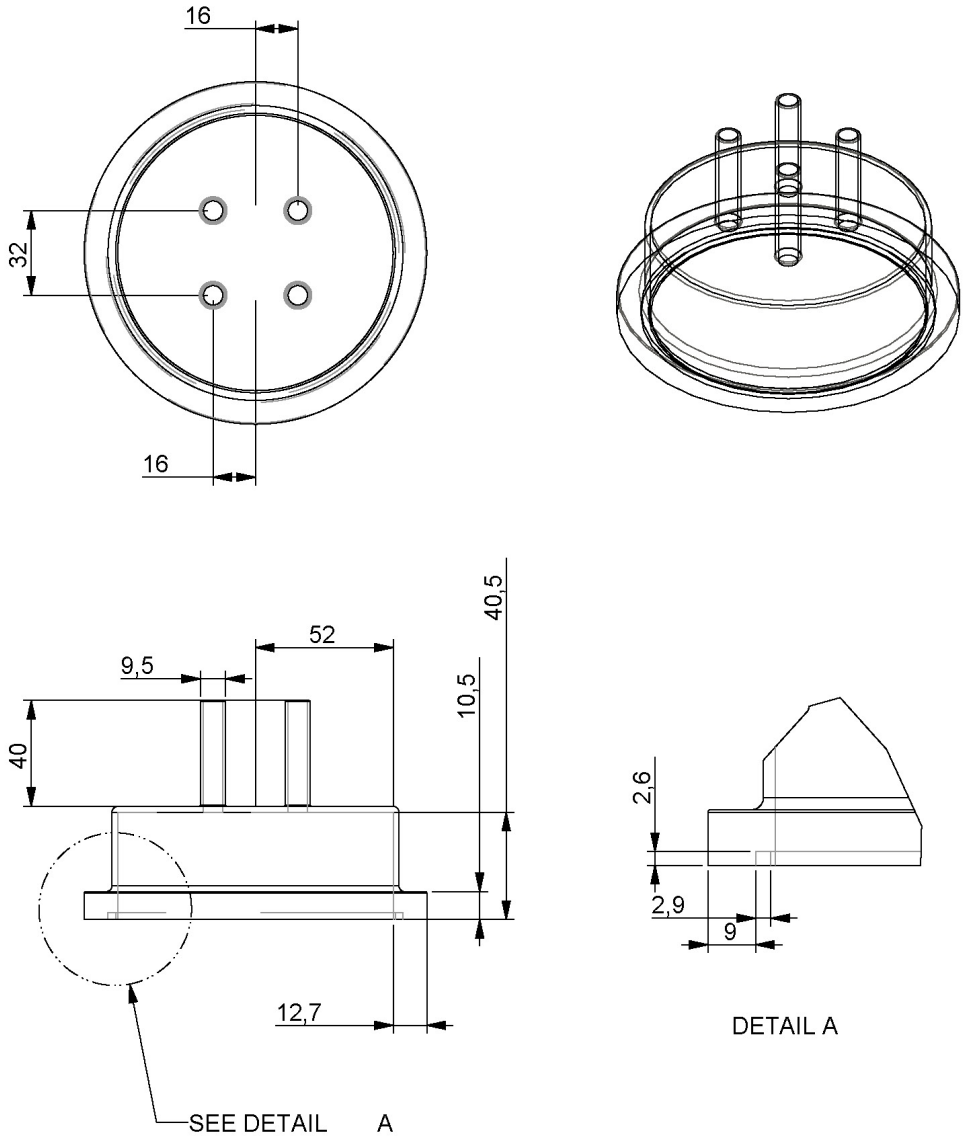

Figure 5.3: Technical drawing of the container's lid. All dimensions are in millimeters.

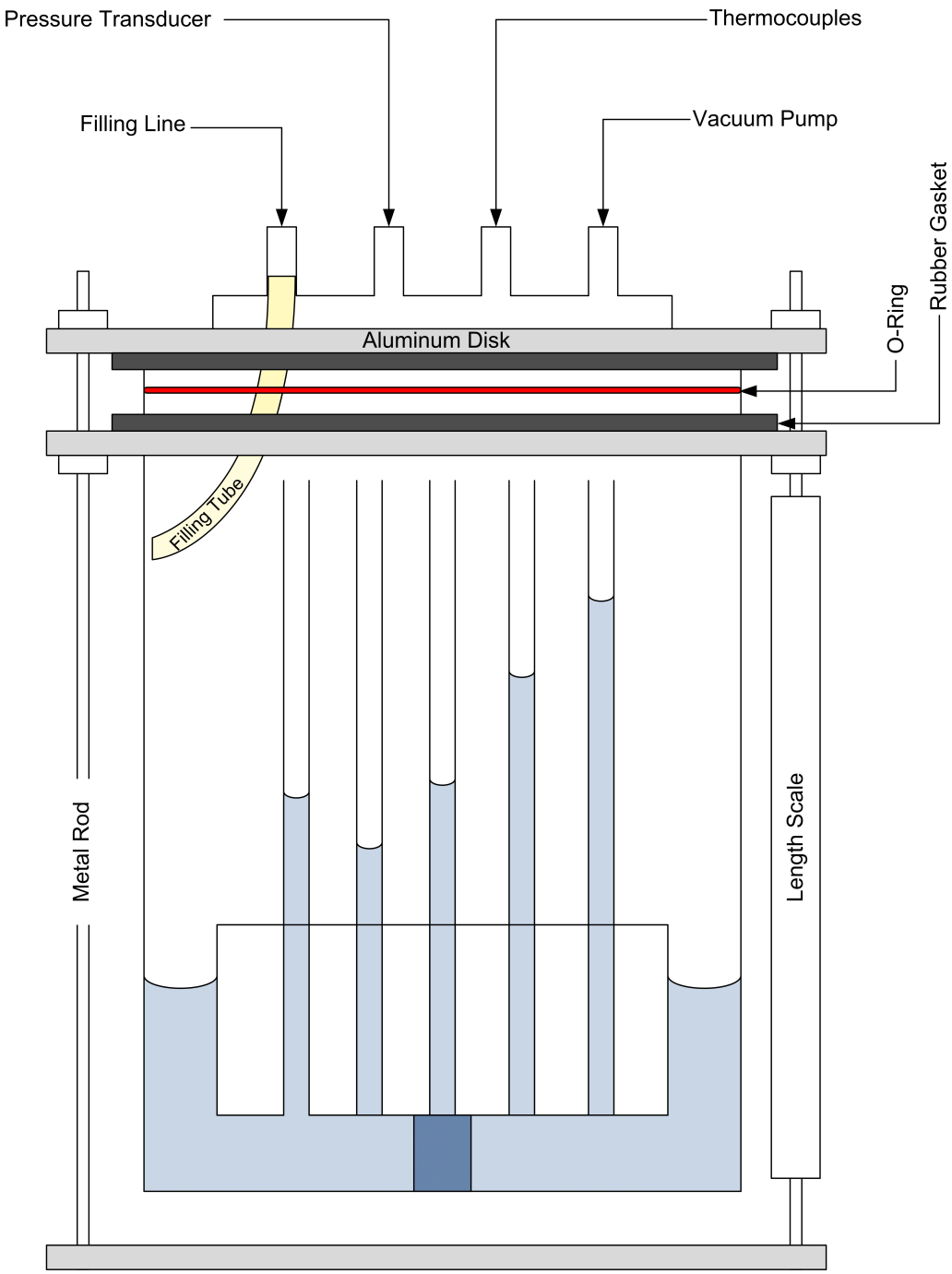

Figure 5.4: Schematic view of the glass container.

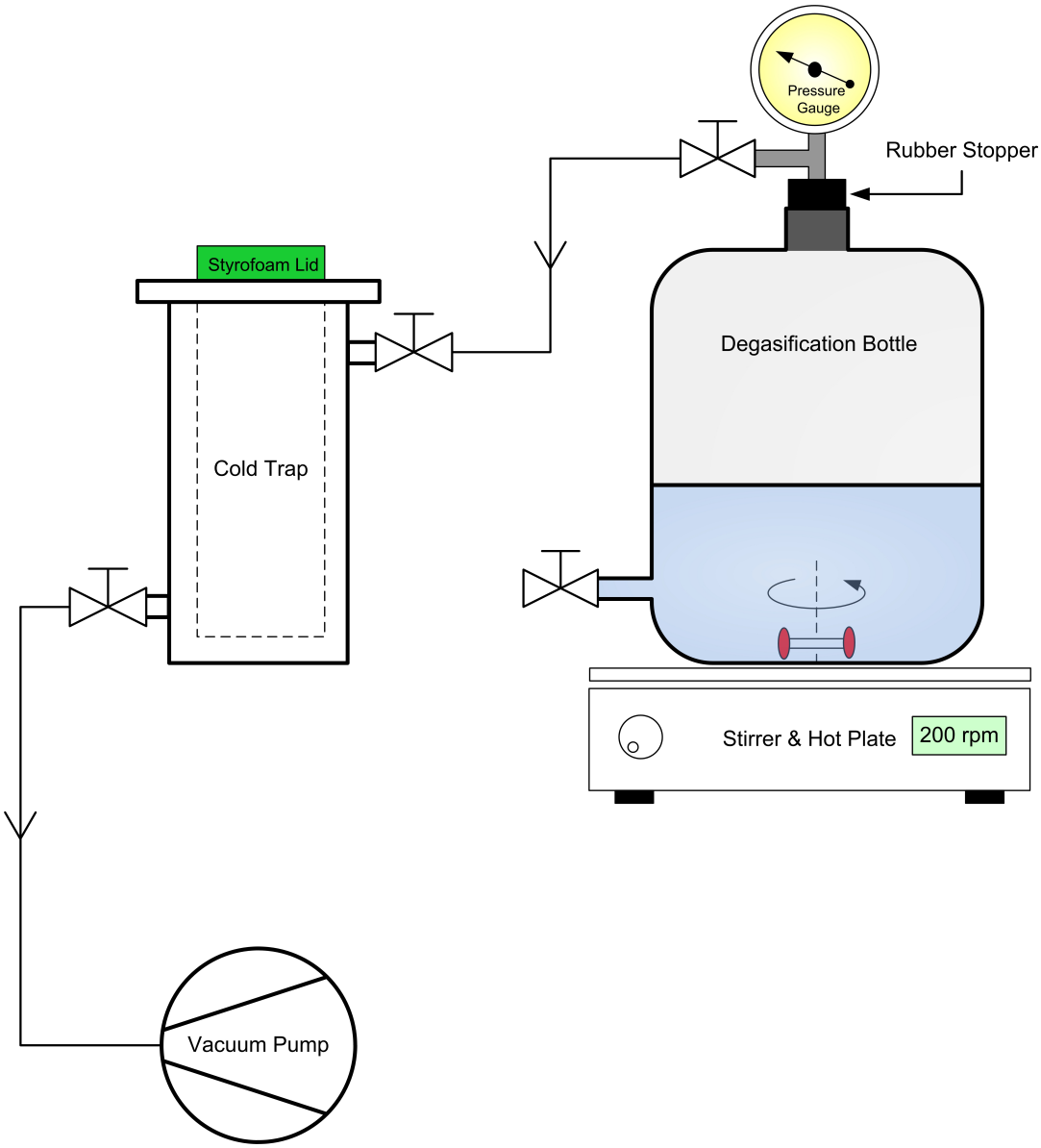

Figure 5.5: Schematic view of the degasification equipment.

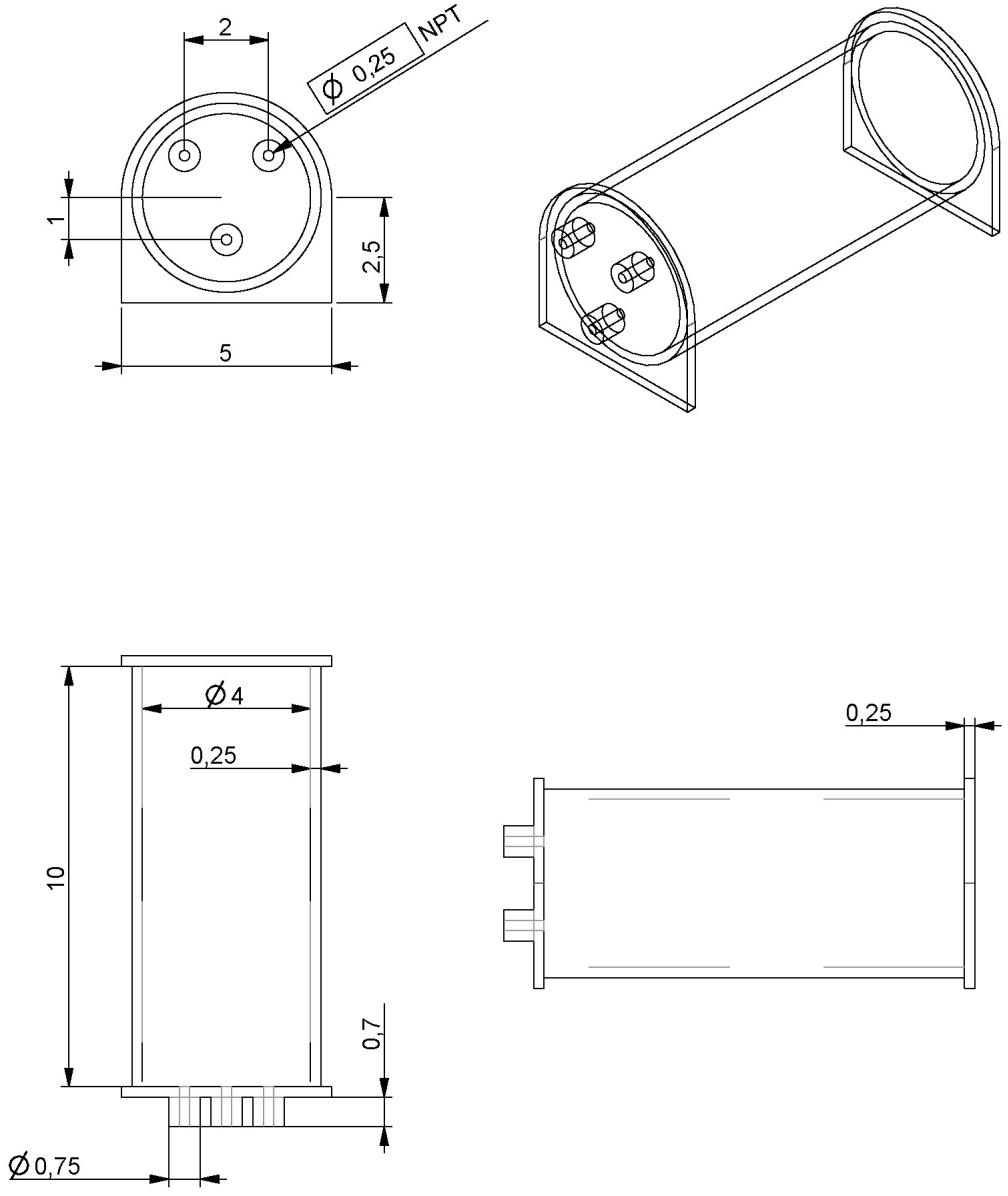

Figure 5.6: Technical drawing of the vacuum chamber used for pressure transducer calibration. All dimensions are in inches. Material Aluminum.

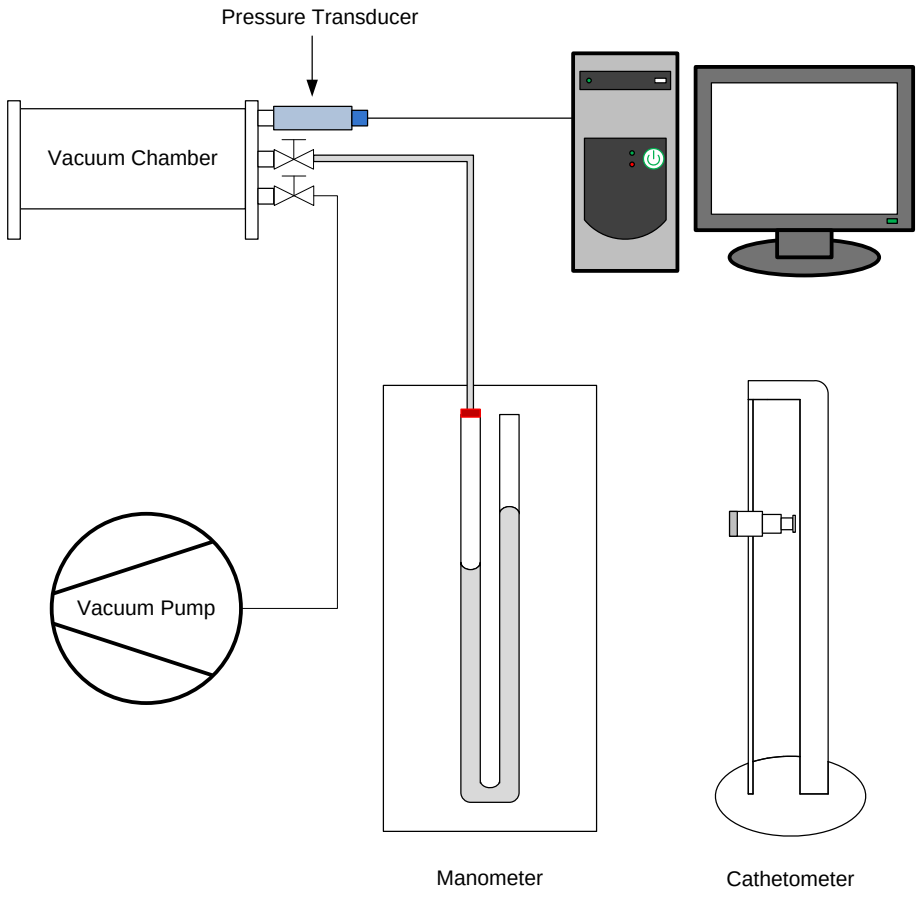

Figure 5.7: Schematic view of the pressure transducer calibration procedure.

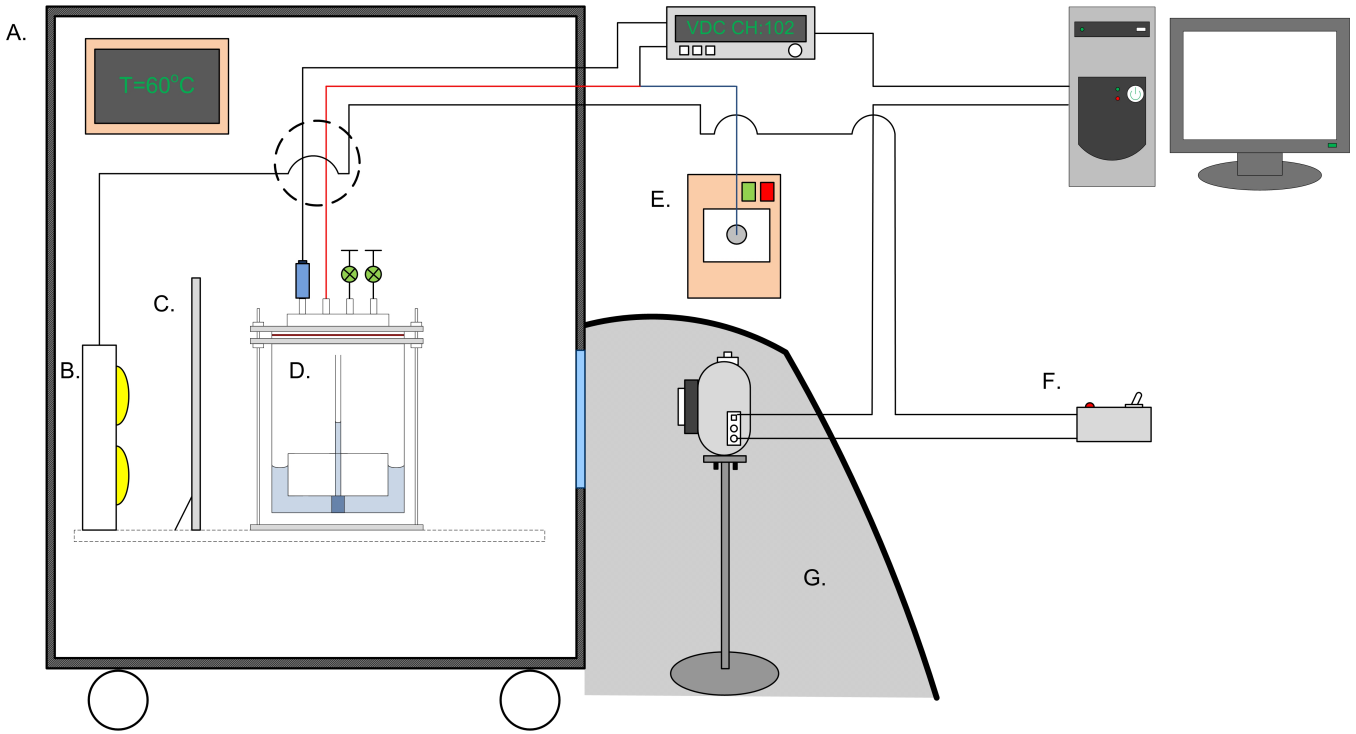

Figure 5.8: Schematic view of the experimental setup: A. Environment Chamber, B. Light Source, C. Light Diffuser, D. Canister, E. Zero Point Cell, F. Timer, and G. Dark Room.

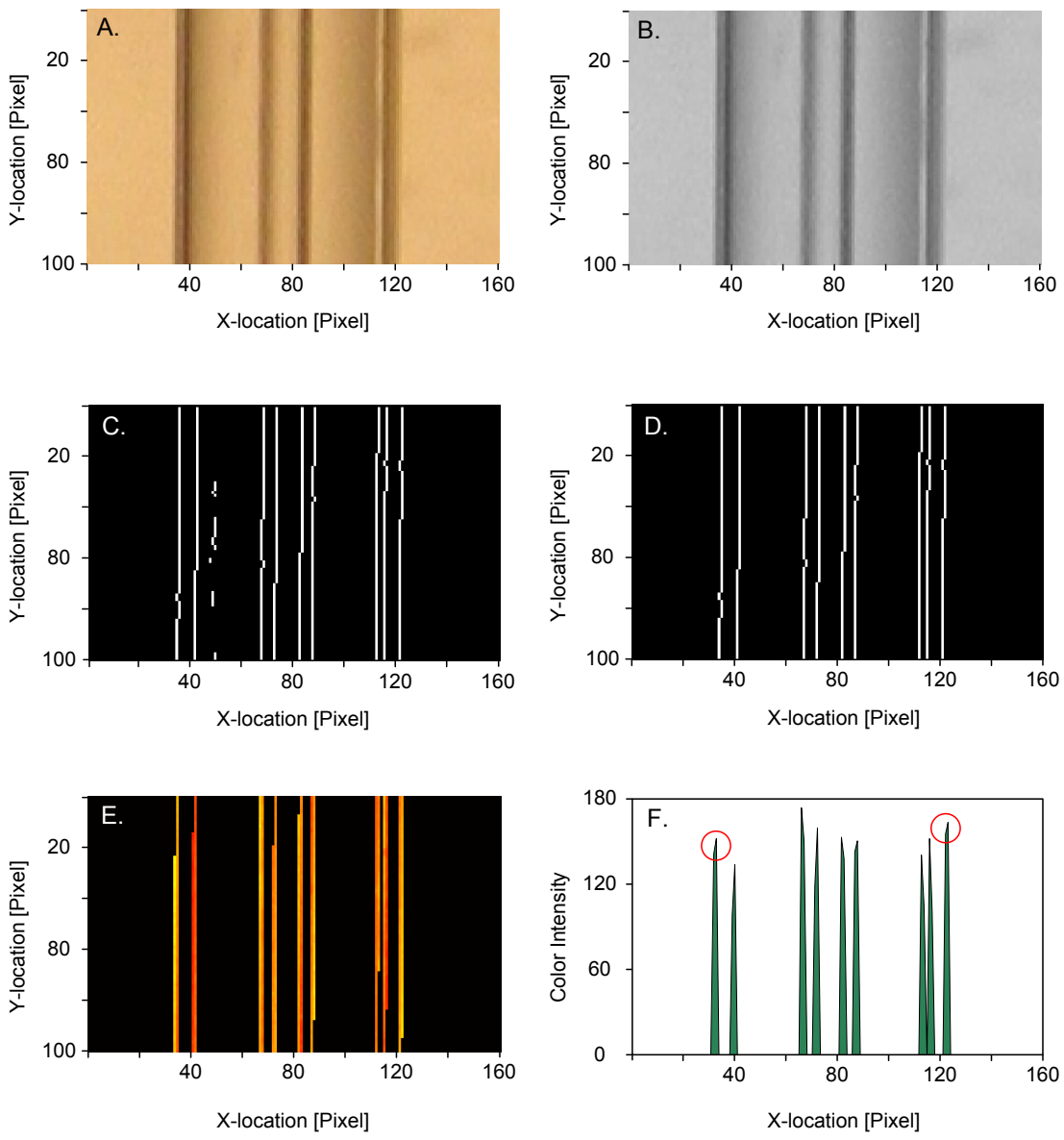

Figure 5.9: Image processing method used for capillary edge detection: A. The original RGB image (here, 100×160 pixel), B. RGB image converted to black and white, C. Image B. after applying a vertical Canny filter, D. Image B. after eliminating regions containing less that 50 connected pixels, E. Image D. after elongating the weak lines and multiplying the resultant with image A., F. The average of rows plotted as a function of color intensity. The first and last peak correspond to the capillary edge.

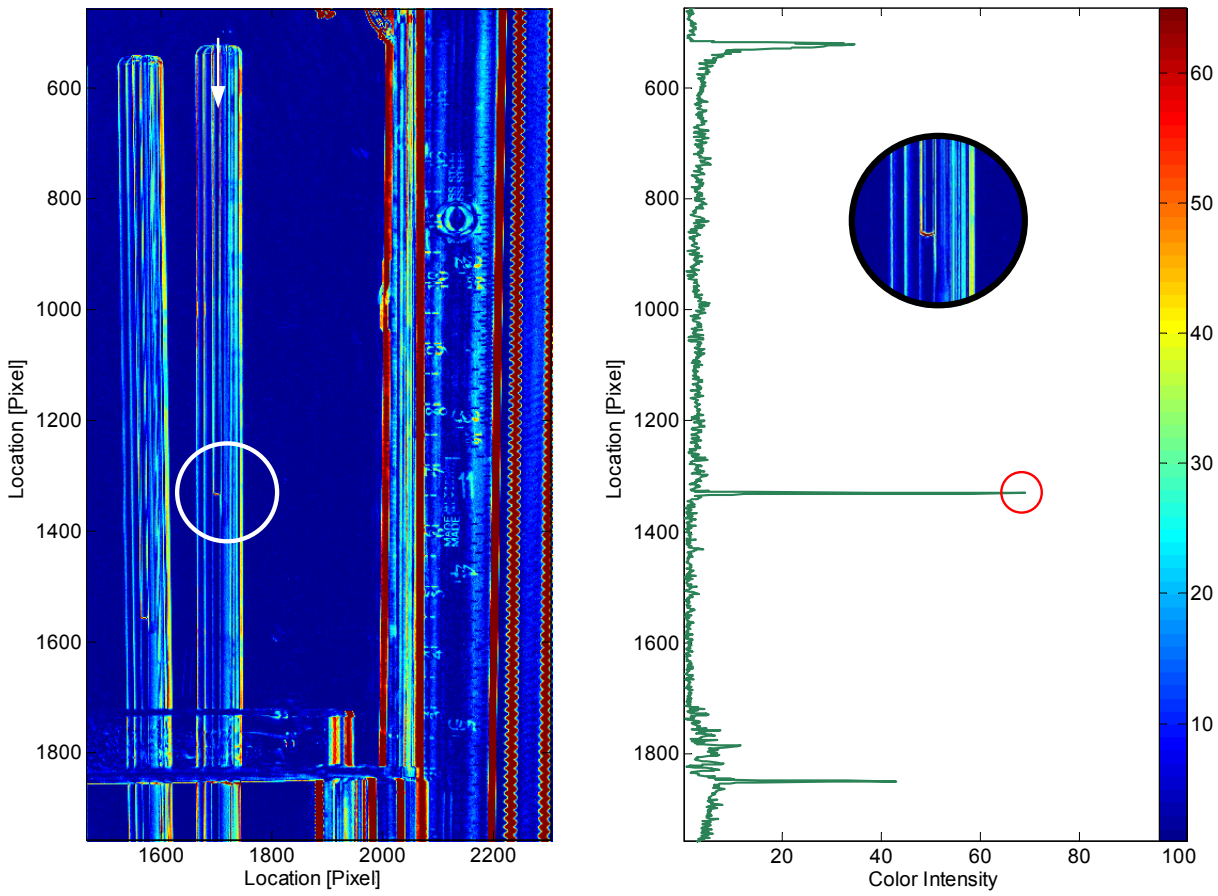

Figure 5.10: Left: The absolute value of the original image subtracted from the average of a number of initial images. Right: Color intensity plotted along the middle point of the capillary in Y direction. The peak value represent the location of the meniscus in pixel.

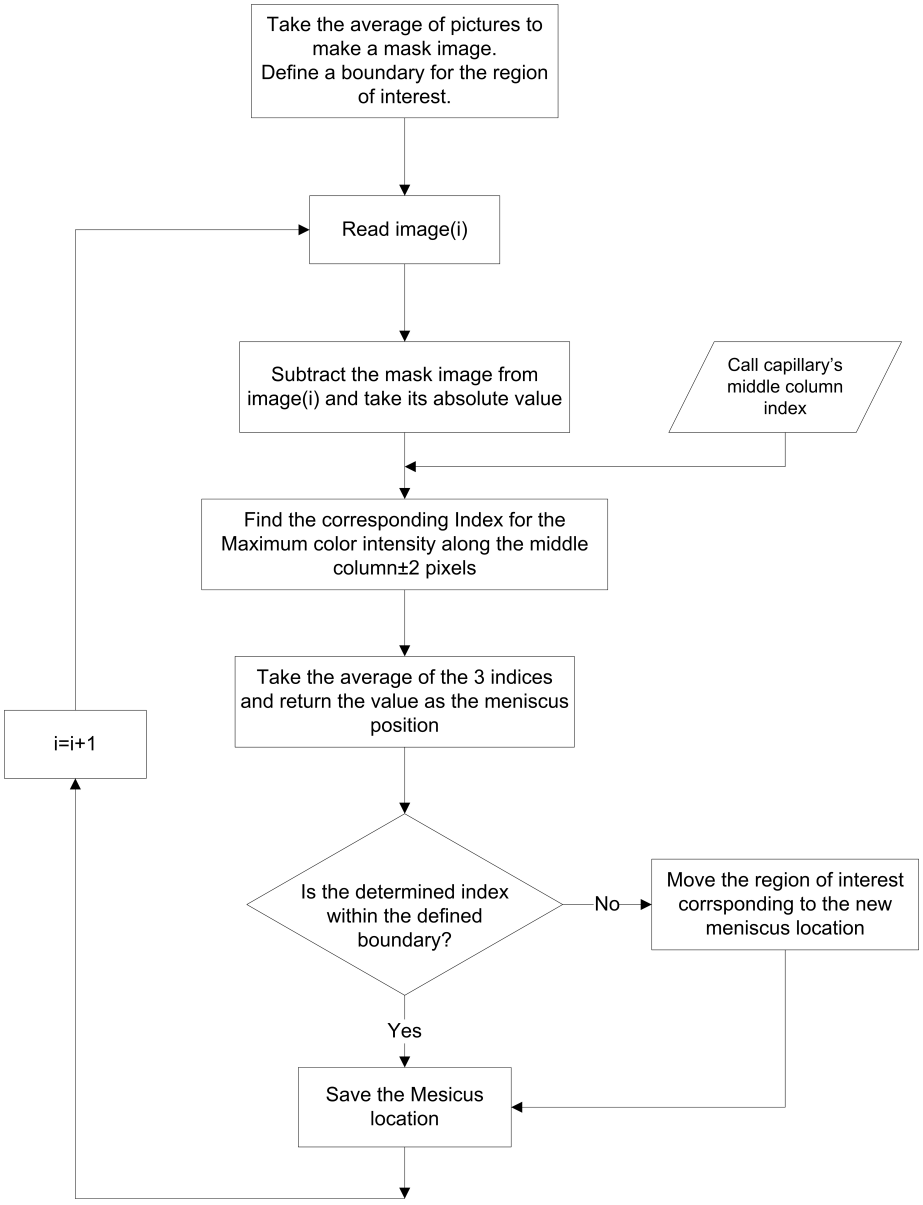

Figure 5.11: A part of the of the algorithm used for meniscus position detection.

Chapter 6

Results and discussion

6.1 Introduction

In the previous chapter we discussed the experimental setup. The objective was to monitor the change in the height of the liquids inside capillaries for various liquids under the prescribed constant temperature during the course of each experiment. For this purpose, two containers with various geometrical dimensions were built. As mentioned in the previous chapter, the variation in saucer-wall gap dictates the radius of curvature of the bulk liquid meniscus formed in between and hence the bulk liquid pressure at the apex of the formed bulk interface. This structure would then enable us to scrutinize the effect of pressure on the rate of evaporation of liquids from the capillaries in an isolated, close to equilibrium condition. It was hypothesized that the canister with lower bulk liquid phase pressure (i.e. bigger saucer-wall gap), under similar conditions, should exhibit a higher rate of evaporation from the liquids inside the capillaries than that of a smaller gap (i.e. canister 2). One of the principal objectives for conducting these systematic experimental procedures was to further expand the much needed lack of data sets for evaporation of liquids in such controlled environments. By combining observations from experiments with the

provided SRT model, it is possible to achieve a reasonably good understanding of how different parameters (e.g. variations in temperature) could affect the rate of evaporation of liquids in near equilibrium conditions.

6.2 Experimental results

A review of the experiments performed is provided in Table 6.1. The outcome of the tests will be presented as this chapter unfolds.

Container	Temperature $°C$	Working Liquid
1	30	Water
2	30	Water
1	40	Water
1	51	Water, Octane, Methylcyclohexane
2	51	Water, Octane, Methylcyclohexane
2	62	Water

Table 6.1: Summary of the preformed experiments.

First, focusing on the results obtained from the case study of container 2, T=62$°C$ and working liquid of distilled, deionized water is presented in Fig. 6.1.

As can be seen, Fig. 6.1 depicts the location of the meniscuses inside capillaries 1 through 4, as well as the open capillary, from the bulk liquid phase as a function of time. It should be pointed out that the gaps between the data points is due to the inability to detect the location of the meniscus at a particular location. That could be due to obscured visibility as a result of excessive condensation on the canister wall, capillary wall, concealment of the meniscus behind the bulk

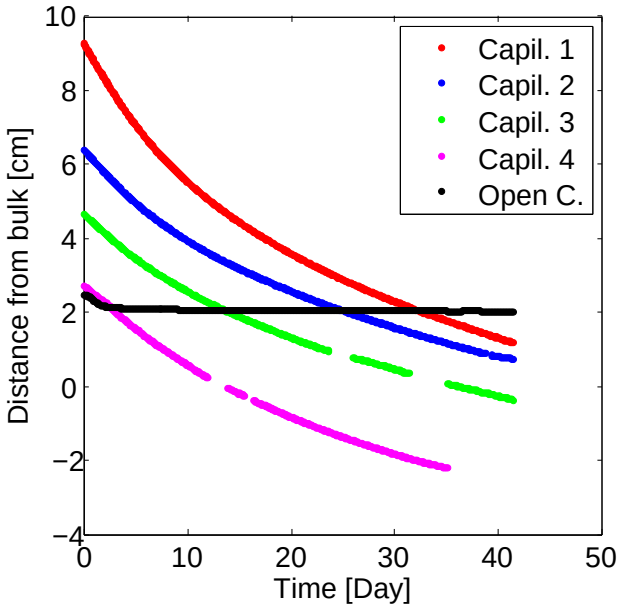

Figure 6.1: Measured interface position for container 2 at $62°C$.

liquid and/or the saucer rim. In these regions the location of the meniscus was inevitably undetectable and is not available.

Several results can be deduced from this data set. First, it can be seen that the meniscuses heights are monotonically decreasing as a function of time. This suggests that the evaporation is the dominant physical phenomena and that if in fact condensation does occur it is negligible. Second, the data set exhibit a higher slope within the first few days of the experiment which ultimately subsides as time progresses. This trend could be interpreted as an indication that the system is reaching its corresponding equilibrium configuration, and thus the evaporation/condensation is suppressed. At last, a capillary with a higher initial meniscus location (with respect to the bulk liquid phase) experiences more evaporation in comparison with those of a lower initial height.

By revisiting the concepts introduced in preceding chapters, and the notion

that the rate of change in evaporation of liquids (in close to equilibrium conditions) is believed to be predominantly affected by the vapor phase pressure above the meniscus, we have an expectation that the evaporation rates at the same height from the bulk liquid should be the same. That being said, the presented SRT model does not include nonequilibrium aspects of the vapor flux away from an evaporating meniscus to the ambient environment.

In order to examine this hypothesis, the experimental data set shown in Fig. 6.1 was re-worked to present the evaporation flux in terms of $\left[\frac{molecule}{m^2.sec}\right]$ vs. the location of the meniscus from the bulk liquid phase, see Fig. 6.2.

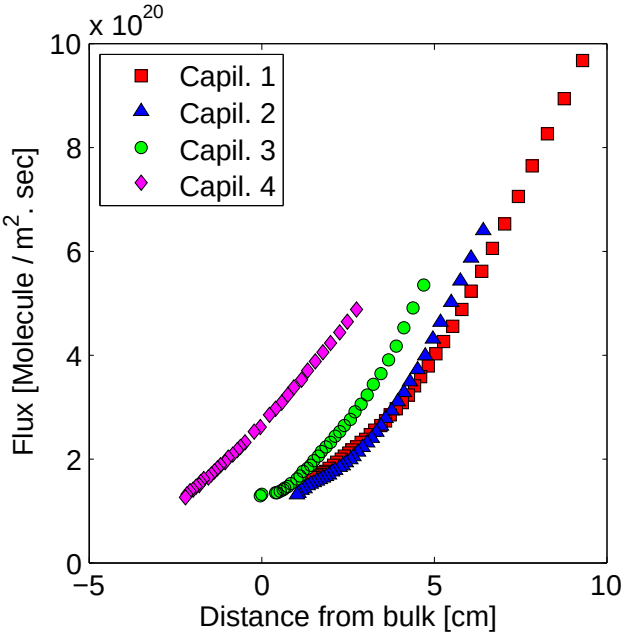

Figure 6.2: Calculated flux vs. interface position for container 2 at $62°C$.

From Fig. 6.2 it is evident that capillaries 1 and 2 exhibit a close evaporation rate at the same location from the bulk liquid. However, this trend is not as closely followed by capillary 3 and in particular capillary 4. Using typical values

for meniscus height, tube diameter, density, time and meniscus surface area, the uncertainty in flux is estimated to be 7%.

In an attempt to further investigate the effects of temperature and geometrical boundary conditions (that determine the pressure within the system) a set of experiment was conducted at $40°C$ using container 1. As mentioned before, container 1 had a larger gap between the saucer and the wall and thus, in comparison with container 2 the bulk meniscus formed is less curved. Since the shape of the bulk liquid meniscus is the determining factor for estimation of the liquid pressure at the apex of the meniscus, in similar conditions, we expect to have a lower liquid pressure (i.e. higher vapor pressure) in the container with a higher bulk liquid curvature (i.e. container 2) than that of with the lower curvature (i.e container 1), see table 6.2. The data set obtained from conducting the test at $40°C$ with distilled, deionized water as the working liquid is depicted in Fig. 6.3.

From Fig. 6.3 it is apparent that the following factors are commonly shared between the previous data set (i.e. container 2 at $62°C$): the monotonic decrease in the hight of the meniscuses, a higher slope within the early days of the experiment which lessens through to the final days of the test, and finally a capillary starting with a higher meniscus location exhibit a higher change in height than that with lower starting points. For the sake of brevity, henceforth the aforemention conditions will be referred to as the Commonly-Shared-Trend (CST). It is worth reminding that the gaps in the data sets are due to incomprehensibility in detecting the meniscus' position.

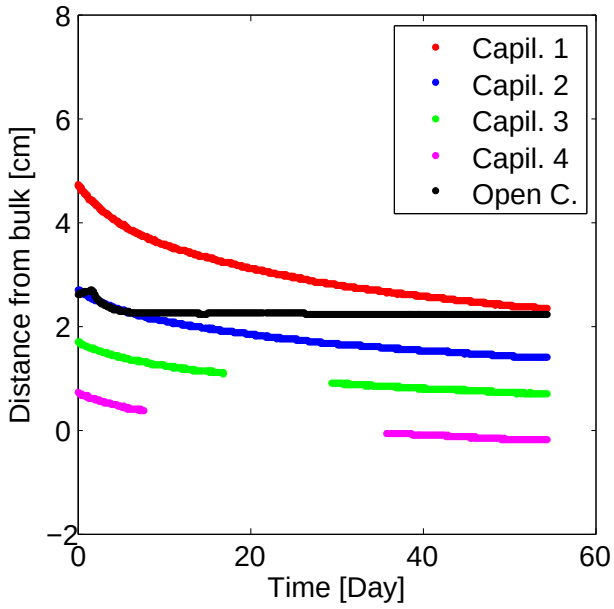

Figure 6.3: Measured interface position for container 1 at $40°C$.

In accordance with an attempt to obtain a better understanding of the role of pressure on the rate of evaporation in liquids, the data set depicted in Fig. 6.3 is reanalyzed to show the evaporation rate as a function of bulk liquid phase pressure and is depicted in Fig. 6.4.

As can be seen from Fig. 6.4, the evaporation rates at the same bulk phase pressure are not equal. This could be interpreted as an indicator of the possibility of other factor(s) beside the vapor phase pressure above the meniscus, that could be equally as important and play a significant role in this phenomena. The highest calculated evaporation rate at these conditions shows a 59% decrease in comparison with the base case study.

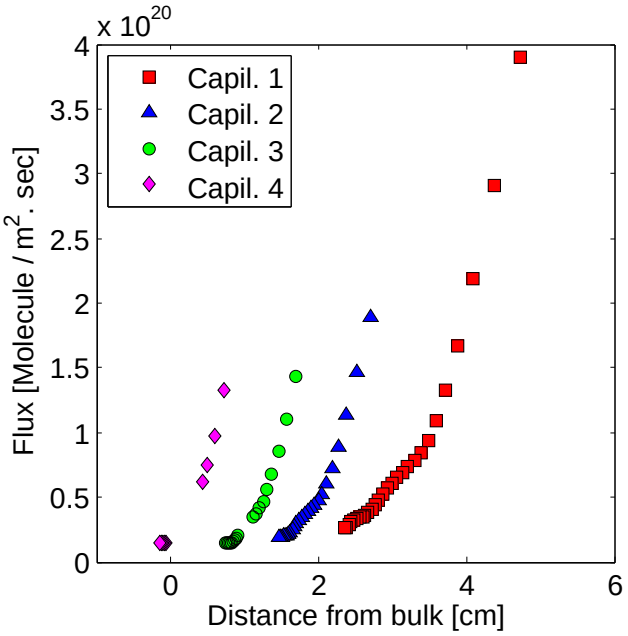

Figure 6.4: Calculated flux vs. interface position for container 1 at $40°C$.

6.2.1 The effect of geometry at the same temperature

By comparing observations from experiments like those presented above, it was evident that more tests were required to achieve a reasonably good understanding of how different parameters affect the evaporation in a controlled environment. To limit the interconnect variability between temperature and pressure, a number of tests were performed at same temperature for both containers. As we will see, the collected information assisted us to illustrate a better picture in understanding this phenomena in any such conditions.

The results obtained for both containers 1 and 2 with the working temperature kept at $51°C$ is shown in Fig. 6.5 and Fig. 6.6 respectively.

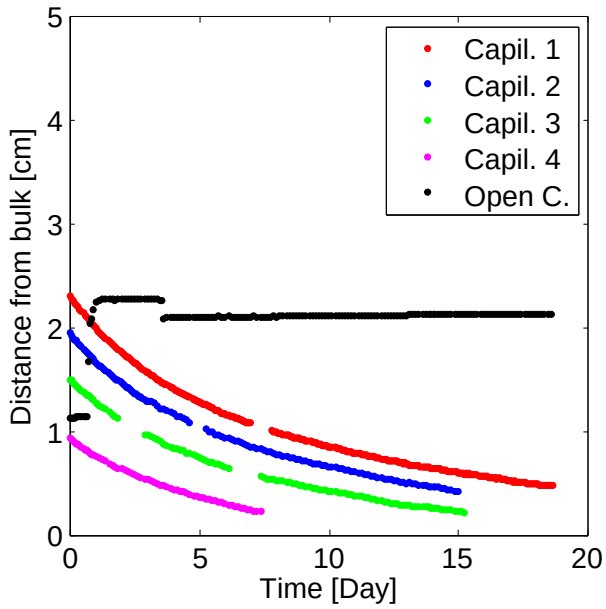

Figure 6.5: Measured interface position for container 1 at $51°C$.

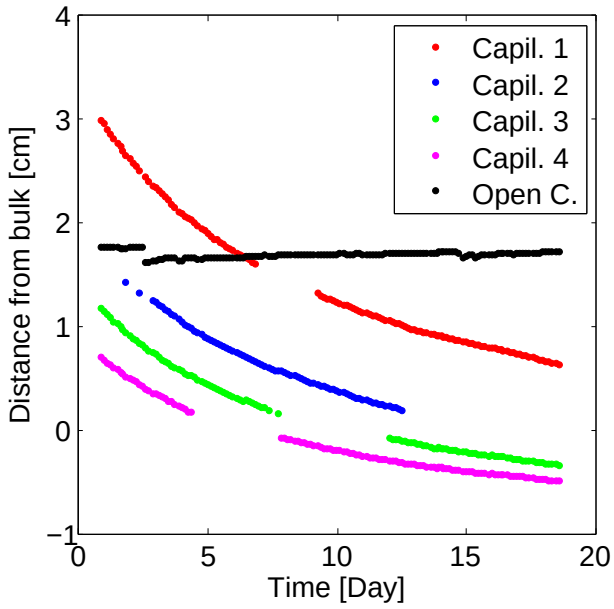

Figure 6.6: Measured interface position for container 2 at $51°C$.

As can be seen from figures 6.5 and 6.6 the CST is evidently repeated in both cases. It is evident that the change in height for the menisci with respect to time is more when the initial location above the bulk was higher. The following factors could influence that trend. First, the higher the level of meniscus above the bulk phase the lower the vapor phase pressure. Second, the meniscus location is closer to the open end of the capillary, thus, the vapor flux away from it has a better chance of diffusing out of the capillary. Intuitively, in cases where the evaporation rate is higher than the diffusion rate away from the interphase, the accumulated vapor above the meniscus could in fact suppress and choke the evaporation.

Figures 6.5 and 6.6 were reworked to express the evaporation flux vs. bulk liquid pressure and are given in Fig. 6.7 and Fig. 6.8. As can be seen the rate of change in evaporation for various capillaries is not necessarily the same at the

same location above the liquid phase bulk. This finding somewhat contradicts the prevalent hypothesis suggested by some authors who perceive the effect of pressure in any such conditions as an ineluctable and sole predominant factor affecting the rate of evaporation in liquids in any such conditions.

In container 1, at approximately 1.1 centimeters above the bulk interface the evaporation rate from capillaries 2 and 3 is 23% and 56% higher than the calculated evaporation flux from capillary 1. This is while in container 2, at approximately 1 cm above the bulk interface capillaries 2 and 3 experience 97% and 154% higher rates of evaporation that than of capillary 1 at the similar location.

In order to have a better understanding, the evaporation flux vs. bulk phase pressure for both containers is shown in in Fig. 6.9.

It was hypothesized that a container with a lower bulk liquid curvature (i.e container 1) should experience a faster rate of liquid evaporation from capillaries (of the same height above the bulk interface) in comparison with the case of a container corresponding to a higher vapor phase pressure (i.e. container 2). Although at approximately 1 centimeter above the bulk phase capillary 1 in container 1 has a higher evaporation than its counterpart in container 2, this trend is just the opposite in case of capillaries 2 through 4.

These findings contradict the authors who have ruled the pressure above an evaporating liquid interface from a capillary tube as the only factor that is inherently and predominantly responsible for controlling the rate of evaporation in similar experimental situations.

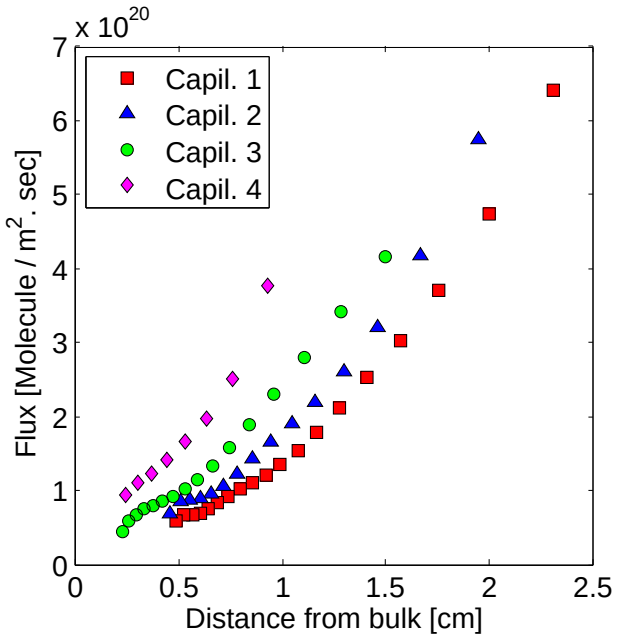

Figure 6.7: Calculated flux vs. interface position for container 1 at $51°C$.

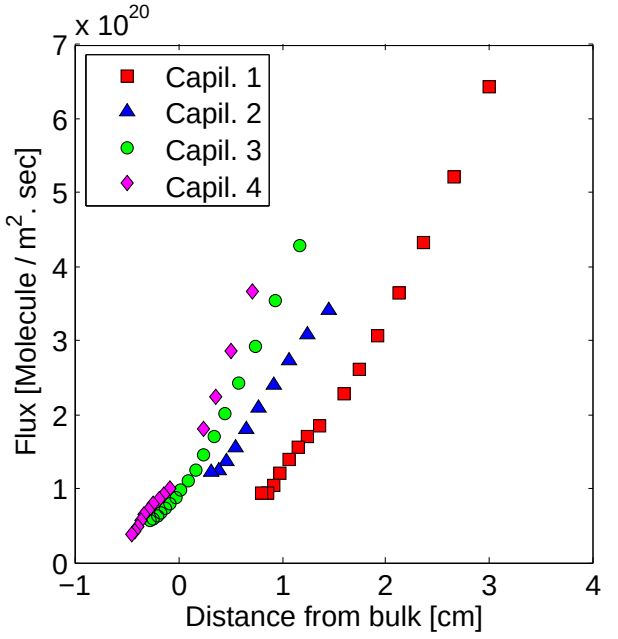

Figure 6.8: Calculated flux vs. interface position for container 2 at $51°C$.

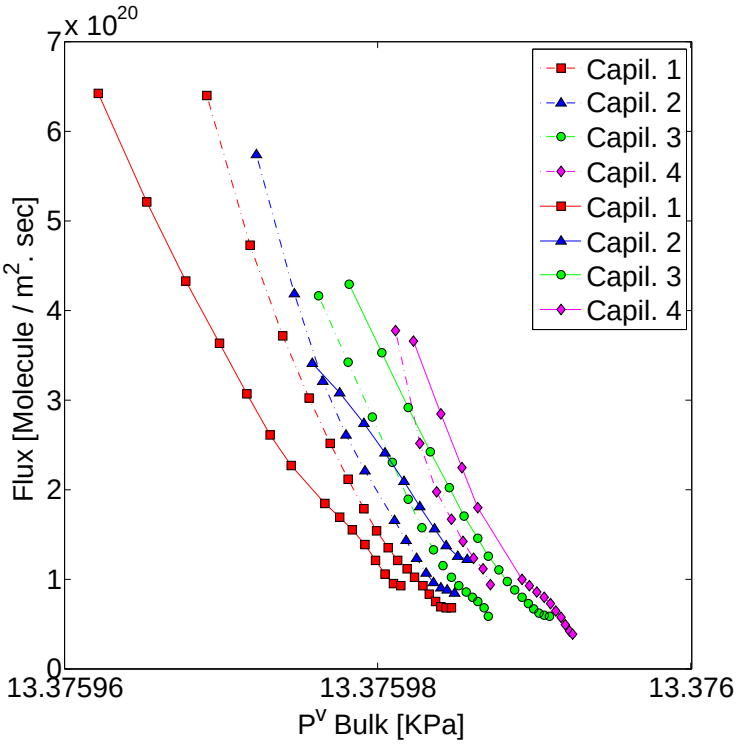

Figure 6.9: Flux as a function of bulk phase vapor pressure for both containers at $51°C$. Dashed lines represent container 1.

Similar tests were preformed for both containers, this time at $30°C$. The data sets obtained for containers 1 and 2 are depicted in Fig. 6.10 and Fig. 6.11 respectively. This time the order in which the capillaries were filled was changed such that capillary 2 would start with a higher position with respect to the other 3 capillaries that are closed at the bottom. This would clarify the possible role of yet another probable interconnective variable, i.e. the homogeneity of the capillary wall, on the rate of evaporation from capillaries.

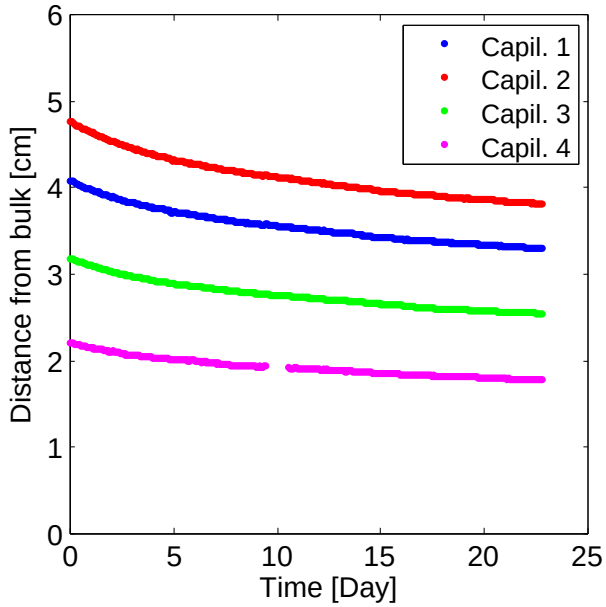

Figure 6.10: Measured interface position for container 1 at $30°C$.

As can be seen in Fig. 6.10 and Fig. 6.11, the CST trend is manifested in both cases. Note that this time the location of the meniscus in capillary 2 in both containers is higher. This change in the order of initial heights in capillaries was imposed to further speculate and rule out the possibility of the effect of glass wall inhomogeneity on the rate of evaporation from the capillaries. Thus, by looking at the results depicted in Fig. 6.10 and Fig. 6.11, it can be deduced

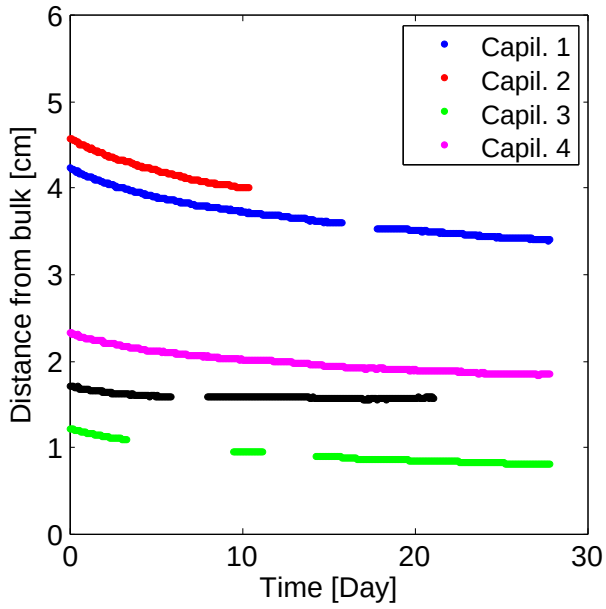

Figure 6.11: Measured interface position for container 2 at $30°C$.

that the initial location of the meniscus with respect to the bulk liquid phase is undoubtedly the determining factor in this case study. This finding confirms the notion that the evaporation from capillaries is affected by the initial height of the meniscus.

The plots showing the flux vs. the bulk liquid phase pressure for containers 1 and 2 are provided in Fig. 6.12 and Fig. 6.13 respectively.

In an attempt to compare the evaporation flux of both containers as a function of the vapor phase pressure they are presented at once in Fig. 6.14.

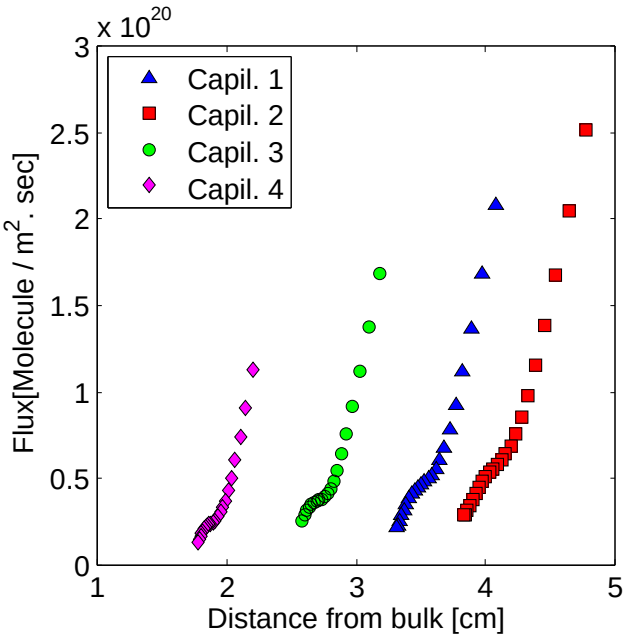

Figure 6.12: Calculated flux vs. interface position for container 1 at $30°C$.

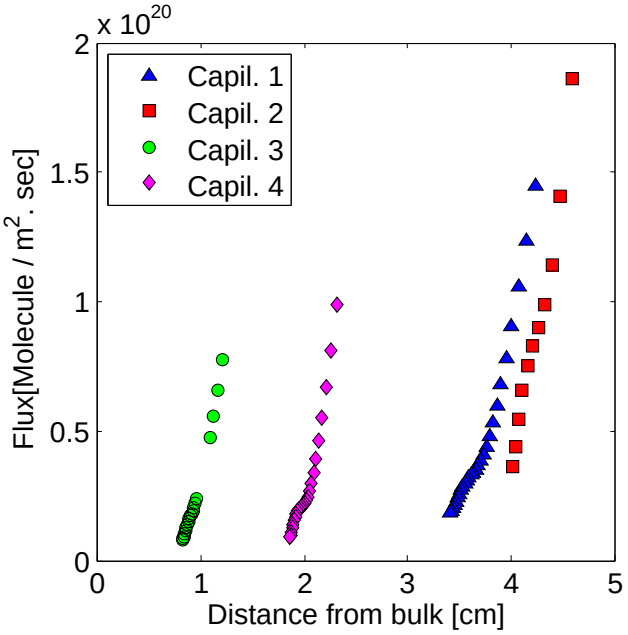

Figure 6.13: Calculated flux vs. interface position for container 2 at $30°C$.

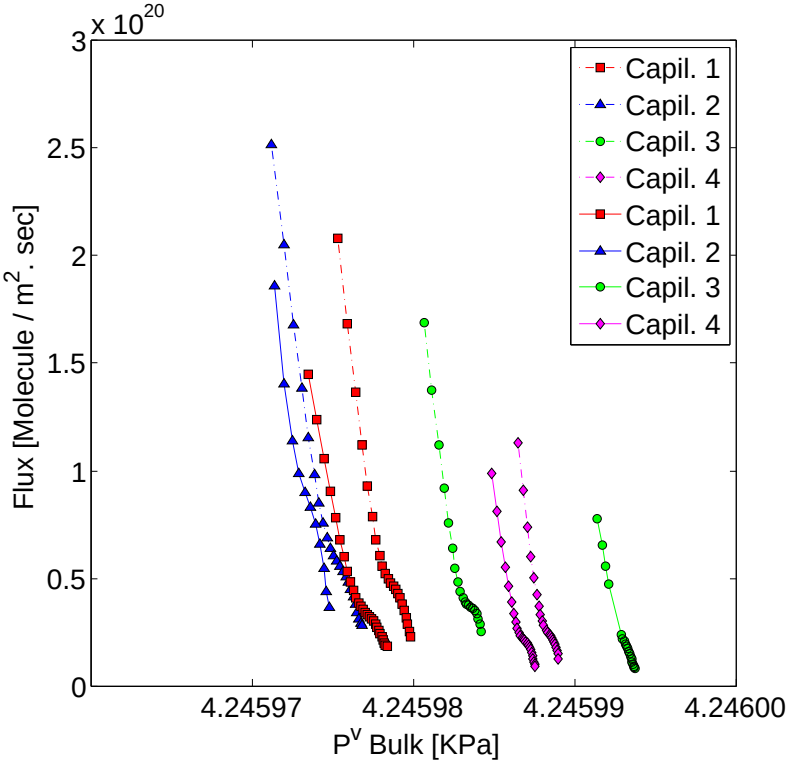

Figure 6.14: Flux as a function of bulk phase vapor pressure for both containers at $30°C$, working fluid: water. Dashed lines represent container 1.

6.2.2 Evaporation of other liquids

In order to expand our understanding of the phenomena of evaporation in a closed, constant temperature and volume system that is impermeable to mass transfer, for liquids other than distilled deionized water, the tests were preformed for octane (C_8H_{18}) and methylcyclohexane (C_7H_{14}). The temperature chosen for these case studies was $51°C$.

The data set obtained for both containers with octane as the working liquid is delineated in Fig. 6.15 and Fig. 6.16.

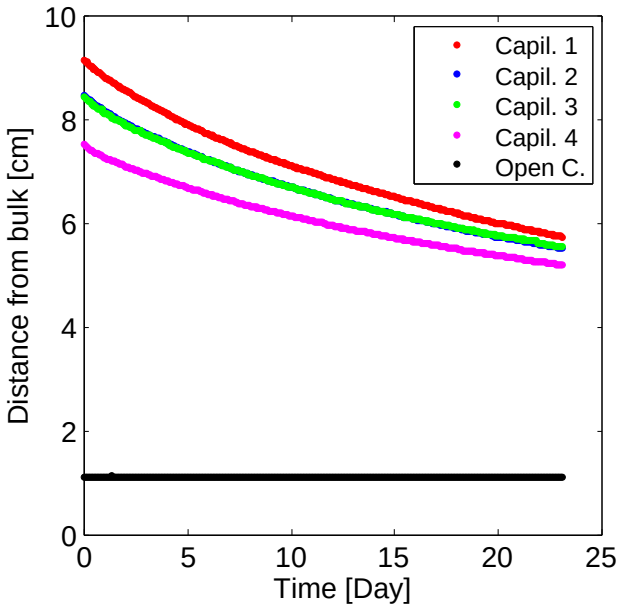

Figure 6.15: Measured interface position for container 1 at $51°C$, working fluid: octane.

Evidently, the CST pattern is repeated in these data sets as well. It should be pointed out that in order to further scrutinize the role of initial starting height at the evaporation rate from the capillaries, in case of container 1, capillaries 2 and 3 were filled at the same initial height. As depicted in Fig. 6.15, it is apparent

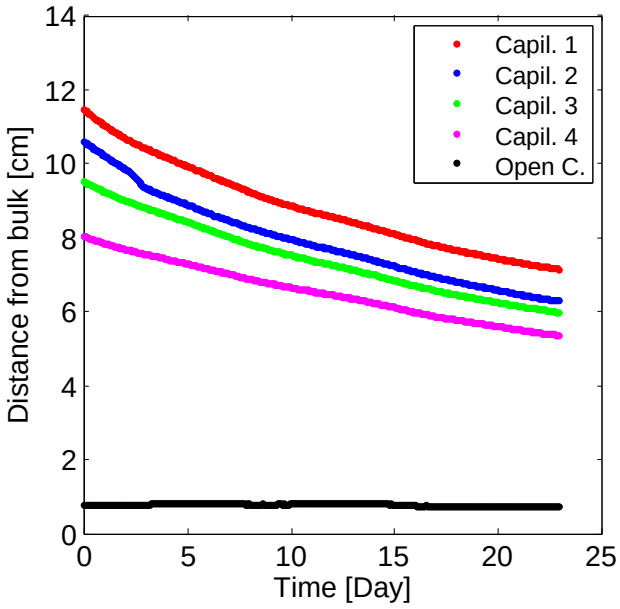

Figure 6.16: Measured interface position for container 2 at $51°C$, working fluid: octane.

that they both follow the same trend and thus experience the similar rate of change in height. As astonished as it made the author to make such a statement, intuitively, it can be deduced that in case of an evaporating meniscus into any such system (i.e. constant volume and temperature which is impermeable to mass transfer), the rate at which liquids evaporate is highly dependent to its previous history and initial conditions. In other words, its location from the bulk liquid phase as well as its distance from the tip of the capillary.

Consequently the results were re-plotted to illustrate the evaporation flux and they are given in Fig. 6.17 and Fig.6.18.

In Fig. 6.19 the evaporation rate for capillaries in both containers vs. the bulk liquid phase is plotted.

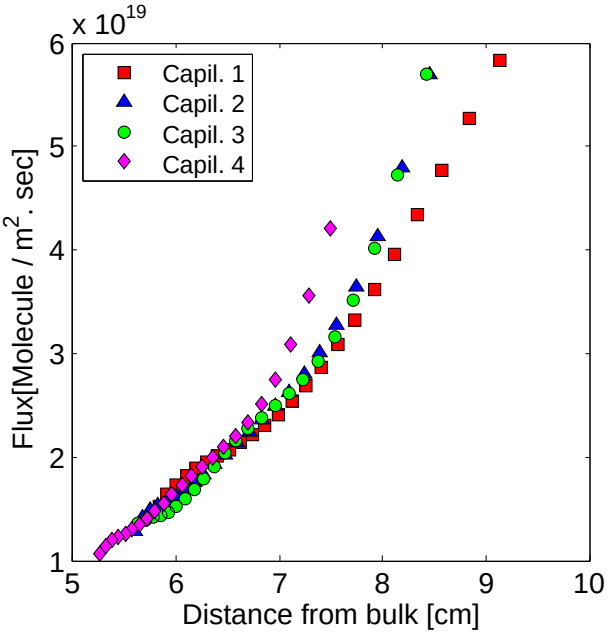

Figure 6.17: Calculated flux vs. interface position for container 1 at $51°C$, working fluid: octane.

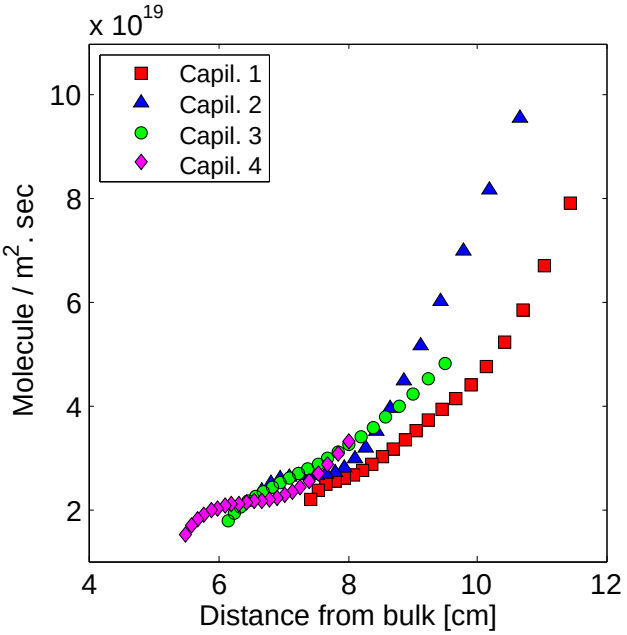

Figure 6.18: Calculated flux vs. interface position for container 2 at $51°C$, working fluid: octane.

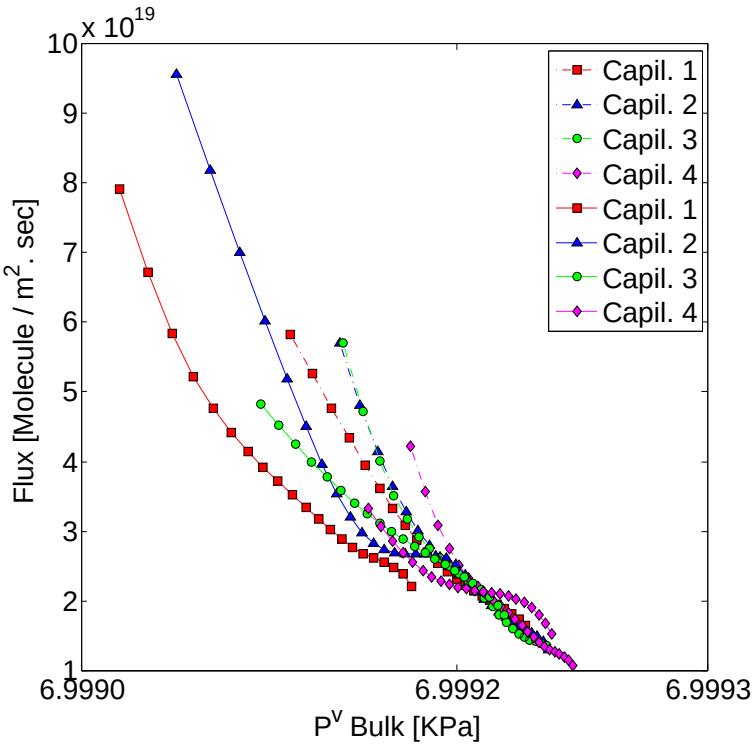

Figure 6.19: Flux as a function of bulk phase vapor pressure for both containers at $51°C$, working fluid: octane. Dashed lines represent container 1.

In Fig. 6.20 and Fig. 6.21 the meniscus location as a function of time, is given for methylcyclohexane as the working liquid at $51°C$.

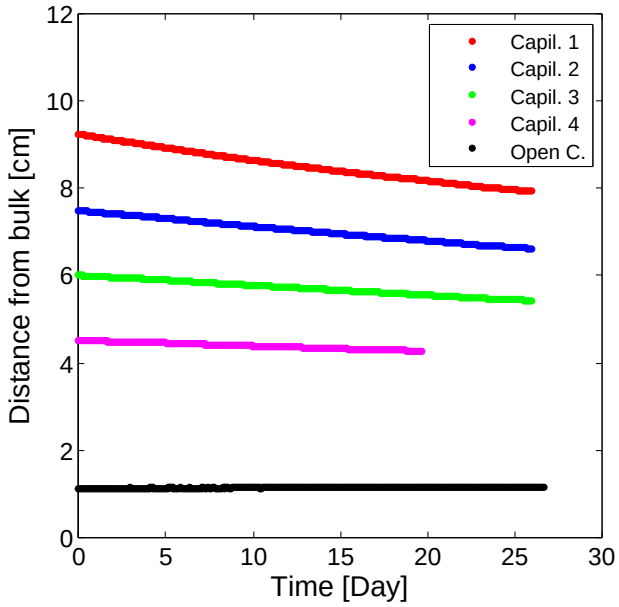

Figure 6.20: Measured interface position for container 1 at $51°C$, working fluid: methylcyclohexane.

As delineated in location vs. time figures, it can be deduced that the CST pattern is commonly repeated in both cases. However, the evaporation from the capillaries appears to be much slower than the cases where water and octane were used as the working liquids.

The evaporation flux as a function of vapor phase pressure can be seen in Fig. 6.22 and Fig. 6.23.

Finally, the evaporation fluxes for both capillaries as a function of bulk liquid pressure can be seen in Fig. 6.24. From the figure, it is evident that as as the vapor pressure above the meniscus increases the evaporation rate decreases.

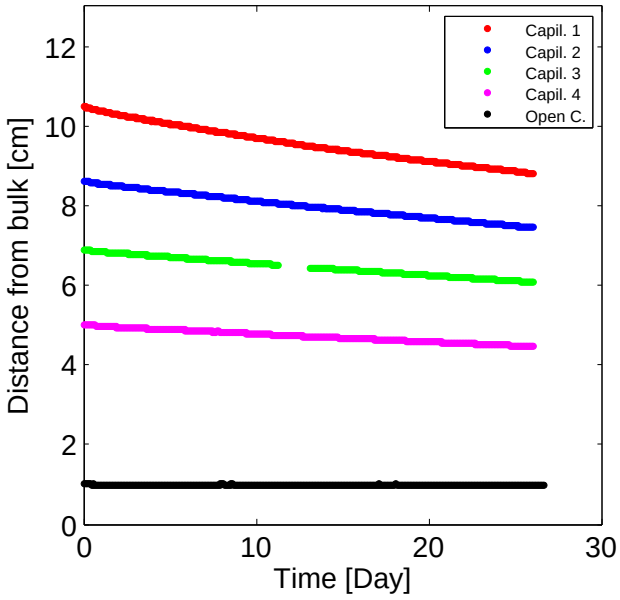

Figure 6.21: Measured interface position for container 2 at $51°C$, working fluid: methylcyclohexane.

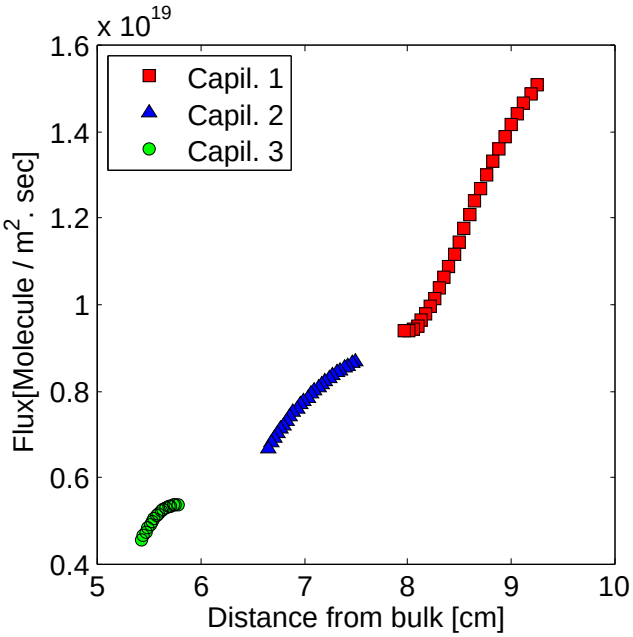

Figure 6.22: Calculated flux vs. interface position for container 1 at $51°C$, working fluid: methylcyclohexane.

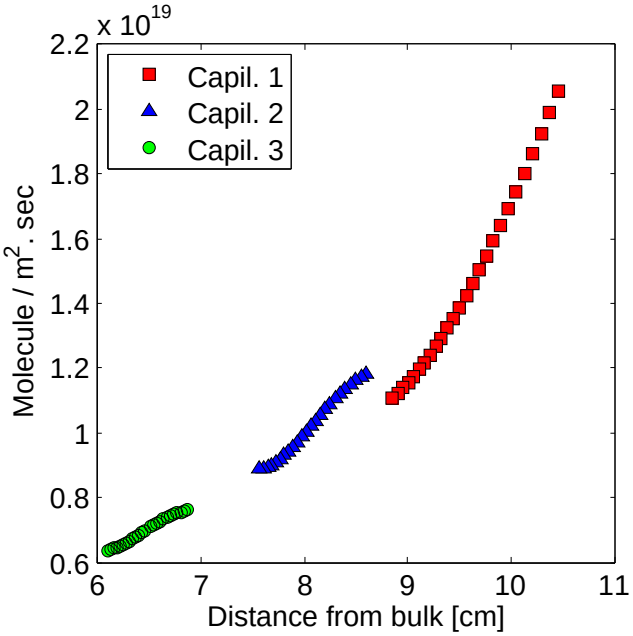

Figure 6.23: Calculated flux vs. interface position for container 2 at $51°C$, working fluid: methylcyclohexane.

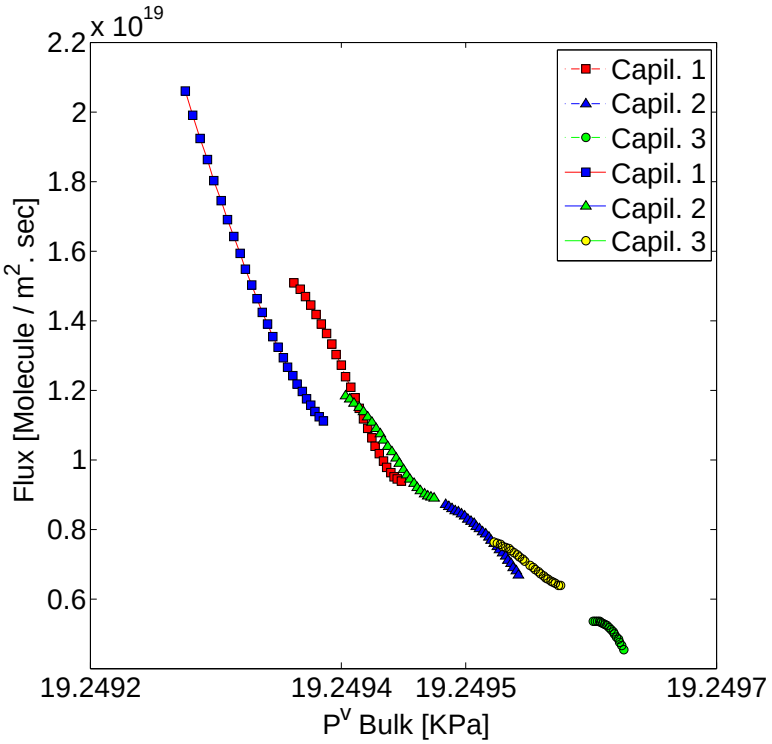

Figure 6.24: Flux as a function of bulk phase vapor pressure for both containers at $51°C$, working fluid: methylcyclohexane. Connecting dashed lines represent container 1.

6.3 Summary and Concluding Remarks

This work was inspired by the notion that even a minute (i.e. on the order of 10^{-4} Pascals) difference in pressure above an evaporating meniscus (that is in the vicinity of equilibrium condition) can significantly alter the evaporation rate.

With all the elaborate intricacies involved in creating any such controlled environment, the theorized notion that called for the vapor pressure as the most influential and sole factor on the rate of evaporation of liquids, was found to be insufficient. The experimental results manifested evidence that would require other factors to be equally as important on the rate of evaporation of liquids in near to equilibrium conditions. For instance, the location of meniscus from the tip of the capillary, the vapor diffusion rate out and away from the interface relative to the evaporation rate.

The observations presented in this work are the product of numerous hours of meticulous preparation and precise post processing of raw data, which raise questions about relative significance of the effect of pressure above an evaporating meniscus on its evaporation rate. To make a conjecture with such certitude (as done by Rahimi et.al. [4]) could not be supported by the present work. As mentioned before, this class of evaporation (i.e. from capillaries in a near equilibrium condition) requires a more detailed model to capture an inherent physical phenomenon such as mass diffusion way from the evaporating meniscus. Intuitively, and based on the manifestation of the collected experimental data in this work, to declare pressure above the liquid interface of an evaporating meniscus receding inside a capillary (of close to equilibrium conditions) was proven to be inconclusive.

In case of the effect of bulk liquid shape (i.e. which determines the vapor

pressure at the apex), on the rate of evaporation the following factors should be taken into consideration. First,the initial location of the meniscus above the bulk must be the same at the time when the system reaches equilibrium (i.e. the starting point for counting in the data) before one could make such comparison between the two containers. This, condition although not impossible to create but is virtually unattainable due to the following reasons: first, the initial vacuuming of the containers before starting the experiment makes it impossible to have a control over the level of the liquid meniscus above the bulk level; second, initial evolution (within the first 12-24 hours) that the system undergoes before reaching a near equilibrium state; and finally, the volume of the containers must be identical, which due to their custom design build is very difficult to achieve. However, from an observational point of view, the evaporation from the container with a lower liquid pressure at the apex of the bulk seems to be lower than that of with lower vapor pressure at the similar location. Lastly, it should be pointed out that in case there was a leak in a container no evaporation from the capillaries would occur.

Despite all of the aforementioned difficulties and modeling challenges the evaporation processes that were approaching equilibrium followed a Commonly-Shared-Trend (CST). The CST include the monotonic decrease in the hight of the meniscuses, a higher slope within the early days of the experiment which lessens through to the final days of the test, and finally a capillary starting with a higher meniscus location exhibit a higher change in height than that with lower starting points.

	Liquid	Temperature $°C$	Bulk liquid Pressure [pa]
Container1	Water	30	4.239138e+3
	Water	40	7.375663e+3
	Water	51	13.368353e+3
	Octane	51	6.99825e+3
	Methylcyclohexane	51	19.248854e+3
Container2	Liquid	Temperature $°C$	Bulk liquid Pressure [pa]
	Water	30	4.223444e+3
	Water	51	13.358929e+3
	Water	62	21.159366e+3
	Octane	51	6.9944e+3
	Methylcyclohexane	51	19.244789e+3

Table 6.2: Estimated bulk liquid pressure for both containers under working conditions.

Chapter 7

Summary and future work

7.1 Summary

Chapters 1, and 2 gave an overview about the phenomenon of evaporation, its importance and applications in industry and pure scientific advancements made in this field of studies, as well as some of the proposed models used in estimation of the evaporation flux and other relevant literature review helping in comprehending the underlying physics of this phenomena. In Chapter 3, classical thermodynamic relations were used to determine the equilibrium conditions for the system of study. It was also shown that by having certain geometrical dimensions of the interface, the radius of curvature could be estimated which ultimately would be used to numerically calculate the bulk liquid pressure in the system. In Chapter 4, SRT and its applications in predicting nonequilibrium processes was introduced and with the use of statistical thermodynamics an expression for the net evaporation flux was expressed. This expression is free of any fitting parameters and by having the net evaporation flux estimates the vapor phase pressure. Chapter 5, discussed the experimental setup, apparatus and techniques used for collecting data. The experimentally gathered data and post processing of the results was provided in Chapter 6.

In this thesis, the underlying physics behind evaporation of liquids in near equilibrium conditions from capillary tubes was studied. This work was performed to further expand our understanding of such a phenomenon focusing on the effect of pressure above an evaporating meniscus on the rate of evaporation of liquids from a capillary tube, and gather the much required experimental data to fill the gap between the proposed model (i.e. SRT) and the experimental observations.

Furthermore, the exploration of this phenomena expanded by introducing two containers with a difference in their geometry. The variation in the geometry of the containers affect the bulk liquid pressure (on the order of 10^{-2} Pascals difference) and thus prescribed slightly different pressure in each case study. This scrutiny was aimed to divulge the hypothesized notion that calls for the vapor pressure above an evaporating meniscus as the prevailing factor that ultimately controls the rate of evaporation in liquids.

The experimental results delineated in Chapter 6, revealed that even though, as thought before, pressure has a role in determining the rate of evaporation of liquids, for the case where the evaporation takes place from a receding meniscus in a capillary tube, a model should be used to also include the nonequilibrium aspects of the vapor flux away from the meniscus in a close to equilibrium conditions.

By reviewing the results provided in Chapter 6, the following empirical conclusions are apparent. The monotonic decrease in the height of the meniscuses, a higher slope within in the early days of the experiment which lessens through to the final days of the test, and finally a capillary starting with a higher meniscus location exhibits a higher change in height than that of lower starting points.

7.2 Future work

7.2.1 Introduction of mass diffusion into the numerical model

To be precise, the numerical model suggested in chapter 3 ought to be reworked to include the mass diffusion out and away from an evaporating meniscus entrapped inside a capillary tube and how this may effect the pressure experienced at the interface. The existing model lacks the ability to capture and predict evaporation rate with the precision required for this phenomena occurring inside a capillary tube. That could be a reason behind the deviation of experimental observation from what is anticipated according to the preliminary SRT model, i.e. the evaporation rate from a meniscus at similar position above the bulk liquid should be the same.

7.2.2 On the treatment of glass surface

During the course of experiments, over time, the unwanted accumulation of condensation on the glass surface obscured the capillaries and thus the meniscus within. Henceforth, this excessive sweating and its attenuating effect on collecting valuable data should be eliminated. As a suggestion, the surface of the glass containers could be coated with Teflon. This would make the surfaces hydrophobic, and as a result the condensed vapor would easily bead and run down the glass surface, leaving the view of the capillary tubes clear.

Another recommendation is to apply vacuum grease on the O-rings, except for the ones on the filling line. The vacuum grease should be inert and non-melting, Dow Corning® high vacuum grease could be a suitable candidate for this purpose. Experience showed that there is a fine line between tightening the fittings such that the glass parts could tolerate the pressure while withholding

the vacuum during the lengthy course of each experiment (e.g. a minimum of 20 days). Since the vacuum grease was not used, sometimes the delicate and cautious efforts in tightening the fittings caused the lids' tube to crack, and in a few occasions the canisters themselves, making the preparation of the setup even more time consuming, and cumbersome.

Last but not least, using cameras with higher pixel intensity, better sensors, and lenses with better optical qualities would indeed enhance the precision of collected data.

Appendix

Time [Day]	Loc.±0.01 [cm]	Flux $\times 10^{-19}$ $[\frac{molec}{m^2 sec}]$	$P^V_{eq} \pm 10^{-7}$ [KPa]	$P^V_{SRT} \pm 10^{-5}$ [KPa]
0	4.08	20.79826	4.2459876	4.24599
1	3.98	16.83277	4.2459880	4.24599
2	3.89	13.66690	4.2459882	4.24599
3	3.83	11.18420	4.2459884	4.24599
4	3.77	9.27684	4.2459886	4.24599
5	3.72	7.84566	4.2459887	4.24599
6	3.68	6.80014	4.2459888	4.24599
7	3.65	6.05838	4.2459889	4.24599
8	3.61	5.54717	4.2459890	4.24599
9	3.58	5.20190	4.2459891	4.24599
10	3.56	4.96662	4.2459892	4.24599
11	3.53	4.79405	4.2459893	4.24599
12	3.50	4.64552	4.2459894	4.24599
13	3.48	4.49101	4.2459894	4.24599
14	3.45	4.30917	4.2459895	4.24599
15	3.43	4.08726	4.2459896	4.24599
16	3.41	3.82121	4.2459896	4.24599
17	3.39	3.51559	4.2459897	4.24599
18	3.37	3.18360	4.2459898	4.24599
19	3.35	2.84710	4.2459898	4.24599
20	3.34	2.53658	4.2459899	4.24599
21	3.32	2.29121	4.2459899	4.24599
22	3.31	2.15876	4.2459899	4.24599

Table A.1: Container One - Capillary One @ 30° C

Time [Day]	Loc.±0.01 [cm]	Flux $\times 10^{-19}$ $[\frac{molec}{m^2 sec}]$	$P_{eq}^{V} \pm 10^{-7}$ [KPa]	$P_{SRT}^{V} \pm 10^{-5}$ [KPa]
0	4.77	25.17193	4.2459856	4.24598
1	4.64	20.52953	4.2459860	4.24599
2	4.54	16.79976	4.2459863	4.24599
3	4.46	13.85071	4.2459865	4.24599
4	4.39	11.56036	4.2459867	4.24599
5	4.33	9.81653	4.2459869	4.24599
6	4.28	8.51688	4.2459871	4.24599
7	4.23	7.56896	4.2459872	4.24599
8	4.19	6.89016	4.2459873	4.24599
9	4.16	6.40771	4.2459874	4.24599
10	4.12	6.05873	4.2459875	4.24599
11	4.09	5.79015	4.2459876	4.24599
12	4.06	5.55881	4.2459877	4.24599
13	4.03	5.33136	4.2459878	4.24599
14	4.00	5.08432	4.2459879	4.24599
15	3.97	4.80408	4.2459880	4.24599
16	3.94	4.48688	4.2459881	4.24599
17	3.92	4.13880	4.2459881	4.24599
18	3.90	3.77579	4.2459882	4.24599
19	3.88	3.42366	4.2459882	4.24599
20	3.86	3.11805	4.2459883	4.24599
21	3.84	2.90450	4.2459883	4.24599
22	3.83	2.83836	4.2459884	4.24599

Table A.2: Container One - Capillary Two @ 30° C

Time [Day]	Loc.±0.01 [cm]	Flux $\times 10^{-19}$ $[\frac{molec}{m^2 sec}]$	$P_{eq}^{V} \pm 10^{-7}$ [KPa]	$P_{SRT}^{V} \pm 10^{-5}$ [KPa]
0	3.18	16.89378	4.2459903	4.24599
1	3.10	13.75679	4.2459906	4.24599
2	3.03	11.21143	4.2459908	4.24599
3	2.97	9.18057	4.2459909	4.24599
4	2.93	7.59195	4.2459911	4.24599
5	2.89	6.37815	4.2459912	4.24599
6	2.86	5.47661	4.2459913	4.24599
7	2.83	4.82962	4.2459914	4.24599
8	2.80	4.38434	4.2459915	4.24599
9	2.78	4.09277	4.2459915	4.24599
10	2.76	3.91177	4.2459916	4.24599
11	2.74	3.80306	4.2459916	4.24599
12	2.71	3.73321	4.2459917	4.24599
13	2.69	3.67365	4.2459918	4.24599
14	2.67	3.60065	4.2459918	4.24599
15	2.65	3.49536	4.2459919	4.24599
16	2.64	3.34378	4.2459919	4.24599
17	2.62	3.13673	4.2459920	4.24599
18	2.60	2.86994	4.2459921	4.24599
19	2.59	2.54395	4.2459921	4.24599

Table A.3: Container One - Capillary Three @ 30° C

Time [Day]	Loc.±0.01 [cm]	Flux $\times 10^{-19}$ $[\frac{molec}{m^2 sec}]$	$P_{eq}^{V} \pm 10^{-7}$ [KPa]	$P_{SRT}^{V} \pm 10^{-5}$ [KPa]
0	2.21	11.29078	4.2459932	4.24599
1	2.15	9.08321	4.2459934	4.24599
2	2.10	7.35780	4.2459935	4.24599
3	2.07	6.02808	4.2459936	4.24599
4	2.04	5.01870	4.2459937	4.24599
5	2.01	4.26458	4.2459938	4.24599
6	1.99	3.71017	4.2459939	4.24599
7	1.97	3.30863	4.2459939	4.24599
8	1.95	3.02105	4.2459940	4.24599
9	1.94	2.81563	4.2459940	4.24599
11	1.91	2.55514	4.2459941	4.24599
12	1.89	2.46504	4.2459942	4.24599
13	1.88	2.38553	4.2459942	4.24599
14	1.87	2.30861	4.2459942	4.24599
15	1.85	2.22871	4.2459943	4.24599
16	1.84	2.14184	4.2459943	4.24599
17	1.83	2.04480	4.2459943	4.24599
18	1.82	1.93443	4.2459944	4.24599
19	1.81	1.80677	4.2459944	4.24599
20	1.80	1.65631	4.2459944	4.24599
21	1.79	1.47518	4.2459945	4.24599
22	1.78	1.25233	4.2459945	4.24599

Table A.4: Container One - Capillary Four @ 30° C

Time [Day]	Loc.±0.01 [cm]	Flux $\times 10^{-19}$ $[\frac{molec}{m^2 sec}]$	$P_{eq}^{V} \pm 10^{-7}$ [KPa]	$P_{SRT}^{V} \pm 10^{-5}$ [KPa]
0	4.23	14.48914	4.2459867	4.24599
1	4.14	12.36242	4.2459870	4.24599
2	4.07	10.56744	4.2459872	4.24599
3	4.00	9.06667	4.2459874	4.24599
4	3.95	7.82478	4.2459876	4.24599
5	3.90	6.80859	4.2459877	4.24599
6	3.86	5.98708	4.2459878	4.24599
7	3.82	5.33144	4.2459879	4.24599
8	3.79	4.81499	4.2459880	4.24599
9	3.76	4.41323	4.2459881	4.24599
10	3.73	4.10385	4.2459882	4.24599
11	3.70	3.86669	4.2459883	4.24599
12	3.68	3.68376	4.2459884	4.24599
13	3.66	3.53924	4.2459884	4.24599
14	3.63	3.41950	4.2459885	4.24599
15	3.61	3.31306	4.2459886	4.24599
16	3.59	3.21060	4.2459886	4.24599
17	3.57	3.10501	4.2459887	4.24599
18	3.55	2.99131	4.2459888	4.24599
19	3.53	2.86670	4.2459888	4.24599
20	3.51	2.73057	4.2459889	4.24599
21	3.49	2.58445	4.2459889	4.24599
22	3.48	2.43207	4.2459890	4.24599
23	3.46	2.27931	4.2459890	4.24599
24	3.45	2.13422	4.2459891	4.24599
25	3.43	2.00702	4.2459891	4.24599
26	3.42	1.91012	4.2459891	4.24599
27	3.41	1.85808	4.2459892	4.24599

Table A.5: Container Two - Capillary One @ 30° C

Time [Day]	Loc.±0.01 [cm]	Flux $\times 10^{-19}$ $[\frac{molec}{m^2 sec}]$	$P_{eq}^{V} \pm 10^{-7}$ [KPa]	$P_{SRT}^{V} \pm 10^{-5}$ [KPa]
0	4.58	18.61720	4.2459857	4.24599
1	4.47	14.06828	4.2459860	4.24599
2	4.39	11.39713	4.2459862	4.24599
3	4.32	9.89534	4.2459864	4.24599
4	4.26	9.00214	4.2459866	4.24599
5	4.21	8.30447	4.2459868	4.24599
6	4.15	7.53696	4.2459870	4.24599
7	4.11	6.58192	4.2459871	4.24599
8	4.07	5.46934	4.2459872	4.24599
9	4.04	4.37689	4.2459873	4.24599
10	4.01	3.62993	4.2459874	4.24599

Table A.6: Container Two - Capillary Two @ 30° C

Time [Day]	Loc.±0.01 [cm]	Flux $\times 10^{-19}$ $[\frac{molec}{m^2 sec}]$	$P_{eq}^{V} \pm 10^{-7}$ [KPa]	$P_{SRT}^{V} \pm 10^{-5}$ [KPa]
0	1.21	7.76088	4.2459957	4.24599
1	1.17	6.55677	4.2459958	4.24599
2	1.13	5.56340	4.2459960	4.24599
3	1.09	4.75221	4.2459961	4.24599
9	0.96	2.36669	4.2459964	4.24599
10	0.95	2.20151	4.2459965	4.24599
11	0.94	2.06319	4.2459965	4.24599
12	0.92	1.94147	4.2459966	4.24599
13	0.91	1.82814	4.2459966	4.24599
14	0.90	1.71703	4.2459966	4.24599
15	0.89	1.60400	4.2459967	4.24599
16	0.88	1.48694	4.2459967	4.24599
17	0.87	1.36580	4.2459967	4.24599
18	0.86	1.24254	4.2459968	4.24599
19	0.85	1.12117	4.2459968	4.24599
20	0.85	1.00775	4.2459968	4.24599
21	0.84	0.91034	4.2459968	4.24599
22	0.83	0.83907	4.2459968	4.24599
23	0.83	0.80610	4.2459968	4.24599

Table A.7: Container Two - Capillary Three @ 30° C

Time [Day]	Loc.±0.01 [cm]	Flux $\times 10^{-19}$ $[\frac{molec}{m^2 sec}]$	$P_{eq}^{V} \pm 10^{-7}$ [KPa]	$P_{SRT}^{V} \pm 10^{-5}$ [KPa]
0	2.32	9.88960	4.2459924	4.24599
1	2.26	8.13009	4.2459926	4.24599
2	2.21	6.69298	4.2459927	4.24599
3	2.17	5.53619	4.2459928	4.24599
4	2.14	4.62040	4.2459929	4.24599
5	2.11	3.90907	4.2459930	4.24599
6	2.09	3.36844	4.2459931	4.24599
7	2.07	2.96750	4.2459932	4.24599
8	2.05	2.67801	4.2459932	4.24599
9	2.03	2.47450	4.2459933	4.24599
10	2.02	2.33428	4.2459933	4.24599
11	2.00	2.23742	4.2459934	4.24599
12	1.99	2.16674	4.2459934	4.24599
13	1.97	2.10787	4.2459934	4.24599
14	1.96	2.04917	4.2459935	4.24599
15	1.95	1.98178	4.2459935	4.24599
16	1.94	1.89962	4.2459936	4.24599
17	1.92	1.79936	4.2459936	4.24599
18	1.91	1.68046	4.2459936	4.24599
19	1.90	1.54513	4.2459937	4.24599
20	1.89	1.39834	4.2459937	4.24599
21	1.88	1.24786	4.2459937	4.24599
22	1.88	1.10421	4.2459937	4.24599
23	1.87	0.98067	4.2459938	4.245993
24	1.86	0.89330	4.2459938	4.245993

Table A.8: Container Two - Capillary Four @ 30° C

Time [Day]	Loc.±0.01 [cm]	Flux $\times 10^{-19}$ $[\frac{molec}{m^2 sec}]$	$P^V_{eq} \pm 10^{-6}$ [KPa]	$P^V_{SRT} \pm 10^{-5}$ [KPa]
0	4.73	39.0286	7.383976	7.38398
2	4.36	29.0785	7.383978	7.38398
4	4.08	21.8400	7.383979	7.38398
6	3.87	16.7260	7.383980	7.38398
8	3.71	13.2259	7.383981	7.38399
10	3.58	10.9065	7.383982	7.38399
12	3.47	9.4110	7.383982	7.38399
14	3.37	8.4549	7.383983	7.38399
16	3.28	7.8213	7.383983	7.38399
18	3.20	7.3535	7.383984	7.38399
20	3.12	6.9477	7.383984	7.38399
22	3.05	6.5437	7.383984	7.38399
24	2.98	6.1165	7.383985	7.38399
26	2.92	5.6665	7.383985	7.38399
28	2.86	5.2110	7.383985	7.38399
30	2.80	4.7754	7.383986	7.38399
32	2.75	4.3859	7.383986	7.38399
34	2.71	4.0631	7.383986	7.38399
36	2.66	3.8175	7.383986	7.38399
38	2.62	3.6467	7.383986	7.38399
40	2.58	3.5347	7.383987	7.38399
42	2.55	3.4542	7.383987	7.38399
44	2.51	3.3713	7.383987	7.38399
46	2.47	3.2543	7.383987	7.38399
48	2.44	3.0848	7.383987	7.38399
50	2.41	2.8743	7.383988	7.38399
52	2.37	2.6835	7.383988	7.38399
54	2.35	2.6476	7.383988	7.38399

Table A.9: Container One - Capillary One @ 40° C

Time [Day]	Loc.±0.01 [cm]	Flux $\times 10^{-19}$ $[\frac{molec}{m^2 sec}]$	$P_{eq}^{V} \pm 10^{-6}$ [KPa]	$P_{SRT}^{V} \pm 10^{-4}$ [KPa]
0	2.70	18.9519	7.383986	7.3840
2	2.52	14.6414	7.383987	7.3840
4	2.37	11.3625	7.383988	7.3840
6	2.26	8.9473	7.383988	7.3840
8	2.18	7.2286	7.383989	7.3840
10	2.10	6.0484	7.383989	7.3840
12	2.04	5.2640	7.383989	7.3840
14	1.99	4.7521	7.383990	7.3840
16	1.94	4.4117	7.383990	7.3840
18	1.89	4.1644	7.383990	7.3840
20	1.85	3.9541	7.383990	7.3840
22	1.81	3.7452	7.383991	7.3840
24	1.77	3.5199	7.383991	7.3840
26	1.73	3.2751	7.383991	7.3840
28	1.69	3.0183	7.383991	7.3840
30	1.66	2.7638	7.383991	7.3840
32	1.63	2.5288	7.383991	7.3840
34	1.61	2.3292	7.383992	7.3840
36	1.58	2.1769	7.383992	7.3840
38	1.56	2.0765	7.383992	7.3840
40	1.54	2.0244	7.383992	7.3840
42	1.51	2.0073	7.383992	7.3840
44	1.49	2.0040	7.383992	7.3840
46	1.47	1.9871	7.383992	7.3840
48	1.45	1.9277	7.383992	7.3840

Table A.10: Container One - Capillary Two @ 40° C

Time [Day]	Loc.±0.01 [cm]	Flux $\times 10^{-19}$ $[\frac{molec}{m^2 sec}]$	$P_{eq}^{V} \pm 10^{-5}$ [KPa]	$P_{SRT}^{V} \pm 10^{-4}$ [KPa]
0	1.69	14.2903	7.38399	7.3840
2	1.55	10.9980	7.38399	7.3840
4	1.45	8.5621	7.38399	7.3840
6	1.36	6.8028	7.38399	7.3840
8	1.30	5.5635	7.38399	7.3840
10	1.24	4.7108	7.38399	7.3840
12	1.19	4.1332	7.38399	7.3840
14	1.15	3.7407	7.38399	7.3840
16	1.11	3.4629	7.38399	7.3840
30	0.90	2.0671	7.38400	7.3840
32	0.88	1.8814	7.38400	7.3840
34	0.86	1.7232	7.38400	7.3840
36	0.84	1.6014	7.38400	7.3840
38	0.82	1.5213	7.38400	7.3840
40	0.81	1.4826	7.38400	7.3840
42	0.79	1.4788	7.38400	7.3840
44	0.77	1.4963	7.38400	7.3840
46	0.76	1.5141	7.38400	7.3840
48	0.74	1.5045	7.38400	7.3840

Table A.11: Container One - Capillary Three @ 40° C

Time [Day]	Loc.±0.01 [cm]	Flux $\times 10^{-19}$ $[\frac{molec}{m^2 sec}]$	$P_{eq}^{V} \pm 10^{-6}$ [KPa]	$P_{SRT}^{V} \pm 10^{-4}$ [KPa]
0	0.71	13.2275	7.383996	7.3839
2	0.59	9.7243	7.383997	7.3839
4	0.50	7.5222	7.383997	7.3839
6	0.42	6.1483	7.383997	7.3839
36	-0.06	1.5002	7.384000	7.3839
38	-0.08	1.4880	7.384000	7.3839
40	-0.09	1.4840	7.384000	7.3839
42	-0.11	1.4833	7.384000	7.3839
44	-0.13	1.4811	7.384000	7.3839
46	-0.14	1.4704	7.384000	7.3839
48	-0.16	1.4359	7.384000	7.3839

Table A.12: Container One - Capillary Four @ 40° C

Time [Day]	Loc.±0.01 [cm]	Flux $\times 10^{-20}$ $[\frac{molec}{m^2 sec}]$	$P_{eq}^{V} \pm 10^{-5}$ [KPa]	$P_{SRT}^{V} \pm 10^{-5}$ [KPa]
0	2.31	6.409904	13.37597	13.37596
1	2.00	4.734102	13.37598	13.37597
2	1.76	3.712643	13.37598	13.37597
3	1.57	3.028383	13.37598	13.37597
4	1.41	2.519292	13.37598	13.37597
5	1.28	2.114692	13.37598	13.37597
6	1.17	1.790083	13.37598	13.37597
7	1.07	1.537721	13.37599	13.37597
8	0.99	1.350094	13.37599	13.37597
9	0.92	1.213481	13.37599	13.37597
10	0.85	1.108717	13.37599	13.37597
11	0.79	1.016360	13.37599	13.37597
12	0.74	0.923386	13.37599	13.37597
13	0.69	0.828601	13.37599	13.37597
14	0.64	0.743902	13.37599	13.37597
15	0.60	0.688563	13.37599	13.37597
16	0.56	0.673704	13.37599	13.37597
17	0.53	0.674093	13.37599	13.37597
18	0.49	0.584444	13.37599	13.37597

Table A.13: Container One - Capillary One @ 51° C

Time [Day]	Loc.±0.01 [cm]	Flux $\times 10^{-20}$ $[\frac{molec}{m^2 sec}]$	$P_{eq}^{V} \pm 10^{-6}$ [KPa]	$P_{SRT}^{V} \pm 10^{-5}$ [KPa]
0	1.95	5.749158	13.375982	13.37597
1	1.67	4.186435	13.375985	13.37597
2	1.46	3.214785	13.375986	13.37597
3	1.30	2.607324	13.375988	13.37597
4	1.16	2.205243	13.375989	13.37597
6	0.94	1.654870	13.375991	13.37597
7	0.86	1.428109	13.375992	13.37597
8	0.78	1.227290	13.375992	13.37597
9	0.72	1.065269	13.375993	13.37597
10	0.66	0.955488	13.375994	13.37597
11	0.61	0.900734	13.375994	13.37597
12	0.55	0.881887	13.375994	13.37597
13	0.51	0.846675	13.375995	13.37597

Table A.14: Container One - Capillary Two @ 51° C

Time [Day]	Loc.±0.01 [cm]	Flux $\times 10^{-20}$ $[\frac{molec}{m^2 sec}]$	$P_{eq}^{V} \pm 10^{-5}$ [KPa]	$P_{SRT}^{V} \pm 10^{-5}$ [KPa]
0	1.50	4.170492	13.37598	13.37597
1	1.28	3.426092	13.37598	13.37597
2	1.10	2.806738	13.37599	13.37597
3	0.96	2.299946	13.37599	13.37597
4	0.84	1.893228	13.37599	13.37597
5	0.74	1.574098	13.37599	13.37597
6	0.66	1.330070	13.37599	13.37597
7	0.59	1.148657	13.37599	13.37597
8	0.53	1.017374	13.37599	13.37597
9	0.47	0.923734	13.37599	13.37597
10	0.42	0.855251	13.37599	13.37597
11	0.38	0.799438	13.37599	13.37597
12	0.33	0.743809	13.37599	13.37597
13	0.29	0.675878	13.37599	13.37597
14	0.26	0.583158	13.37599	13.37597

Table A.15: Container One - Capillary Three @ 51° C

Time [Day]	Loc.±0.01 [cm]	Flux $\times 10^{-20}$ $[\frac{molec}{m^2 sec}]$	$P^V_{eq} \pm 10^{-6}$ [KPa]	$P^V_{SRT} \pm 10^{-4}$ [KPa]
0	0.93	3.777494	13.375991	13.3759
1	0.76	2.511475	13.375993	13.3759
2	0.63	1.971893	13.375994	13.3759
3	0.53	1.665632	13.375995	13.3759
4	0.44	1.420488	13.375995	13.3759
5	0.37	1.232597	13.375996	13.3759
6	0.30	1.113863	13.375997	13.3759
7	0.24	0.939386	13.375997	13.3759

Table A.16: Container One - Capillary Four @ 51° C

Time [Day]	Loc.±0.01 [cm]	Flux $\times 10^{-20}$ $[\frac{molec}{m^2 sec}]$	$P^V_{eq} \pm 10^{-6}$ [KPa]	$P^V_{SRT} \pm 10^{-4}$ [KPa]
1	3.00	6.429310	13.375972	13.3759
2	2.65	5.211623	13.375975	13.3759
3	2.36	4.330407	13.375977	13.3759
4	2.12	3.634417	13.375979	13.3759
5	1.92	3.067623	13.375981	13.3759
6	1.75	2.615622	13.375983	13.3759
7	1.60	2.272396	13.375984	13.3759
9	1.35	1.842591	13.375986	13.3759
10	1.25	1.695175	13.375987	13.3759
11	1.15	1.549554	13.375988	13.3759
12	1.06	1.387328	13.375989	13.3759
13	0.98	1.211886	13.375989	13.3759
14	0.91	1.050313	13.375990	13.3759
15	0.85	0.944964	13.375991	13.3759
16	0.80	0.930884	13.375991	13.3759

Table A.17: Container Two - Capillary One @ 51° C

Time [Day]	Loc.±0.01 [cm]	Flux $\times 10^{-20}$ $[\frac{molec}{m^2 sec}]$	$P^V_{eq} \pm 10^{-6}$ [KPa]	$P^V_{SRT} \pm 10^{-5}$ [KPa]
2	1.44	3.412606	13.375985	13.37597
3	1.24	3.083652	13.375987	13.37597
4	1.07	2.745368	13.375989	13.37597
5	0.91	2.410949	13.375990	13.37597
6	0.78	2.093593	13.375991	13.37597
7	0.66	1.806495	13.375992	13.37597
8	0.56	1.562851	13.375993	13.37597
9	0.47	1.375859	13.375994	13.37597
10	0.39	1.258714	13.375995	13.37597
11	0.31	1.224612	13.375995	13.37597

Table A.18: Container Two - Capillary Two @ 51° C

Time [Day]	Loc.±0.01 [cm]	Flux $\times 10^{-20}$ $[\frac{molec}{m^2 sec}]$	$P^V_{eq} \pm 10^{-5}$ [KPa]	$P^V_{SRT} \pm 10^{-5}$ [KPa]
1	1.18	4.290779	13.37598	13.3759
2	0.94	3.535236	13.37599	13.3759
3	0.74	2.919244	13.37599	13.3759
4	0.58	2.421598	13.37599	13.3759
5	0.45	2.023020	13.37599	13.3759
6	0.34	1.706156	13.37599	13.3759
7	0.24	1.455578	13.37599	13.3759
8	0.16	1.257783	13.37599	13.3759
9	0.09	1.101195	13.37599	13.3759
10	0.02	0.976160	13.37599	13.3759
11	-0.03	0.874953	13.37599	13.3759
12	-0.08	0.791773	13.37599	13.3759
13	-0.13	0.722744	13.37600	13.3759
14	-0.17	0.665916	13.37600	13.3759
15	-0.21	0.621264	13.37600	13.3759
16	-0.25	0.590689	13.37600	13.3759
17	-0.28	0.578016	13.37600	13.3759

Table A.19: Container Two - Capillary Three @ 51° C

Time [Day]	Loc.±0.01 [cm]	Flux $\times 10^{-20}$ $[\frac{molec}{m^2 sec}]$	$P_{eq}^{V} \pm 10^{-6}$ [KPa]	$P_{SRT}^{V} \pm 10^{-4}$ [KPa]
1	0.71	3.663154	13.375992	13.37597
2	0.51	2.850520	13.375994	13.37597
3	0.36	2.241645	13.375995	13.37597
4	0.24	1.796526	13.375996	13.37597
8	-0.08	1.001153	13.375999	13.37597
9	-0.14	0.922363	13.375999	13.37597
10	-0.19	0.855866	13.376000	13.37597
11	-0.24	0.791174	13.376000	13.37597
12	-0.29	0.722019	13.376001	13.37597
13	-0.33	0.646348	13.376001	13.37597
14	-0.37	0.566325	13.376001	13.37597
15	-0.40	0.488332	13.376002	13.37597
16	-0.43	0.422965	13.376002	13.37597
17	-0.45	0.385040	13.376002	13.37597

Table A.20: Container Two - Capillary Four @ 51° C

Time [Day]	Loc.±0.01 [cm]	Flux $\times 10^{-18}$ $[\frac{molec}{m^2 sec}]$	$P_{eq}^{V} \pm 10^{-6}$ [KPa]	$P_{SRT}^{V} \pm 10^{-5}$ [KPa]
0	9.14	58.2764	6.999133	6.99936
1	8.84	52.6697	6.999142	6.99936
2	8.58	47.7068	6.999150	6.99937
3	8.33	43.3358	6.999157	6.99937
4	8.12	39.5073	6.999163	6.99937
5	7.92	36.1738	6.999169	6.99937
6	7.73	33.2900	6.999174	6.99937
7	7.56	30.8119	6.999179	6.99937
8	7.40	28.6973	6.999184	6.99937
9	7.26	26.9051	6.999188	6.99937
10	7.12	25.3953	6.999192	6.99937
11	6.99	24.1288	6.999196	6.99937
12	6.86	23.0670	6.999199	6.99937
13	6.74	22.1718	6.999203	6.99937
14	6.63	21.4054	6.999206	6.99937
15	6.52	20.7300	6.999209	6.99937
16	6.41	20.1074	6.999213	6.99937
17	6.30	19.4994	6.999216	6.99937
18	6.20	18.8667	6.999219	6.99937
19	6.10	18.1695	6.999222	6.99937
20	6.01	17.3668	6.999224	6.99937
21	5.92	16.4166	6.999227	6.99937
22	5.83	15.2751	6.999229	6.99937

Table A.21: Container One - Capillary One @ 51° C, Working Liquid: Octane

Time [Day]	Loc.±0.01 [cm]	Flux $\times 10^{-18}$ $[\frac{molec}{m^2 sec}]$	$P^V_{eq} \pm 10^{-6}$ [KPa]	$P^V_{SRT} \pm 10^{-5}$ [KPa]
0	8.46	56.9800	6.999153	6.99936
1	8.18	48.0494	6.999161	6.99937
2	7.94	41.3890	6.999168	6.99937
3	7.74	36.4586	6.999174	6.99937
4	7.56	32.8114	6.999179	6.99937
5	7.39	30.0854	6.999184	6.99937
6	7.24	27.9949	6.999189	6.99937
7	7.09	26.3224	6.999193	6.99937
8	6.96	24.9095	6.999197	6.99937
9	6.83	23.6491	6.999200	6.99937
10	6.71	22.4766	6.999204	6.99937
11	6.59	21.3617	6.999207	6.99937
12	6.48	20.2993	6.999211	6.99937
13	6.37	19.3020	6.999214	6.99937
14	6.27	18.3908	6.999217	6.99937
15	6.18	17.5872	6.999219	6.99937
16	6.09	16.9044	6.999222	6.99937
17	6.00	16.3392	6.999224	6.99937
18	5.91	15.8629	6.999227	6.99937
19	5.83	15.4138	6.999229	6.99937
20	5.75	14.8878	6.999232	6.99937
21	5.67	14.1305	6.999234	6.99937
22	5.60	12.9286	6.999236	6.99937

Table A.22: Container One - Capillary Two @ 51° C, Working Liquid: Octane

Time [Day]	Loc.±0.01 [cm]	Flux $\times 10^{-18}$ $[\frac{molec}{m^2 sec}]$	$P_{eq}^{V} \pm 10^{-6}$ [KPa]	$P_{SRT}^{V} \pm 10^{-5}$ [KPa]
0	8.42	57.0086	6.999154	6.99936
1	8.15	47.1893	6.999162	6.99937
2	7.92	40.1324	6.999169	6.99937
3	7.72	35.1504	6.999174	6.99937
4	7.54	31.6732	6.999180	6.99937
5	7.38	29.2378	6.999184	6.99937
6	7.23	27.4785	6.999189	6.99937
7	7.09	26.1167	6.999193	6.99937
8	6.95	24.9509	6.999197	6.99937
9	6.83	23.8467	6.999200	6.99937
10	6.70	22.7264	6.999204	6.99937
11	6.58	21.5595	6.999207	6.99937
12	6.47	20.3520	6.999211	6.99937
13	6.37	19.1369	6.999214	6.99937
14	6.27	17.9636	6.999217	6.99937
15	6.18	16.8883	6.999219	6.99937
16	6.09	15.9637	6.999222	6.99937
17	6.01	15.2289	6.999224	6.99937
18	5.93	14.6996	6.999227	6.99937
19	5.85	14.3575	6.999229	6.99937
20	5.78	14.1408	6.999231	6.99937
21	5.70	13.9339	6.999233	6.99937
22	5.63	13.5573	6.999235	6.99937

Table A.23: Container One - Capillary Three @ 51° C, Working Liquid: Octane

Time [Day]	Loc.±0.01 [cm]	Flux $\times 10^{-18}$ $[\frac{molec}{m^2 sec}]$	$P^V_{eq} \pm 10^{-6}$ [KPa]	$P^V_{SRT} \pm 10^{-5}$ [KPa]
0	7.50	42.1427	6.999181	6.99937
1	7.29	35.6120	6.999187	6.99937
2	7.11	30.8844	6.999192	6.99937
3	6.96	27.5006	6.999197	6.99937
4	6.82	25.0834	6.999201	6.99937
5	6.69	23.3300	6.999204	6.99937
6	6.57	22.0050	6.999208	6.99937
7	6.46	20.9321	6.999211	6.99937
8	6.35	19.9875	6.999214	6.99937
9	6.25	19.0918	6.999217	6.99937
10	6.15	18.2027	6.999220	6.99937
11	6.06	17.3077	6.999223	6.99937
12	5.97	16.4163	6.999225	6.99937
13	5.88	15.5527	6.999228	6.99937
14	5.80	14.7483	6.999230	6.99937
15	5.72	14.0343	6.999233	6.99937
16	5.65	13.4339	6.999235	6.99937
17	5.58	12.9551	6.999237	6.99937
18	5.51	12.5831	6.999239	6.99937
19	5.45	12.2731	6.999241	6.99937
20	5.38	11.9422	6.999242	6.99937
21	5.32	11.4625	6.999244	6.99937
22	5.26	10.6534	6.999246	6.99937

Table A.24: Container One - Capillary Four @ 51° C, Working Liquid: Octane

Time [Day]	Loc.±0.01 [cm]	Flux $\times 10^{-18}$ $[\frac{molec}{m^2 sec}]$	$P_{eq}^{V} \pm 10^{-6}$ [KPa]	$P_{SRT}^{V} \pm 10^{-5}$ [KPa]
0	11.43	79.2189	6.999065	6.99936
1	11.04	67.1809	6.999076	6.99937
2	10.70	58.4748	6.999086	6.99937
3	10.41	52.1974	6.999095	6.99937
4	10.14	47.6257	6.999102	6.99937
5	9.90	44.1979	6.999109	6.99937
6	9.67	41.4945	6.999116	6.99937
7	9.45	39.2197	6.999122	6.99937
8	9.25	37.1822	6.999128	6.99937
9	9.06	35.2765	6.999134	6.99937
10	8.87	33.4640	6.999139	6.99937
11	8.70	31.7542	6.999144	6.99937
12	8.53	30.1859	6.999149	6.99937
13	8.38	28.8079	6.999154	6.99937
14	8.23	27.6608	6.999158	6.99937
15	8.08	26.7576	6.999162	6.99937
16	7.94	26.0649	6.999166	6.99937
17	7.80	25.4845	6.999170	6.99937
18	7.67	24.8339	6.999174	6.99937
19	7.54	23.8279	6.999178	6.99937
20	7.42	22.0594	6.999182	6.99937

Table A.25: Container Two - Capillary One @ 51° C, Working Liquid: Octane

Time [Day]	Loc.±0.01 [cm]	Flux $\times 10^{-18}$ $[\frac{molec}{m^2 sec}]$	$P^V_{eq} \pm 10^{-6}$ [KPa]	$P^V_{SRT} \pm 10^{-5}$ [KPa]
0	10.65	95.6466	6.999088	6.99936
1	10.18	81.9114	6.999101	6.99936
2	9.77	70.1310	6.999113	6.99937
3	9.43	60.1557	6.999123	6.99937
4	9.13	51.8354	6.999132	6.99937
5	8.87	45.0202	6.999139	6.99937
6	8.64	39.5603	6.999146	6.99937
7	8.44	35.3057	6.999152	6.99937
8	8.27	32.1064	6.999157	6.99937
9	8.10	29.8125	6.999162	6.99937
10	7.95	28.2742	6.999166	6.99937
11	7.80	27.3414	6.999171	6.99937
12	7.65	26.8643	6.999175	6.99937
13	7.51	26.6930	6.999179	6.99937
14	7.37	26.6774	6.999183	6.99937
15	7.23	26.6678	6.999187	6.99937
16	7.08	26.5140	6.999191	6.99937
17	6.94	26.0663	6.999195	6.99937
18	6.81	25.1747	6.999199	6.99937
19	6.68	23.6893	6.999203	6.99937

Table A.26: Container Two - Capillary Two @ 51° C, Working Liquid: Octane

Time [Day]	Loc.±0.01 [cm]	Flux $\times 10^{-18}$ $[\frac{molec}{m^2 sec}]$	$P_{eq}^{V} \pm 10^{-6}$ [KPa]	$P_{SRT}^{V} \pm 10^{-5}$ [KPa]
0	9.49	48.2673	6.999121	6.99937
1	9.24	45.1897	6.999128	6.99937
2	9.01	42.4289	6.999135	6.99937
3	8.79	39.9606	6.999142	6.99937
4	8.58	37.7606	6.999148	6.99937
5	8.39	35.8048	6.999153	6.99937
6	8.20	34.0687	6.999159	6.99937
7	8.02	32.5282	6.999164	6.99937
8	7.85	31.1591	6.999169	6.99937
9	7.69	29.9370	6.999174	6.99937
10	7.53	28.8378	6.999178	6.99937
11	7.38	27.8372	6.999183	6.99937
12	7.24	26.9110	6.999187	6.99937
13	7.10	26.0348	6.999191	6.99937
14	6.96	25.1846	6.999195	6.99937
15	6.83	24.3359	6.999199	6.99937
16	6.70	23.4647	6.999202	6.99937
17	6.58	22.5466	6.999206	6.99937
18	6.46	21.5573	6.999209	6.99937
19	6.35	20.4727	6.999213	6.99937
20	6.24	19.2685	6.999216	6.99937
21	6.14	17.9205	6.999219	6.99937

Table A.27: Container Two - Capillary Three @ 51° C, Working Liquid: Octane

Time [Day]	Loc.±0.01 [cm]	Flux $\times 10^{-18}$ $[\frac{molec}{m^2 sec}]$	$P_{eq}^{V} \pm 10^{-6}$ [KPa]	$P_{SRT}^{V} \pm 10^{-5}$ [KPa]
0	8.02	33.1994	6.999164	6.99937
1	7.85	30.7141	6.999169	6.99937
2	7.69	28.6225	6.999174	6.99937
3	7.54	26.8884	6.999178	6.99937
4	7.40	25.4752	6.999182	6.99937
5	7.27	24.3466	6.999186	6.99937
6	7.14	23.4660	6.999190	6.99937
7	7.02	22.7972	6.999193	6.99937
8	6.90	22.3036	6.999197	6.99937
9	6.78	21.9489	6.999200	6.99937
10	6.66	21.6965	6.999204	6.99937
11	6.55	21.5102	6.999207	6.99937
12	6.43	21.3534	6.999210	6.99937
13	6.32	21.1897	6.999214	6.99937
14	6.21	20.9827	6.999217	6.99937
15	6.10	20.6961	6.999220	6.99937
16	5.99	20.2932	6.999223	6.99937
17	5.88	19.7378	6.999226	6.99937
18	5.78	18.9934	6.999229	6.99937
19	5.68	18.0235	6.999232	6.99937
20	5.58	16.7918	6.999235	6.99937
21	5.50	15.2619	6.999237	6.99937

Table A.28: Container Two - Capillary Four @ 51° C, Working Liquid: Octane

Time [Day]	Loc.±0.01 [cm]	Flux $\times 10^{-18}$ $[\frac{molec}{m^2 sec}]$	$P^V_{eq} \pm 10^{-6}$ [KPa]	$P^V_{SRT} \pm 10^{-5}$ [KPa]
0	9.26	22.64253	19.249362	19.24993
1	9.18	15.39185	19.249367	19.24993
2	9.12	13.50243	19.249371	19.24993
3	9.06	13.64181	19.249375	19.24993
4	9.00	14.14067	19.249380	19.24993
5	8.94	14.34184	19.249384	19.24993
6	8.88	14.13862	19.249388	19.24993
7	8.82	13.66603	19.249392	19.24993
8	8.76	13.11169	19.249396	19.24993
9	8.70	12.61673	19.249400	19.24993
10	8.65	12.24095	19.249404	19.24993
11	8.60	11.96949	19.249407	19.24993
12	8.55	11.74237	19.249411	19.24993
13	8.49	11.49155	19.249414	19.24993
14	8.45	11.17360	19.249418	19.24993
15	8.40	10.79006	19.249421	19.24993
16	8.35	10.39064	19.249424	19.24993
17	8.31	10.05838	19.249427	19.24993
18	8.26	9.87909	19.249430	19.24993
19	8.22	9.90142	19.249433	19.24993
20	8.18	10.09687	19.249436	19.24993
21	8.13	10.33323	19.249439	19.24993
22	8.09	10.37802	19.249442	19.24993
23	8.05	9.95237	19.249445	19.24993
24	8.00	8.85917	19.249448	19.24993

Table A.29: Container One - Capillary One @ 51° C, Working Liquid: Methylcyclohexane

Time [Day]	Loc.±0.01 [cm]	Flux $\times 10^{-18}$ $[\frac{molec}{m^2 sec}]$	$P^V_{eq} \pm 10^{-6}$ [KPa]	$P^V_{SRT} \pm 10^{-5}$ [KPa]
0	7.50	14.87741	19.249483	19.24993
1	7.45	8.37340	19.249486	19.24993
2	7.42	7.15525	19.249488	19.24993
3	7.39	7.78969	19.249490	19.24993
4	7.35	8.61614	19.249493	19.24993
5	7.31	9.03291	19.249495	19.24993
6	7.28	8.99639	19.249498	19.24993
7	7.24	8.69092	19.249501	19.24993
8	7.20	8.33141	19.249503	19.24993
9	7.16	8.06474	19.249506	19.24993
10	7.13	7.94052	19.249508	19.24993
11	7.10	7.92569	19.249510	19.24993
12	7.06	7.94170	19.249513	19.24993
13	7.03	7.90749	19.249515	19.24993
14	6.99	7.77524	19.249518	19.24993
15	6.96	7.55053	19.249520	19.24993
16	6.93	7.29235	19.249522	19.24993
17	6.90	7.09294	19.249524	19.24993
18	6.87	7.04142	19.249526	19.24993
19	6.84	7.17949	19.249528	19.24993
20	6.80	7.46161	19.249531	19.24993
21	6.77	7.73646	19.249533	19.24993
22	6.74	7.77029	19.249535	19.24993
23	6.70	7.33753	19.249537	19.24993
24	6.67	6.40775	19.249539	19.24993

Table A.30: Container One - Capillary Two @ 51° C, Working Liquid: Methylcyclohexane

Time [Day]	Loc.±0.01 [cm]	Flux $\times 10^{-18}$ $[\frac{molec}{m^2 sec}]$	$P_{eq}^{V} \pm 10^{-6}$ [KPa]	$P_{SRT}^{V} \pm 10^{-5}$ [KPa]
0	6.01	10.15777	19.249585	19.24993
1	5.98	4.83847	19.249587	19.24993
2	5.96	3.85986	19.249588	19.24993
3	5.94	4.47986	19.249590	19.24993
4	5.92	5.31950	19.249591	19.24993
5	5.90	5.83569	19.249593	19.24993
6	5.87	5.94560	19.249595	19.24993
7	5.85	5.77346	19.249596	19.24993
8	5.82	5.49352	19.249598	19.24993
9	5.80	5.24560	19.249600	19.24993
10	5.78	5.10258	19.249601	19.24993
11	5.76	5.07204	19.249603	19.24993
12	5.73	5.11705	19.249604	19.24993
13	5.71	5.18406	19.249606	19.24993
14	5.69	5.22847	19.249607	19.24993
15	5.67	5.23160	19.249609	19.24993
16	5.64	5.20540	19.249610	19.24993
17	5.62	5.18407	19.249612	19.24993
18	5.60	5.20492	19.249613	19.24993
19	5.58	5.28311	19.249615	19.24993
20	5.55	5.38832	19.249617	19.24993
21	5.53	5.43384	19.249618	19.24993
22	5.51	5.29159	19.249620	19.24993
23	5.48	4.84939	19.249621	19.24993
24	5.46	4.12968	19.249623	19.24993

Table A.31: Container One - Capillary Three @ 51° C, Working Liquid: Methylcyclohexane

Time [Day]	Loc.±0.01 [cm]	Flux $\times 10^{-18}$ $[\frac{molec}{m^2 sec}]$	$P_{eq}^{V} \pm 10^{-6}$ [KPa]	$P_{SRT}^{V} \pm 10^{-5}$ [KPa]
0	4.51	6.26962	19.249688	19.249934
1	4.50	2.09760	19.249689	19.249934
2	4.49	1.50523	19.249690	19.249934
3	4.48	2.17571	19.249690	19.249934
4	4.47	2.97934	19.249691	19.249934
5	4.46	3.48229	19.249692	19.249934
6	4.44	3.61851	19.249693	19.249934
7	4.43	3.48416	19.249694	19.249934
8	4.41	3.21994	19.249695	19.249934
9	4.40	2.95216	19.249696	19.249934
10	4.38	2.76934	19.249697	19.249934
11	4.37	2.71671	19.249698	19.249934
12	4.36	2.79693	19.249699	19.249934
13	4.35	2.97070	19.249699	19.249934
14	4.34	3.15717	19.249700	19.249934
15	4.32	3.23927	19.249701	19.249934
16	4.31	3.08537	19.249702	19.249934
17	4.30	2.60374	19.249703	19.249934
18	4.29	1.85283	19.249704	19.249934

Table A.32: Container One - Capillary Four @ 51° C, Working Liquid: Methylcyclohexane

Time [Day]	Loc.±0.01 [cm]	Flux $\times 10^{-18}$ $[\frac{molec}{m^2 sec}]$	$P_{eq}^{V} \pm 10^{-6}$ [KPa]	$P_{SRT}^{V} \pm 10^{-5}$ [KPa]
0	10.48	29.0613	19.2492741	19.249934
1	10.37	22.9764	19.2492819	19.249934
2	10.28	19.5104	19.2492882	19.249934
3	10.20	17.7187	19.2492938	19.249934
4	10.12	16.9188	19.2492990	19.249934
5	10.05	16.6338	19.2493041	19.249934
6	9.97	16.5469	19.2493091	19.249934
7	9.90	16.4634	19.2493141	19.249934
8	9.83	16.2801	19.2493190	19.249934
9	9.76	15.9606	19.2493239	19.249934
10	9.69	15.5137	19.2493286	19.249934
11	9.62	14.9773	19.2493332	19.249934
12	9.56	14.4033	19.2493377	19.249934
13	9.50	13.8458	19.2493419	19.249934
14	9.44	13.3517	19.2493461	19.249935
15	9.38	12.9526	19.2493500	19.249935
16	9.32	12.6601	19.2493539	19.249935
17	9.27	12.4630	19.2493577	19.249935
18	9.21	12.3291	19.2493614	19.249935
19	9.16	12.2105	19.2493651	19.249935
20	9.11	12.0554	19.2493688	19.249935
21	9.05	11.8261	19.2493724	19.249935
22	9.00	11.5263	19.2493759	19.249935
23	8.95	11.2385	19.2493794	19.249935
24	8.90	11.1735	19.2493827	19.249935
25	8.85	11.7356	19.2493862	19.249935

Table A.33: Container Two - Capillary One @ 51° C, Working Liquid: Methylcyclohexane

Time [Day]	Loc.±0.01 [cm]	Flux $\times 10^{-18}$ $[\frac{molec}{m^2 sec}]$	$P_{eq}^{V} \pm 10^{-6}$ [KPa]	$P_{SRT}^{V} \pm 10^{-5}$ [KPa]
0	8.61	16.9818	19.2494028	19.249934
1	8.55	13.8220	19.2494074	19.249934
2	8.49	11.9172	19.2494112	19.249935
3	8.44	10.9435	19.2494147	19.249935
4	8.39	10.5956	19.2494179	19.249935
5	8.35	10.6093	19.2494211	19.249935
6	8.30	10.7744	19.2494243	19.249935
7	8.25	10.9401	19.2494276	19.249935
8	8.20	11.0139	19.2494309	19.249935
9	8.16	10.9552	19.2494342	19.249935
10	8.11	10.7657	19.2494375	19.249935
11	8.06	10.4777	19.2494407	19.249935
12	8.02	10.1408	19.2494438	19.249935
13	7.97	9.8093	19.2494469	19.249935
14	7.93	9.5308	19.2494498	19.249935
15	7.89	9.3367	19.2494526	19.249935
16	7.85	9.2362	19.2494554	19.249935
17	7.81	9.2137	19.2494582	19.249935
18	7.77	9.2320	19.2494610	19.249935
19	7.73	9.2401	19.2494638	19.249935
20	7.69	9.1869	19.2494666	19.249935
21	7.64	9.0426	19.2494693	19.249935
22	7.61	8.8259	19.2494720	19.249935
23	7.57	8.6395	19.2494747	19.249935
24	7.53	8.7128	19.2494773	19.249935
25	7.49	9.4528	19.2494800	19.249935

Table A.34: Container Two - Capillary Two @ 51° C, Working Liquid: Methylcyclohexane

Time [Day]	Loc.±0.01 [cm]	Flux $\times 10^{-18}$ $[\frac{molec}{m^2 sec}]$	$P_{eq}^{V} \pm 10^{-6}$ [KPa]	$P_{SRT}^{V} \pm 10^{-5}$ [KPa]
0	6.88	9.0479	19.2495222	19.249935
1	6.84	8.5995	19.2495248	19.249935
2	6.80	7.9328	19.2495273	19.249935
3	6.77	7.3779	19.2495296	19.249935
4	6.74	7.0614	19.2495318	19.249935
5	6.71	6.9836	19.2495339	19.249935
6	6.67	7.0771	19.2495360	19.249935
7	6.64	7.2498	19.2495382	19.249935
8	6.61	7.4150	19.2495404	19.249935
9	6.58	7.5087	19.2495427	19.249935
10	6.55	7.4983	19.2495449	19.249935
11	6.51	7.3828	19.2495472	19.249935
12	6.48	7.1882	19.2495494	19.249935
13	6.45	6.9575	19.2495515	19.249935
14	6.42	6.7403	19.2495536	19.249935
15	6.39	6.5804	19.2495556	19.249935
16	6.36	6.5054	19.2495576	19.249935
17	6.33	6.5192	19.2495595	19.249935
18	6.30	6.5985	19.2495615	19.249935
19	6.27	6.6957	19.2495635	19.249935
20	6.25	6.7489	19.2495656	19.249935
21	6.22	6.7011	19.2495676	19.249935
22	6.19	6.5292	19.2495696	19.249935
23	6.16	6.2849	19.2495715	19.249935
24	6.13	6.1482	19.2495734	19.249935
25	6.10	6.4952	19.2495753	19.249935

Table A.35: Container Two - Capillary Three @ 51° C, Working Liquid: Methylcyclohexane

Time [Day]	Loc.±0.01 [cm]	Flux $\times 10^{-18}$ $[\frac{molec}{m^2 sec}]$	$P_{eq}^{V} \pm 10^{-6}$ [KPa]	$P_{SRT}^{V} \pm 10^{-5}$ [KPa]
0	5.02	12.6600	19.2496501	19.249935
1	4.97	8.1903	19.2496532	19.249935
2	4.94	5.7387	19.2496552	19.249935
3	4.92	4.5948	19.2496568	19.249935
4	4.90	4.2383	19.2496581	19.249935
5	4.88	4.2998	19.2496594	19.249935
6	4.86	4.5287	19.2496607	19.249935
7	4.84	4.7668	19.2496621	19.249935
8	4.82	4.9275	19.2496636	19.249935
9	4.80	4.9771	19.2496651	19.249935
10	4.78	4.9201	19.2496666	19.249935
11	4.76	4.7854	19.2496680	19.249935
12	4.73	4.6148	19.2496695	19.249935
13	4.71	4.4528	19.2496708	19.249935
14	4.70	4.3374	19.2496722	19.249935
15	4.68	4.2930	19.2496735	19.249935
16	4.66	4.3253	19.2496748	19.249935
17	4.64	4.4190	19.2496761	19.249935
18	4.62	4.5393	19.2496774	19.249935
19	4.60	4.6385	19.2496788	19.249935
20	4.58	4.6683	19.2496802	19.249935
21	4.56	4.6004	19.2496816	19.249935
22	4.54	4.4569	19.2496830	19.249935
23	4.52	4.3516	19.2496843	19.249935
24	4.50	4.5463	19.2496857	19.249935
25	4.48	5.5227	19.2496871	19.249935

Table A.36: Container Two - Capillary Four @ 51° C, Working Liquid: Methylcyclohexane

Time [Day]	Loc.±0.01 [cm]	Flux $\times 10^{-20}$ $[\frac{molec}{m^2 sec}]$	$P_{eq}^{V} \pm 10^{-6}$ [KPa]	$P_{SRT}^{V} \pm 10^{-5}$ [KPa]
0	9.28	9.6960	21.176473	21.17655
2	8.28	8.2700	21.176486	21.17656
4	7.43	7.0668	21.176498	21.17656
6	6.70	6.0629	21.176508	21.17656
8	6.07	5.2349	21.176516	21.17656
10	5.52	4.5597	21.176523	21.17656
12	5.04	4.0150	21.176530	21.17656
14	4.62	3.5790	21.176536	21.17656
16	4.24	3.2316	21.176541	21.17656
18	3.90	2.9540	21.176545	21.17656
20	3.58	2.7293	21.176550	21.17656
22	3.29	2.5428	21.176553	21.17656
24	3.01	2.3824	21.176557	21.17656
26	2.75	2.2387	21.176561	21.17656
28	2.51	2.1055	21.176564	21.17656
30	2.28	1.9801	21.176567	21.17656
32	2.07	1.8635	21.176570	21.17656
34	1.87	1.7608	21.176573	21.17657
36	1.67	1.6817	21.176575	21.17657
38	1.49	1.6403	21.176578	21.17657

Table A.37: Container Two - Capillary One @ 62° C

Time [Day]	Loc.±0.01 [cm]	Flux $\times 10^{-20}$ $[\frac{molec}{m^2 sec}]$	$P_{eq}^{V} \pm 10^{-6}$ [KPa]	$P_{SRT}^{V} \pm 10^{-5}$ [KPa]
0	6.42	6.4176	21.176511	21.17656
2	5.76	5.4329	21.176520	21.17656
4	5.20	4.6419	21.176528	21.17656
6	4.72	4.0087	21.176534	21.17656
8	4.30	3.5027	21.176540	21.17656
10	3.93	3.0984	21.176545	21.17656
12	3.60	2.7750	21.176549	21.17656
14	3.31	2.5154	21.176553	21.17656
16	3.04	2.3060	21.176557	21.17656
18	2.79	2.1363	21.176560	21.17656
20	2.56	1.9978	21.176563	21.17656
22	2.34	1.8840	21.176566	21.17656
24	2.14	1.7896	21.176569	21.17656
26	1.94	1.7100	21.176571	21.17657
28	1.76	1.6407	21.176574	21.17657
30	1.58	1.5770	21.176576	21.17657
32	1.40	1.5130	21.176579	21.17657
34	1.24	1.4415	21.176581	21.17657
36	1.08	1.3534	21.176583	21.17657

Table A.38: Container Two - Capillary Two @ 62° C

Time [Day]	Loc.±0.01 [cm]	Flux $\times 10^{-20}$ $[\frac{molec}{m^2 sec}]$	$P_{eq}^{V} \pm 10^{-6}$ [KPa]	$P_{SRT}^{V} \pm 10^{-5}$ [KPa]
0	4.67	5.3427	21.176535	21.17656
2	4.12	4.5183	21.176542	21.17656
4	3.65	3.8968	21.176549	21.17656
6	3.25	3.4246	21.176554	21.17656
8	2.89	3.0592	21.176559	21.17656
10	2.56	2.7679	21.176563	21.17656
12	2.27	2.5265	21.176567	21.17656
14	2.00	2.3182	21.176571	21.17656
16	1.75	2.1325	21.176574	21.17656
18	1.52	1.9640	21.176577	21.17656
20	1.31	1.8112	21.176580	21.17656
22	1.11	1.6751	21.176583	21.17657
25	0.85	1.5081	21.176586	21.17657
27	0.68	1.4257	21.176588	21.17657
29	0.53	1.3681	21.176591	21.17657
31	0.38	1.3339	21.176593	21.17657
37	-0.06	1.2935	21.176598	21.17657

Table A.39: Container Two - Capillary Three @ 62° C

Time [Day]	Loc.±0.01 [cm]	Flux $\times 10^{-20}$ $[\frac{molec}{m^2 sec}]$	$P_{eq}^{V} \pm 10^{-6}$ [KPa]	$P_{SRT}^{V} \pm 10^{-4}$ [KPa]
0	2.76	4.8758	21.176561	21.1766
2	2.24	4.4427	21.176568	21.1766
4	1.76	4.0510	21.176574	21.1766
6	1.33	3.6979	21.176580	21.1766
8	0.94	3.3807	21.176585	21.1766
10	0.57	3.0969	21.176590	21.1766
12	0.24	2.8436	21.176594	21.1766
15	-0.21	2.5153	21.176600	21.1766
18	-0.60	2.2409	21.176606	21.1766
20	-0.84	2.0834	21.176609	21.1766
22	-1.07	1.9432	21.176612	21.1766
24	-1.28	1.8176	21.176615	21.1766
26	-1.48	1.7039	21.176617	21.1766
28	-1.66	1.5995	21.176620	21.1766
30	-1.83	1.5017	21.176622	21.1766
32	-2.00	1.4077	21.176624	21.1766
34	-2.15	1.3150	21.176626	21.1766

Table A.40: Container Two - Capillary Four @ 62° C

Bibliography

[1] V. K. Badam, V. Kumar, F. Durst, and K. Danov. Experimental and theoretical investigations on interfacial temperature jumps during evaporation. *Experimental thermal and fluid science*, 32:276–292, 2007.

[2] Ward C.A. and Sasges M. R. Effect of gravity on contact angle: A theoretical investigation. *Journal of chemical physics*, 109:3651, 1998.

[3] P. Rahimi. *Effect of Pressure on the rate of evaporation.* PhD thesis, University of Toronto, 2003.

[4] P. Rahimi and C. A. Ward. Effect of pressure on the rate of evaporation from capillaries: statistical rate theory approach. *International Journal of Heat and Mass Transfer*, 47:877–886, 2004.

[5] D. Bedeaux and S. Kjelstrup. Trasnfer coefficients for evaporation. *Physica A*, 270:413–426, 1999.

[6] Hertz H. On the evaporation of liquids, especially mercury, in vaccum. *Annals of Physics*, 17:177, 1882.

[7] T. A. Delchar. *Vacuum Physics and Techniques.* Chapman & Hall, 1993. chaper 1 and 4.

[8] I. W. Eames, N. J. Marr, and H. Sabir. The evaporation coefficient of water: a review. *International Journal of Heat and Mass Transfer*, 40:2963–2973, 1997.

[9] Knudsen Martin. *The kinetic Theory of Gases.* Methuens Monographs on Physical Subjects, 1950.

[10] J. Barrett and C. Clement. Kinetic evaporation and condensation rates and their coefficinets. *Journal of Colloid and Interface Science*, 150:352–364, 1991.

[11] R. Marek and J. Straub. Analysis of the evaporation coefficient and the condensation coefficient of water. *Int. Journal of heat and mass transfer*, 44:39–53, 2001.

[12] Robert W. Schrage. *A theroretical Study Of Interphase Mass Transfer*. Columbia Univ. Press, New York, 1953.

[13] M. Bond and H. Struchtrup. Mean evaporation and condensation coefficients based on energy dependent condensation probability. *Physical Review E*, 70, 2004.

[14] Simon JM, Kjelstrup S., Bedeaux D., and Hafskjold B. Thermal f;ux through a surface of n-octane. a non-equilibrium molecular dynamics study. *Journal of physical Chemistry*, 108:7186–7195, 2004.

[15] Young-Ping Pao. Application of kinetic theory to problem of evaporation and condensation. *The physics of Fluids*, 14:306, 1971.

[16] Young-Ping Pao. Errat: Temperature and density jumps in kinetic theory of gases and vapors. *The Physics of Fluids*, 16:1560, 1971.

[17] Young-Ping Pao. Temperature and density jumps in the kinetic theory of gases and vapors. *The physics of Fluids*, 14:1340, 1971.

[18] Bedeaux D., Hermans L. J. F, and Ytrehus T. Slow evaporation and condensation. *Physica A*, 169:263–280, 1990.

[19] T. Ytrehus. Molecular flow effects in evaporation and condensation at interfaces. *Multiphase Sci. Technology*, 9:205, 1997.

[20] Koffman L. D., Plesset M. S., and Lees L. Theory of evaporation and condensation. *Physics of Fluids*, 27:876, 1984.

[21] Aoki K. and Masukawa N. Gas flows caused by evaporation and condensation on two parallel condensed phases and negative temperature gradient: Numerical analysis by using nonlinear kinetic equation. *Physics of Fluids*, 6:1379, 1994.

[22] L. J. F Hermans and L. J. F Beenakker. The temperature paradox in the kinetic theory of evaporation. *Physics of Fluids*, 29:4231–4232, 1986.

[23] R. Meland. Molecular dynamics simulation of the inverted temperature gradient phenomenon. *Physics of Fluids*, 15:3244, 2003.

[24] A. Frezzotti, P. Grosfils, and S. Toxvaerd. Evidence of an temperature gradient during evaporation/condensation of a lennard-jones fluid. *Physics of Fluids*, 15:2837, 2003.

[25] J. J. Wlwklinski. Verification of the inverted temperature gradient condition via molecualr dynamics simulation. *Physica A*, 360:151–158, 2006.

[26] E. Johannessen and D. Bedeaux. Integral relations for the interfacial heat and mass transfer resistivities and inverted temperature gradient. *Physics of Fluids*, 19, 2007.

[27] G. Fang and C.A. Ward. Temperature measured close to the interface of an evaporating liquid. *Physical Review E*, 59:417–428, 1999.

[28] G. Fang and C. A. Ward. Examination of the statistical rate theory expression for liquid evaporation rates. *Physica review E*, 59:441–453, 1999.

[29] Fei Duan, V. K. Badam, F. Durst, and C. A. Ward. Thermocapillary transport of energy during water evaporation. *Physical Review E*, 72, 2005.

[30] C. A. Ward and F. Duan. Turbulent transition of thermocapillary flow induced by water evaporation. *Physical Review E*, 69, 2004.

[31] Fei Duan and C. A. Ward. Surface excess properties from energy transport measurments during water evaporation. *Physical Review*, 72, 2005.

[32] F. Duan and C. A. Ward. Surface-thermal capacity of d_2o from measurments made during steady-state evaporation. *Physical Review E*, 72, 2005.

[33] K. Sefiane and C. A. Ward. Recent advances on thermocapillary flows and interfacial conditions during evaporation of liquids. *Advances in Colloid and Interface Science*, 134-135:201–223, 2007.

[34] K. Sefiane. Gravitational effects on evaporative convection at microscale. *Microgravity Science and Tech.*, 18:25–28, 2006.

[35] H. K. Dhavaleswarapu, P. Chamarthy, S. V. Garimella, and J. Y. Murthy. Experimental investigation of steady buoyant-thermocapillary convection near an evaporating meniscus. *Physics of fluids*, 19, 2007.

[36] A. Steinchen and K. Sefiane. Self-organised Marangoni motion at evaporating drops or in capillary menisci-thermohydrodynamical model. *Journal of nonequilibrium thermodynamics*, 30:39–51, 2005.

[37] R. J. Hunter. *Foundations of colloid science*. Oxford Univ. Press, 2001.

[38] S. Popov, A. Melling, F. Durst, and C. A. Ward. Apparatus for investigation of evaporation at free liquid-vapor interfaces. *International Journal of Heat and Mass Transfer*, 48:2299–2309, 2005.

[39] S. Dasgupta, I. Y. Kim, and Jr. P. C. Wayner. Use of the kelvin-clapeyron equation to model an evaporating curved microfilm. *Journal of heat transfer*, 116:1007–1014, 1994.

[40] L. W. Swanson and G. C. Herdt. Model of the evaporating meniscus in capillary tube. *Journal of heat transfer-transactions of the ASME*, 114:434–441, 1992.

[41] K. Park, K. J. Noh, and K. S. Lee. Transport phenomena in the thin film region of a micro-channel. *International Journal of Heat and Mass Transfer*, 46:2381–2388, 2003.

[42] V. Sartre, M. C. Zaghdoudi, and M. Lallemand. Effect of interfacial phenomena on evaporative heat trnasfer in micro heat pipes. *Int. J. Therm. Sci.*, 39:498–504, 2000.

[43] K. Sefiane, M. Snodgrass, and A. Stienchen. Evaporation self-induced Marangoni motion fed capillaries for volatile liquids in open air. *Journal of non equilibrium thermodynamics*, 29:177–198, 2004.

[44] J. J. Yoo. Recent studies on fluid flow and heat transfer in thermal microdevices. *Nanoscale and Microscale Thermophysical Engineering*, 10:67–81, 2006.

[45] J. Rice and A. Faghri. Analysis of the marangoni effect in volatile liquids evaporating from capillary tubes using a new interface tracking method. *Numerical heat transfer, Part A*, 51:445–468, 2007.

[46] C. Buffone and K. Sefiane. Temperature measurment near the triple line during phase change using thermochromic liquid crystal thermography. *Experiments in Fluids*, 39:99–110, 2005.

[47] C. Buffone and K. Sefiane. Ir measurments of interfacial temperature during phase change in confined enviroment. *Experimental thermal and fluid science*, 29:65–74, 2004.

[48] C. Höhmann and P. Stephan. Microscale temperature measurment at an evaporation liquid meniscus. *Experimental thermal and fluid science*, 26:157–162, 2002.

[49] C. Buffone, K. Sefiane, and W. Easson. Marangoni driven instabilities of an evaporating liquid-vapor interface. *Physical Review E*, 71:056302, 2005.

[50] H. Wang, S. V. Garimella, and J. Y. Murthy. Chractristics of an evaporating thin film in a microchannel. *International Journal of Heat and Mass Transfer*, 50:3933–3942, 2007.

[51] H. Wang, J. Y. Murthy, and S. V. Garimella. Transport form a volatile meniscus insde and open microtube. *International Journal of Heat and Mass Transfer*, 51:3007–3017, 2008.

[52] C. Buffone and K. Sefiane. Marangoni convection in capillary tubes filled with volatile liquids. In *First international conference on Microchannels and Minichannels*, April 24-25, 2003, Rochester, New York, USA.

[53] C. Buffone and K. Sefiane. Controlling evaporative thermocapillary convection using external heating: An experimental investigation. *Experimental thermal and fluid science*, 32:1287–1300, 2008.

[54] C. Buffone, K. Sefiane, and J. R. E. Christy. Experimental investigation of the hydrodynamics and stability of an evaporating wetting film placed in a temperature gradient. *Applied thermal engineering*, 24:1157–1170, 2004.

[55] P. Chamarthy, H. K. Dhavaleswarapu, S. V. Garimella, J. Y. Murthy, and S. T. Wereley. Visualization of concentration patterns near an evaporating meniscus using μPIV. *Experimental fluids*, 44:431–438, 2008.

[56] P. Colinet, L. Joannes, C.S. Iorio, B. Hat, M. Bestehorn, G. Lebon, and J.C. Legros. Interfacial turbulence in evaporating liquids : Theory and preliminary results of the itel-master 9 sounding rocket experiment. *Adv. Spc. Res.*, 32:119–127, 2003.

[57] C. Buffone, K. Sefiane, and J. R. E. Christy. Experimental investigation of self-induced thermocapillary convection for an evaporating meniscus in capillary tubes using micro-particle image velocimetry. *Physics of Fluids*, 17, 2005.

[58] C. Buffone and K. Sefiane. Investigation of thermocapillary convective patterns and their role in the enhancement of evaporation form pores. *Int. Journal of Multiphase Flow*, 30:1071–1091, 2004.

[59] J. M. Potash and J. P. Wayner. Evaporation form a two-dimensional extended meniscus. *Int. J. Heat and mass transfer*, 15:1851, 1972.

[60] S. Jin, C. Choi, K. S. Breuer, and J. Y. Yoo. Effects of cross-section geometry of capillary on the evaporation from the meniscus. In *Third international conference on Microchannels and Minichannels*, June 13-15, 2005, Toronto, Ontario, Canada.

[61] M. R. Sasges. *The effect of gravity on fluid configuration and contact angle hysteresis*. PhD thesis, University of Toronto, 1997.

[62] H. B. Callen. *Thermodynamics and an introduction to thermostatistics*. John Wiley and Sons, 1985.

[63] J. Willard Gibbs. *The Scientific Papers of J. Willard Gibbs*, volume I. Dover, New York, 1961.

[64] Munster A. *Classical Thermodynamics*. John Wiley and Sons, 1970.

[65] J. A. W Elliott, C. A. Ward, and D. Yee. Bubble shapes in rotating two-phase fluid systems: a thermodynamic approach. *Fluid Mech*, 319:1–23, 1996.

[66] J. J. Tuma and R. A. Walsh. *Engineering Mathematics Handbook*. McGraw Hill, second edition, 1997.

[67] F. Bashforth and J. C. Adams. *An attempt to test the theories of capillary rise action.* Cambridge Univ. Press and Deighton Bell & Co. Cambridge, 1983.

[68] P. Contreras and M. Olteanu. Interfacial tension measurement by the. rotating meniscus. *Colloids and Surfaces A*, 170:45–50, 2000.

[69] M. R. Sasges and C. A. Ward. Equilibrium fluid configurations in low gravity. *Journal of Applied Physics*, 79:8870–8778, 1996.

[70] Ward C.A. and Sasges M. R. Effect of gravity on contact angle: An experimental investigation. *Journal of chemical physics*, 109:3661, 1998.

[71] C. A. Ward, W. R. Johnson, R.D. Venter, T.W. Ho, S. Forest, and Fraser W.D. Heteregeneous bubble nucleation and conditions for growth in a liquid-gas system of constant mass and volume. *Journal of applied physics.*, 54:1833–1844, 1983.

[72] P. Rahimi and C. A. Ward. Kinetics of evaporation: Statistical rate theory approach. *Int. Journal of Applied Thermodynamics*, 8:1–12, 2005.

[73] A. W. Neumann and J. K. Spelt. *Applied Surface Thermodynamics*, chapter 10, pages 442–480. CRC press, 1996.

[74] M. Hoorfar and A.W. Neumann. Recent progress in axisymmetric drop shape analysis (adsa). *Advances in Colloid and Interface Science*, 121:25–49, 2006.

[75] S. O. Asekomhe and J. A. W. Elliott. The effect of interface deformation due to gravity on line tension measurment by capillary rise in a conical tube. *Colloids and Surfaces A*, 220:271–278, 2003.

[76] A. Bateni, A. Abdaneh, J. A. W. Elliott, A. W. Neumann, and A. Amirfazli. Effect of gravity and electric field on shape and surface tension of drops. *Advanced in space research*, 36:64–69, 2005.

[77] Nakamura S. *Numerical Analysis and Graphic Visualization with Matlab.* Prentice Hall, second edition, 2002.

[78] Ward C. A., R. D. Findlay, and M. Rizk. Statistical rate theory of interfacial trnasport. i. theoretical development. *Journal of Chemical Physics*, 76:5599–5605, 1982.

[79] C. A Ward. Liquid-vapour phase change rates and interfacial entropy production. *Journal of Non-Equilibrium Thermodynamics*, 27:289–303, 2002.

[80] A. J. H. McGaughey and C. A. Ward. Temperature discontiniuity at the surface of an evaporating droplet. *Journal of applied physics*, 91:6406–6415, 2002.

[81] C. A. Ward and G. Fang. Expression for predicting liquid flux: Statistical rate theory approach. *Physical Review E*, 59:429–440, 1999.

[82] C. A. Ward. Effect of concentration on the rate of chemical reactions. *Journal of Chemical Physics*, 79, 1983.

[83] Terrell L. Hill. *An introduction to statistical thermodynamics*. Dover Publications, Inc., 1986.

[84] G. Fang. *Rate of liquid evaporation: Statistical rate theory approach*. PhD thesis, University of Toronto, 1998.

[85] J. A. W. Elliott. *Advancements in the statistical rate theory treatment of adsorption*. PhD thesis, University of Toronto, 1997.

[86] J. A. W Elliott and C. A. Ward. Statistical rate theory and the material properties controlling adsorption kinetics on well defined surfaces. *Applied Surface Science*, 104, 1997.

[87] C. A. Ward. The rate of gas adsorption at a liquid interface. *Journal of Chemical Physics*, 67:229–235, 1977.

[88] C. A Ward and D. Stagna. Intefacial conditions during evaporation or condensation of water. *Physical Review E*, 64, 2001.

[89] B.J. McClelland. *Statistical Thermodynamics*. Chapman and Hall, 1973.

[90] Normand M. Laurendeau. *Statistical thermodynamics : fundamentals and applications*. Cambridge University Press, 2005.

[91] Gerhard Herzberg. *Molecular Spectra and Molecular Structure*, volume II. Krieger Publishing Company, 1991.

[92] R. H. Folwer and E. A. Guggenheim. *Statistical Thermodynamics*. Cambridge Univ. Press, 1939.

[93] G. B. Jackson. *Applied Water and Spentwater Chemistry: A Laboratory Manual*. Springer, 1993.

[94] Gonzalez and Woods. *Digital Image Processing*. Prentice Hall, 3rd edition, 2008.

[95] Woods Gonzalez and Eddins. *Digital Image Processing Using Matlab*. Prentice Hall, 2004.

[96] John C. Russ. *The Image Processing Handbook*. CRC Press, fifth edition, 2007.